Numerical Modelling of Ti6Al4V Machining: A Combined FEA and Unified Mechanics of Cutting Approach

by
David Christian Bowes

Thesis presented in fulfilment of the requirements for the degree of Master of Science in Engineering (Mechanical) in the Faculty of Engineering at Stellenbosch University

Supervisors:
Mr Nico Treurnicht
Mr Kobus van der Westhuizen

March 2013

Declaration

By submitting this thesis electronically, I declare that the entirety of the work contained therein is my own, original work, that I am the sole author thereof (save to the extent explicitly otherwise stated), that reproduction and publication thereof by Stellenbosch University will not infringe any third party rights and that I have not previously in its entirety or in part submitted it for obtaining any qualification.

Signature: .....

D.C Bowes

Abstract

Numerical Modelling of Ti6Al4V machining:
A Combined FEA and Unified Mechanics Approach

D.C Bowes

Department of Mechanical Engineering
University of Stellenbosch
Private Bag X1, 7602 Matieland, South Africa

Thesis: MSc.Eng (Mech)

March 2013

In this study, Ti6Al4V machining is modelled using finite element analysis of orthogonal machining. Orthogonal turning tests are conducted for the verification of FE models in terms of machining forces, temperatures, and chip geometry. Milling force predictions are made using the "unified" mechanics of cutting model which is applied to ball nose milling for this study. The model makes use of orthogonal cutting data, collected from the turning tests, to model milling forces. Model predictions are compared with test data from slot milling tests for verification. Finally a hybrid form of the "'unified"' model is presented in which orthogonal data, obtained from the FE simulations, is used to model ball nose milling operations.

Uittreksel

Modellering van titaanmasjinering

("Numerical Modelling of Ti6Al4V machining:
A Combined FEA and Unified Mechanics Approach")

D.C Bowes

Departement Meganiese Ingenieurswese
Universiteit van Stellenbosch
Privaatsak X1, 7602 Matieland, Suid Afrika

Tesis: MSc.Ing (Meg)

Maart 2013

In hierdie studie word titaanmasjinering (Ti6Al4V) gemodelleer deur gebruik te maak van eindige element analise van ortogonale masjinering. Ortogonale draai toetse word uitgevoer om eindige element (FE) modelle te verifieer in terme van masjineringskragte, temperatuur en spaandergeometrie. Freeskragte word voorspel deur gebruik te maak van die "Unified Mechanics of Cutting"model wat toegepas word op 'n balneusfrees operasie in hierdie studie. Die model maak gebruik van ortogonale snydata, versamel gedurende snytoetse, om die freeskragte te modelleer. Die model word vervolgens vergelyk met die toetsdata afkomstig van die freestoetse vir verifikasie. Ten slotte word 'n hibriede weergawe van die model aangebied waarin ortogonale data verkry word van die FE simulasie om balneus freesoperasies te simuleer.

Acknowledgements

Acknowledgement must be made of the following individuals and organisations:

- Mr N Treurnicht and Mr K van der Westhuizen for supervising the study.
- AMTS (Advanced Manufacturing Technology Stategy) for support and funding through their flagship light metals programme, for which this project was commissioned.
- Element Six, world leading manufacturer of industrial diamonds and superhard materials, for technical support, the use of test facilities and financial support. In particular, I would like to thank Serdar Osbayraktar (General Manager of the Diamond Research Lab), Johnny Lai-Sang and Habib Saridikmen for their input and support in various aspects of this project.

Contents

List of Figures

List of Tables

Chapter 1

Introduction

Titanium, is an important material in several industries due to its favourable mechanical and chemical properties. A combination of good strength to weight ratio, high hot hardness, corrosion resistance and good fatigue properties lends itself well to these challenging environments. Its most important application is in the aerospace, biomedical and automotive industries.

Titanium is known as a material which is difficult to machine for a variety of reasons. The main consequence of its poor machinability is that practical cutting speeds must be kept low (approxof 60 m/min), to achieve reasonable tool life. This is in contrast to materials such as aluminium alloys, which are routinely machined at speeds in the order of 1000 m/min in high speed machining applications.

Its poor machinability can be attributed to a variety of factors, the first being its low thermal conductivity. This results in a concentrated build up of heat at the cutting edge with high temperatures ($750°C$ at 300 m/min under dry cutting conditions was measured in this study). The low heat dissipation by chips and workpiece, due to low conductivity coupled with high heat capacity, sets up high temperature gradients in the tool, resulting in high thermal stresses of the cutting edge. The high temperatures associated with titanium machining is also strongly related to the chip formation mode seen in titanium where segemented chips are formed. High temperatures also lead to increased chemical reactivity, resulting in diffusion wear. Adhesion between the material and tool is also elevated with increasing temperature, resulting in tool failure. Another consideration is the hazard of exoergic reaction of chips in atmospheric air, which causes them to combust energetically and has been the cause of numerous industrial incidents.

Furthermore, high pressure loads are encountered at the cutting edge as result of the small contact surface area, due to short contact length. This exacerbated by the pulsatory nature of the cutting forces due to segmental chip formation. Tool failure may also occur through chipping due to high cutting forces and self induced chatter. In titanium machining, there is a strong tendency to vibration as a result of titanium's high strength coupled with low Young's modulus, which may cause large workpiece deflections inducing chatter and geometrical inaccuracies.

In aerospace, titanium is commonly used in critical structural components and also has application in turbine components such as turbine blades and jet nozzles [1]. In recent years there has been a shift from the widespread use of aluminium alloys alone to the use of titanium alloys and composite materials. With a strong growth of civil air

traffic predicted and an increase in titanium content in aircraft there is a strong drive to develop titanium machining competence in terms of understanding the underlying phenomena that govern the fundamental cutting process. This is of particular importance in process planning and tool design. The most common titanium alloy in the aerospace industry is Ti6Al4V and is thus the focus of this study.

The objective of this study is to develop and implement numerical models that allow investigation of machining Ti6Al4V. The focus is on implementing practical models or tools which can give insight into the underlying mechanisms when titanium is machined orthogonally as well as the ability predict cutting forces in more complex machining operations such as milling. The study is not aimed at investigating the mechanism governing machining but rather at establishing competency and analysis tools for further studies.

A finite element machining model is implemented to model the orthogonal or 2D cutting case and a mechanistic model is implemented for force prediction of milling operations. The FE model is used here to predict cutting forces and temperatures during machining and is used to establish an orthogonal cutting database which is used as an input for the unified mechanic of cutting model which is implemented in this study to model ball nose milling. The FE model is useful in understanding the relative sensitivities of machining parameters and the influence of the constitutive material model used. It allows allows for in depth analysis of the load distribution on a cutting edge, heat generation in the cutting system, chip morphology and workpiece residual stresses.The model may be extended to model cutting of a variety of other materials but is implemented here only for Ti6Al4V

The unified mechanics of cutting is implemented, in this study, to predict cutting forces in ball nose milling. The model however, can be used to model any machining operation and requires only that the tool geometry be defined in the model. The model is implemented using as an input orthogonal cutting databases assembled from cutting test data obtained in literature [69], orthogonal turning test performed in this study and from the predictions of the finite element orthogonal cutting model. The model is implemented with two milling tool geometries, a constant lead ball-nose mill and a modern ball nose mill whose geometry is initially unknown and determined from geometric touch probe measurements. The models are validated against experimental data obtained in literature and machining tests performed in this study.

Chapter 2

Background

This chapter provides a broad background for the study in terms of basic machining theory and more specifically the machining of Ti6Al4V. It also introduces the relavent modelling work conducted by researchers on the subject and the modelling approaches used in this study. As stated in the problem definition, the modelling approach is two-fold and the literature and theory of the FE and Unified mechanstic models are described in more detail in the relevant chapters (Chapters 4 and 6).

2.1 Titanium alloys

Titanium alloys are known as light alloys due to their low density and can be divided into two groups: corrosion resistant alloys and structural alloys. The distinction arises through differences in crystallography, in terms of the constituent α and β phases, through the uses of various alloying elements.

- Corrosion resistant alloys are usually based on a plain α stage with stabilizing elements such as oxygen, palladium or aluminium. These materials are generally used in the chemical, energy, paper processing and food industries in the forms of corrosion resistant pipes, valves and heat exchangers.
- Structural alloys are in turn sub-divided into three categories: close α alloys, β alloys, and α-β alloys [3].

  Close α alloys are characterized by their resistance to fatigue at high temperatures, and are used mainly in internal combustion turbines at more than $600^{\circ}C$.

  High strength β alloys such Ti10V2Fe3Al are used in applications which demand a high strength at relatively low temperatures.

  The α-β alloys are generally structural alloys and are widely used in structures and engine components in aerospace industries. The alloy, Ti6A14V, falls within this group and is the most widely known of the titanium alloys. It has a good combination of mechanical properties at temperatures over $315^{\circ}C$ when in an aged state. Ti6Al4V is thus the most popular alloy for aircraft components under low thermal stresses and thus forms the basis of this study.

2.2 Ti6Al4V properties

In the aerospace industry highly corrosion resistant alloys account for 25% of cases where titanium is used. Ti6Al4V is used about 60% of the time and the other structural alloys account for the remaining 15%. Titanium is available in two states of hardness preparation, precipitation hardened or aged condition.

Table 2.1 compares some of the physical properties of Ti6Al4V with those of inconel and steel. It can be seen that titanium has relatively low thermal conductivity, low density and high strength. It also has a high melting point, hardness and a high ratio of yield stress to tensile strength $R_{p0.2}/R_m = 0.9$. It has a low Young's modulus and will deflect more than steel under load. Titanium also has a high thermal capacity $C = 520\,\mathrm{J/kgK}$ and is highly reactive with small elements such as oxygen, nitrogen and hydrogen, resulting in embrittlement. Due to its high reactivity, titanium reacts with all known cutting materials including polycrystalline diamond, ceramics (PCD), tungsten carbide (WC) and polycrystalline boron nitride (PCBN) [1].

Table 2.1: Properties of three common aerospace materials

	Melting point (°C)	Thermal conductivity (W/mK)	Density (g/cm3)	Modulus E (GPa)	Hardness (HB)
Tiś6Alś4V	1670	7.1	4.43	115	350
Inconel 718	1453	11.4	8.22	200	300
Steel CK 45	1535	51.2	7.84	210	180

2.3 Machining theory and basics

Orthogonal cutting or machining represents the simplest expression of machining in that it is a two-dimensional cutting configuration in which the cutting edge is perpendicular to the direction of cutting velocity. Orthogonal cutting is illustrated in Figure2.1. In orthogonal machining the cutting and feed forces are in the direction of the cutting velocity V_c, and perpendicular to it, respectively. In a turning operation the forces are thus in the tangential and radial directions. The rake angle, α, is the angle between the tool rake face and a perpendicular from the surface being machined. The relief or clearance angle γ is the angle between the flank face of the tool and the machined surface. The feed, t, is the uncut chip thickness and t_c is the cut chip thickness. ϕ is the shear angle, and is the angle at which the workpiece material shears during machining. Shear angle is of significance as it affects the machining forces in that a decreasing shear angle increases the shear area and results in an increase in cutting forces and the direction of the resultant force is altered. The cut chip thickness is also increased, as well as the contact length, which is denoted by L_c and is the length of contact between the chip and tool rake face.

According to Merchant the shear stress, τ, in orthogonal machining can be found by calculating the shear angle from equation2.1(b), where r is the ratio of cut to uncut chip thickness, and substituting into 2.1(a) along with cutting and feed forces F_{Pc} and F_{Qc},

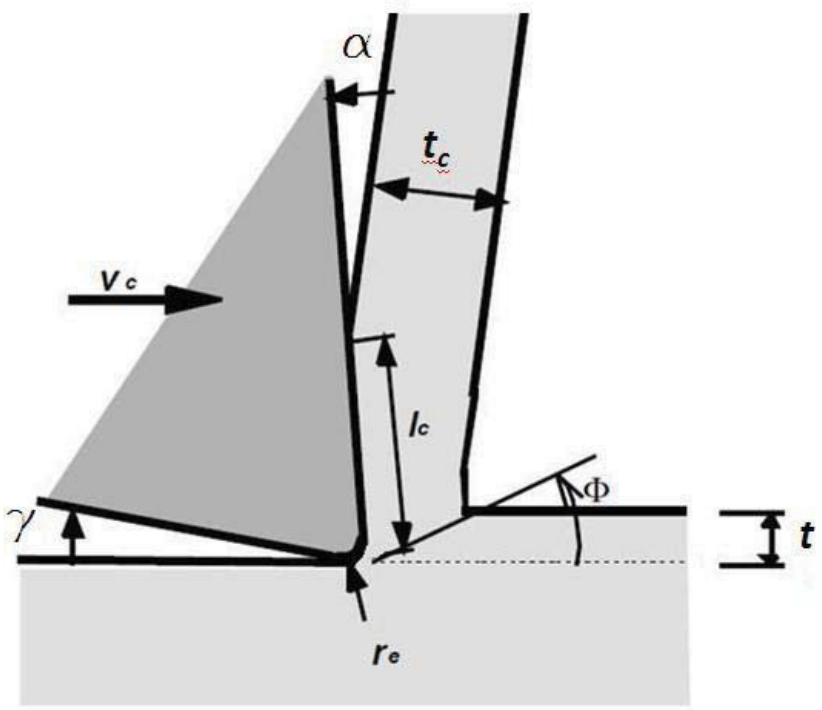

Figure 2.1: Orthogonal cutting geometry

cut width, b and thickness, t. The friction angle, β can be calculated from equation 2.1(c) [2].

$$\tau = \frac{(F_{Pc}\cos\phi - F_{Qc}\sin\phi)\sin\phi}{bt} \quad (a)$$

$$\tan\phi = \frac{r\cos\alpha}{1 - r\sin\alpha} \quad (c) \qquad (2.1)$$

$$\tan\beta = \frac{F_{Qc} + F_{Pc}\tan\alpha}{F_{Pc} + F_{Qc}\tan\alpha} \quad (c)$$

Oblique cutting, on the other hand, represents the cutting case in which the cutting edge is inclined to the velocity vector. In practical machining operations, cutting is usually performed using oblique cutting, as this aids chip evacuation through the generation of a spiral chip due to the angle of the cutting edge. The oblique configuration thus produces a third force component which is not present in orthogonal machining.

2.4 Segmental chip formation

In aluminium cutting, the chip formed in the machining operation is of a continuous nature at all but the highest cutting speeds, where it may become segmented depending on the cutting conditions. Titanium, on the other hand, exhibits segmented chip formation at all but the lowest speeds and this has been cited as the cause of much confusion and inconsistency in interpreting cutting data pre-1980s [3]. Merchant's two-dimensional cutting model was used from the 50s through to the 80s when modelling

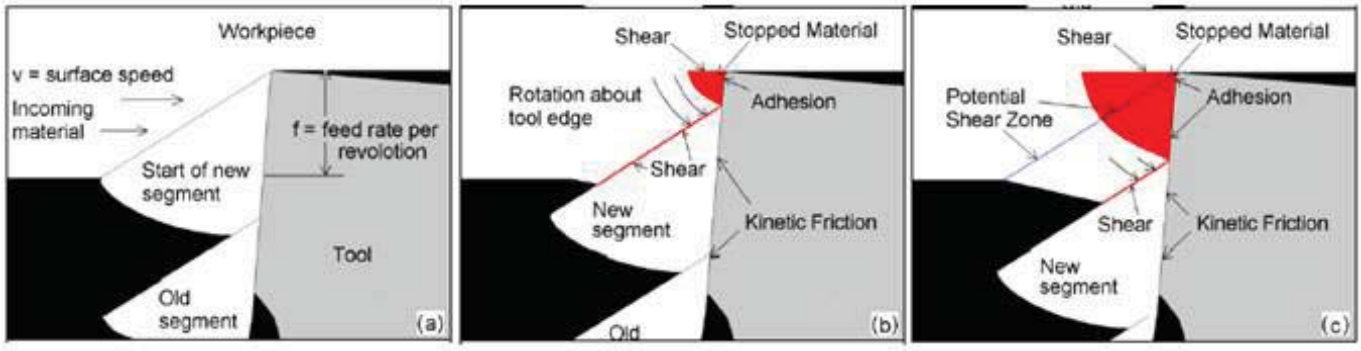

Figure 2.2: Chip segmentation process in titanium machining [3]

and analyzing Titanium cutting, but in 1981 Komanduri and Von Turkovich proposed the new shear-localised chip formation using experimental evidence from low speed SEM (1.2mm/min) and high speed (240m/min) high resolution video experiments for orthogonal cutting [4].

Segmented or adiabatic shear-localised chip formation occurs in two stages. In the first stage the wedge shaped un-deformed chip (Figures 2.2a and 2.2b) is flattened by the advancing tool. This occurs with little deformation of the chip and almost no relative motion between chip and tool. The chip bulges and in the second stage (Figure 2.2c) plastic instability leads to strain localization along the shear surface and the new chip segment is formed through catastrophic shear along a localized shear plane. This event occurs rapidly and the low thermal conductivity of titanium prevents heat from moving out of this band, resulting in high local temperatures in this region. The origin of the shear plane formed is parallel to the cutting vector and curves upwards until it reaches the surface of the material as in Figure 2.3 [4], while others have proposed a flat shear plane as represented in Figure 2.2. The chip is pushed along this trajectory, advancing the previous segement along the tool face.

In this process the cutter is continuously exposed to the freshly formed shear surface which is characterised by high temperatures which results increased chemical reactivity between the workpiece and tool material. As the chip is deformed in the first stage, there is little shear between the chip and tool as the chip rolls onto the surface of the tool. There is thus little secondary deformation along the tool rake face, as is evident in continuous chip formation. Chip formation thus occurs on a narrow region of the tool and causes high local temperatures at the tool edge, resulting in accelerated wear. This is unlike the continuous chip formation process where a primary shear band exist, across which some of the plastic deformation occurs as well as a secondary deformation zone, further from the tool tip, where secondary plastic deformation occurs [3].

The surfaces defined in Figure 2.3 1.3 are referred to as, (1) undeformed surfaces, (2) catastrophic shear failed surface, (3) shear band formed during upsetting stage of segment formation, (4) intensely sheared surface slid onto tool surface, (5) intense localized deformation in localized shear zone and (6) the machined surface [8].

In the achievement of high machining efficiency in commercial machining, tool life and Material Removal Rate (MMR) are two of the most important factors. There are generally two approaches to achieving high MRR. The first is known as high speed machining and the second is as high performance machining.

In high speed machining, high MRR is achieved by machining at a combination of high

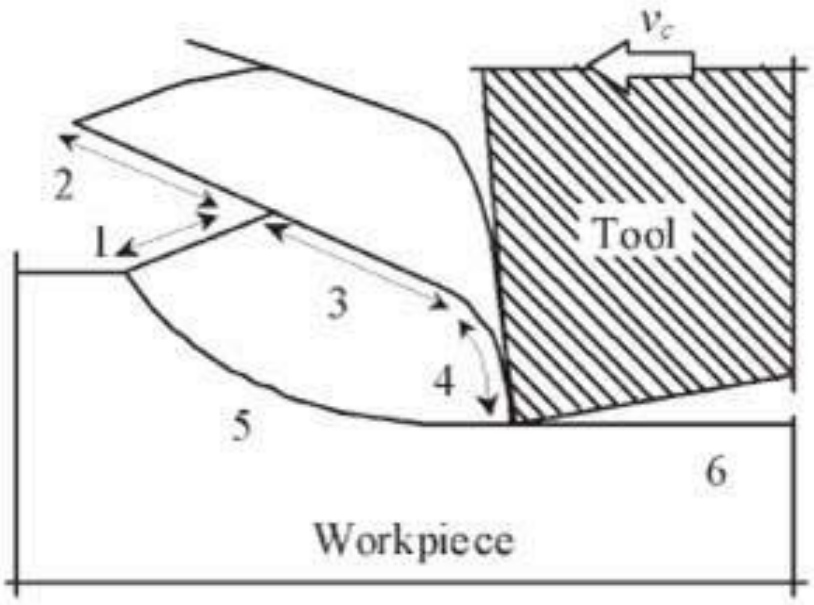

Figure 2.3: Definition of surfaces in segmented chip formation [3]

speed cutting with low feeds or thickness of cut and depths of cut. In general, when machining with increasing cutting speed, cutting forces and temperatures are initially observed to increase to a local maximum and then decrease, followed by a steady increase. This was first observed by the inventor of high speed machining, C. Salomon [5]. From Figure 2.4 it can be seen that there is a transition range of cutting speed where machining is not advisable, as cutting forces and temperatures are too high for the tool and work piece. HSM is generally in the order of 5 to 10 times the conventional cutting speed and, besides the obvious productivity benefits, it is capable of producing high quality surface finishes, low stress components and burr-free edges. Temperature effects on the workpiece and tool are reduced in some cases, with an increase in tool life [5]. In titanium machining, however, temperatures continue to increase with cutting speed and, therefore much research is currently being conducted in tool materials capable of withstanding these temperatures so that practical high speed machining may be realized.

High performance machining, on the other hand, achieves high MRR by machining at lower cutting speeds, but employing high feed rates and depths of cut. Traditionally, when cutting titanium, specifically in roughing operations, HPM machining is regarded as the most practical approach which, however, poses its own difficulties in that machining forces are high due to the high chip loads and material strength. In general, machining forces are approximately proportional to cut width and thickness and so a combination of large feeds and depth of cut, or high chip load, results in high cutting forces. HPM machining thus necessitates the use of sturdy, high powered machining centres.

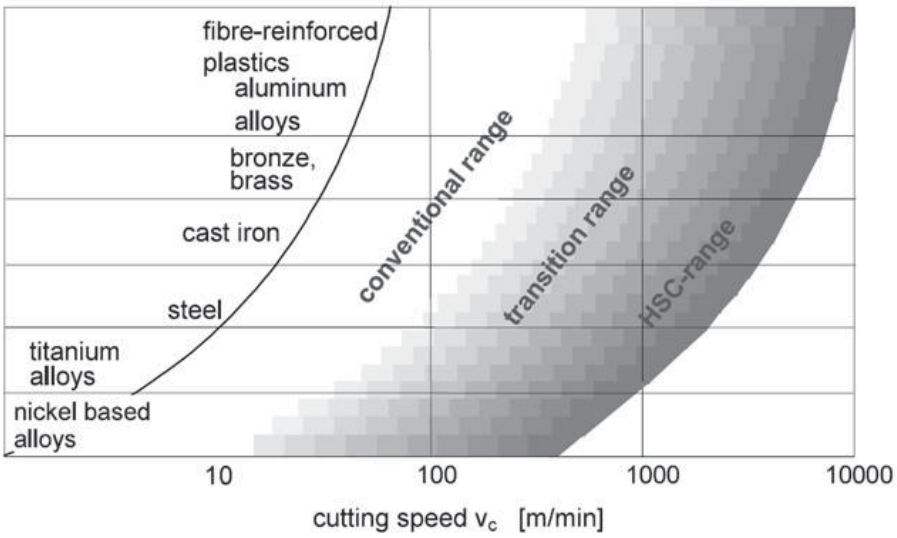

Figure 2.4: High speed machining ranges for various materials [3]

2.5 Modelling metal cutting

According to Ng et al, analytical metal cutting models define the relations between cutting force components based on the cutting geometry [6]. These models are easy to use if prior knowledge of the cutting angles (shear, friction, and chip flow) is available. However, the chip formation mechanism in HSM is dependent on the machining parameters and workpiece material. Variations in the chip flow angle induced by cutting speed could reduce the accuracy and repeatability of the results obtained. Moreover, when including all the necessary boundary conditions describing the HSM process, the mathematical equations could become so complicated that a solution is no longer possible. In general, the theory of plasticity leads to an analytically non-solvable set of equations when work hardening is taken into consideration or when the workpiece geometry is non-trivial [7]. The approach to modelling metal cutting thus is often by the use of finite element models, as well as empirical and mechanistic models.

2.5.1 FEA modelling of metal cutting

A large deal of work has been produced on the FE modelling of metal cutting, but with relatively little emphasis placed on modelling segmental chip formation. Many of these FE models have shown that cutting force predictions can be made with reasonable accuracy and have shown the ability to simulate the localized-shear chip formation present in titanium cutting. With the possibility of a fully coupled thermo-mechanical model of the workpiece and tool, FE models have the ability to model dynamic and residual stresses, as well as temperatures in the tool and workpiece [8][9].

FE simulation of the metal cutting process is no trivial matter though, and is dependent on accurate modelling of material, friction and thermal conditions of the tool-workpiece system. The strain rates and associated temperatures present in metal cutting exceed those of most other common industrial processes. The accurate determination of material properties at these conditions is therefore of importance and some researchers have even proposed machining tests to develop more accurate material

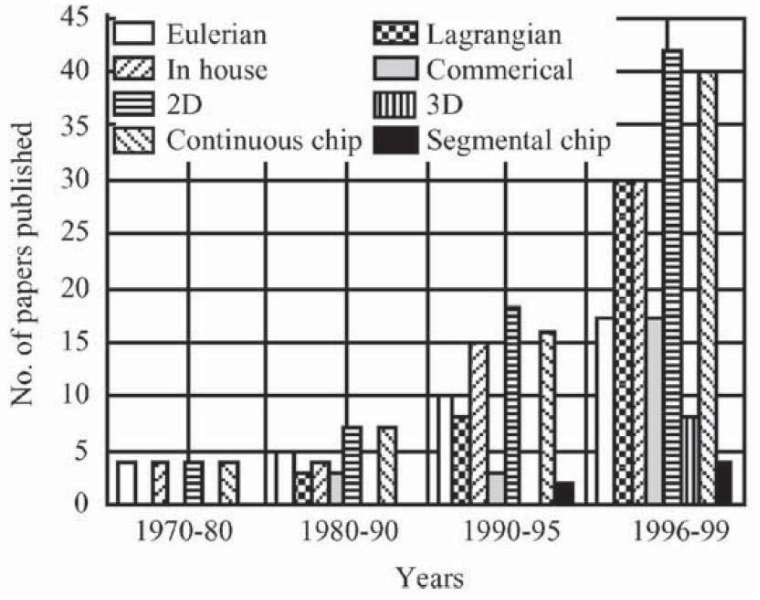

Figure 2.5: Literature survey of fem cutting models [6]

models under high strain rates [10].

There are many approaches to modelling the cutting process. Successful models have been implemented for 2D orthogonal machining, 3D oblique and full 3D cutting simulations for milling, gear hobbing, drilling and a variety of other cutting processes. The titanium cutting process has been modelled using both implicit and explicit formulations, though some authors have insisted on the use of full dynamic explicit, thermo-coupled simulations with efficient remeshing [11].

In FE modelling there are two fundamental approaches to modelling chip formation, the Lagrangian or displacement formulation, in which the mesh is embedded in the material and is constrained to move with it and the Eulerian or flow formulation which assumes a fixed mesh in space [11]. The main advantages of the Lagrangian formulation are that the chip geometry is the result of simulations and presents a simpler scheme to simulate transient processes and segmented chip formation. Due to the large deformations at the shear zone, adaptive remeshing may be implemented to prevent largely distorted elements when using the Lagrangian formulation. This is done at discrete steps in the simulation or when convergence problems are experienced [12].

Eulerian approaches, on the other hand, do not require remeshing to prevent element distortions. Furthermore this approach allows steady state machining to be simulated with no element or nodal separation scheme. The main disadvantage of this method is that the chip geometry needs to be known in advance, although iterative procedures have been developed to adjust chip geometry and tool-chip contact length [12]. Some models have attempted to mitigate the shortcomings of the two formulations by employing an Eulerian formulation for the moving chip and a Lagrangian formulation for the stationary material and moving tool (the distortions on the tool and workpiece are relatively small compared with those of the chip formation) [13].

In FEM simulations of metal cutting, material models which describe the material properties, such as flow stress and strength, as a function of the temperature, strain and strain rate are generally employed. Several models exist, such as the Johnson-Cook,

Oxley and Maekawa but they all fail in some respect to accurately describe the material properties, though the models may be calibrated using test data [14].

Friction modelling is generally through the coulomb or modified coulomb friction model and the effect of friction on the cutting process has been demonstrated to be increased tool and chip temperatures and an increase in cutting forces. This effect on cutting force is great and simulations have indicated a 20% increase in forces when a frictional coefficient of 0.1 is introduced. Friction has an effect on chip shape and formation, as well as an effect on machining force [15].

Full 3D simulation of the milling operation is computationally expensive for practical cutting scheme optimisation, as every cutter geometry and cutting condition needs to be modelled and simulated. On the other hand, 2D orthogonal simulations are much cheaper to perform computationally and have been shown to predict cutting forces with good accuracy.

2.5.2 Mechanistic modelling of machining

Traditionally, cutting force prediction by empirical modelling relates the average cutting forces obtained experimentally to process variables such as cutting speed, depth of cut and other process variables through empirical curve fitting techniques [16]. These methods have been applied to turning, drilling and milling, but are more suited to continuous operations such as turning and drilling, where cutting forces are not expected to vary cyclically, as is the case with milling.

Semi-empirical or mechanistic approaches have been implemented for milling operations where tool forces vary as a function of instantaneous chip thickness [17]. In these approaches, milling force component coefficients are obtained through a series of cutting tests performed for each material and tool geometry combination to be modelled and related to the chip load using empirical techniques. The model identifies six edge coefficients K_{tc}, K_{rc} and K_{ac} which are the tangential, radial and axial cutting force coefficients and K_{te}, K_{re} and K_{ae} are the tangential, radial and axial edge force coefficients, respectively. The first three coefficients represent those forces due to cutting in the Cartesian coordinates, while the second group represents the forces due to friction and ploughing. Together they describe the forces acting on a specific cutter and can be used in a mechanistic model to predict the varying cutting forces and power requirements during a revolution of the cutter [18]. Despite the usefulness and accuracy that these models have demonstrated, the cutting tests must be repeated for each workpiece material and tool geometry combination. This can be a costly and time consuming process when one considers the cost of titanium and cutter inserts.

The unified mechanics of cutting approach differs from the mechanistic approach in that the cutting force coefficients are determined from oblique or orthogonal cutting tests. The cutting tests are performed by varying cutting parameters such as feed rate, rake angle and cutting speed and measuring the cutting forces and chip thickness. This data is incorporated into a database and used to predict the elemental cutting coefficients at a given cutting condition. The cutting forces can then be predicted at any point along an arbitrary cutting flute for a given cutting condition, so that cutting forces may be predicted from orthogonal data for an arbitrary cutter geometry. The machining forces are separated into edge or ploughing forces and shearing forces. The helical flutes are divided into small differential oblique cutting edge segments. The orthogonal

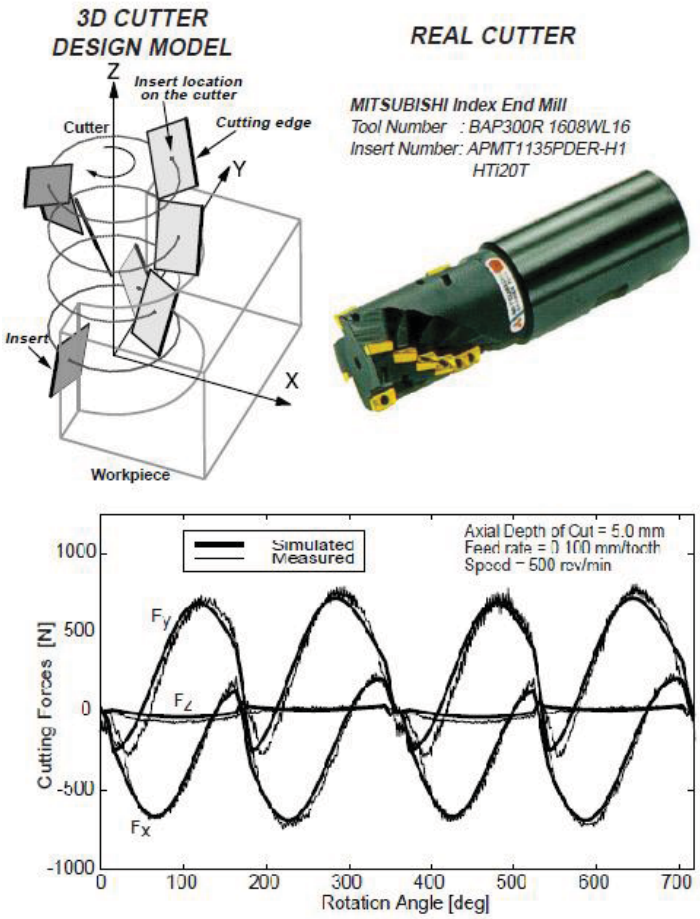

Figure 2.6: Unified mechanistic model applied to an inserted end mill for cutting force predictions [22]

cutting parameters are converted to oblique milling edge geometry using the classical oblique transformation method.

Several important studies in formulating the mechanistic and dynamic models, utilising the "unified cutting model", have been performed. These include the mechanistic description and experimental verification of various milling cutters such as helical end mills [19], ball end mills [20], generalized end mills [21] and general inserted cutters [22], with good results. The accuracy has also been experimentally verified for the prediction of cutting forces when machining Ti6Al4V for a range of chatter, eccentricity and run-out free conditions [22]. Figure 2.6 is taken from [22] where an inserted cutter of any geometry may be defined in a mechanistic model which simulates cutting forces from an orthogonal database. The model predicts the measured forces well and the method is implemented in this study to model ball nose milling.

Although these models have proved to be accurate, it can be an expensive and time consuming exercise to compile the required data and a new set of orthogonal data is needed for different materials to be modelled. Furthermore, these models provide no information on the variation of cutting forces due to the segmented chip formation process or temperatures and stresses in the tool and workpiece during and post machining. It is thus important to have the ability to predict orthogonal cutting data by other means, such as finite element analysis. In view of the previous paragraphs,

the implementation of a hybrid cutting force model is proposed in which the cutting force coefficients are to be determined through FE simulations of the orthogonal cutting process. In this scheme the orthogonal or FE cutting models are used to predict the mechanistic cutting force coefficients and are then used in the mechanistic models to predict cutting forces in any machining operation.

2.6 Summary and document layout

In Chapter 3, the experimental and test work is described with a brief discussion of the results. The Discussion is limited as the results are discussed in more detail in the chapters that follow, where the results are compared with the predictions made using the FE and mechanistic cutting models.

The following Chapter 4, details the orthogonal FE cutting model implemented to simulate titanium machining and compares predicted machining forces, temperatures and chip geometry with experimental results from orthogonal turning tests.

Chapter 6 describes the "unified" mechanics of cutting model applied to ball nose endmills. It compares the results of predictions made using both experimental and FEA orthogonal cutting data in the milling model, to those of the milling tests conducted and results from literature.

Chapter 7 concludes the document and gives results of the study. It also makes recommendations as to the continuation of the research and improvements that can be made.

Chapter 3

Test procedure

A number of tests were conducted for the purpose of this study. All tests were performed using the same material, namely test specimens from a Ti6Al4V, ASTM grade 5 bar. The material was obtained from Titanium Fabrication Corporation in the form of a 75 mm bar of length 300 mm. Table 3.1 summarises the mechanical material properties for this grade at room temperature.

Table 3.1: Physical properties

Property	values	unit
Tensile Strength	895	MPa (min)
Yield Strength	828	Mpa (min)
Modulus of elasticity	105-120	Gpa
Elongation	10	%

Micro-hardness tests were conducted to determine the hardness profile through the diameter of the bar. Material hardness can also be related to yield strength of the material and thus provides a way of determining this property without conducting tensile tests. Optical and SEM microscopy was performed at each indentation site to investigate the crystal structure associated with each hardness test. EDS analysis was conducted to determine the chemical composition as a matter of interest.

Turning tests were conducted to measure the cutting forces under various cutting conditions. Other data collected from these tests were chip samples for geometric comparison with FEA models and the chip thickness, which is required for use in the mechanistic milling model. Chip microscopy was performed on all chip samples in a raw (as machined) state and also in a mounted, sectioned and etched stat, so that micro structure and geometric features could be examined. Chip underside temperature was also measured for selected cutting conditions, again for comparison with FEA models.

Slot milling tests were carried out using a ball nose end mill at various cutting conditions to measure milling forces for comparison with mechanistic milling model predictions.

3.1 Material analysis

Micro hardness tests were conducted to determine the hardness profile through the diameter of the bar. These tests were conducted using a Wilson Wolpert micro hardness tester with Vickers indenter and a 1 kg load.

To perform the hardness tests a 5 mm radial slice or disc was cut from the bar using an EDM cutter, ensuring that no work hardening occurred on the surface of the test sample. A rectangular section of $40x15$ mm was then cut from the disc so that it could be mounte nd SEM microsc moplas- tic and ranging from 40 rries of silica ca

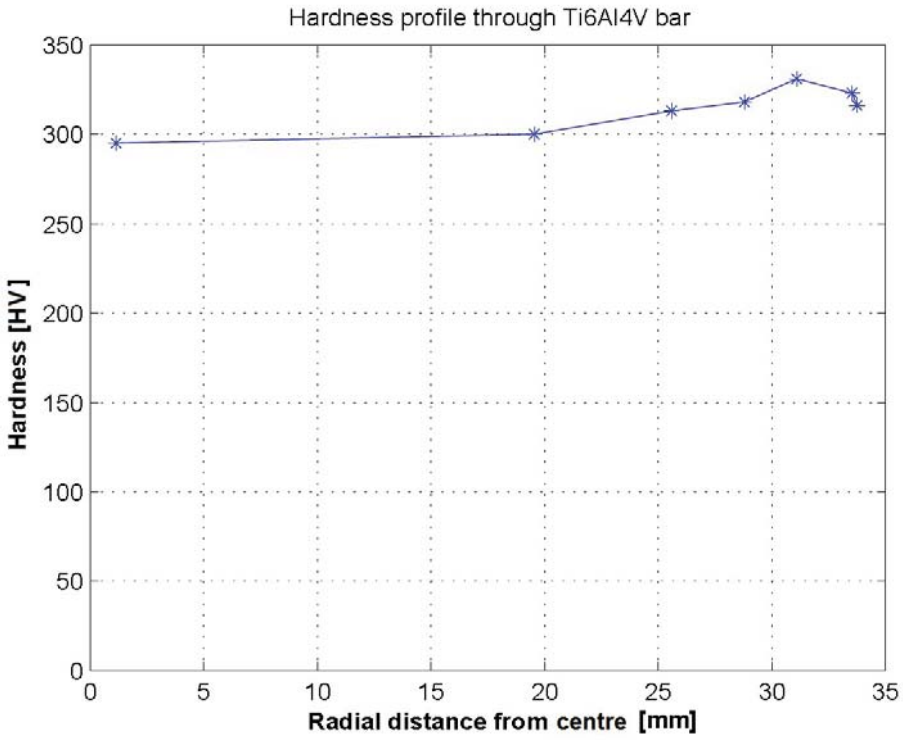

Figure 3.1: Hardness profile across the radius of the titanium bar

Hardness tests were carried out at seven sites through the radius of the bar and the hardness profile in Figure 3.1was obtained. The hardness is observed to increase exponentially towards the outside of the bar and a maximum hardness of HV 331 is obtained 5mm from the surface of the bar but then decreases to a value of HV 316 at the surface of the bar. The hardness through the material varies by no more than 10 % through the radius of the bar and would therefore not affect the results of machining tests significantly. This was later verified by conducting a radial plunging operation on the turning setup, which is described in Section 3.2, whilst measuring cutting and feed forces.

Vickers hardness can be related to yield strength, according to Yavuz and Tekka [23] with the relation $\sigma_y = HV/2.9$ at an equivalent plastic strain of 0.08. This gives a

yield strength range of 997.9 to 1119.7 MPa for the measured sites, which is considerably higher than the manufacturer quoted value of 828 MPa. Knowledge of the yield strength is of use in determining sensible constants for J-C material model described in Chapter 4.

Following the hardness tests, the specimen was etched so that the microstructure at each of the test sites could be examined. Etching was achieved using a solution of Kroll's reagent. The specimen was submerged in the solution for a period of 2 seconds which was sufficient to reveal the microstructure of the sample material. Optical microscopy was conducted, using a Zeiss Axiotech microscope with an Axiocam sensor, operating on Axiovision software.

The microstructure can be described as having an elongated α phase in a fine dark-etching β matrix. The microstructure varies considerably through the radius of the bar with a finer structure near the edges and a higher β phase concentration. Toward the centre of the bar, the α phase becomes more distinct and the β matrix surrounds these grains. SEM analysis revealed no further information and is ommitted here for brevity.

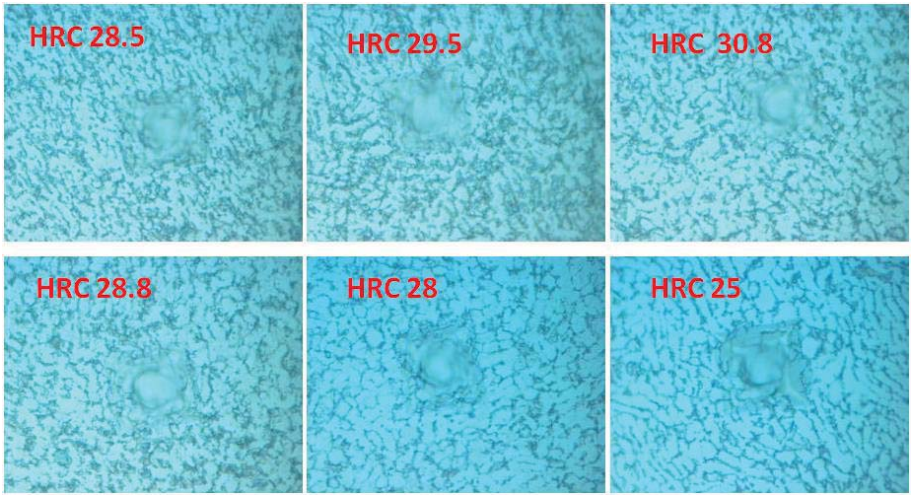

Figure 3.2: Micro structure at indentation sites

EDS analysis was conducted to determine the chemical composition of the titanium sample. A high amount of carbon was found to be present in the alloy while the vanadium and titanium concentrations were lower than expected. This may be attributed to the etching solution, which may be more reactive with certain materials than others. EDS analysis, however, showed a good correlation with the stated composition of the material.

Table 3.2: Material composition from EDS analysis

Element	Weight%	Area%
C	7.12	21.25
N	2.76	7.06
Al	7.42	9.87
Ti	80.36	60.17
V	2.35	1.65

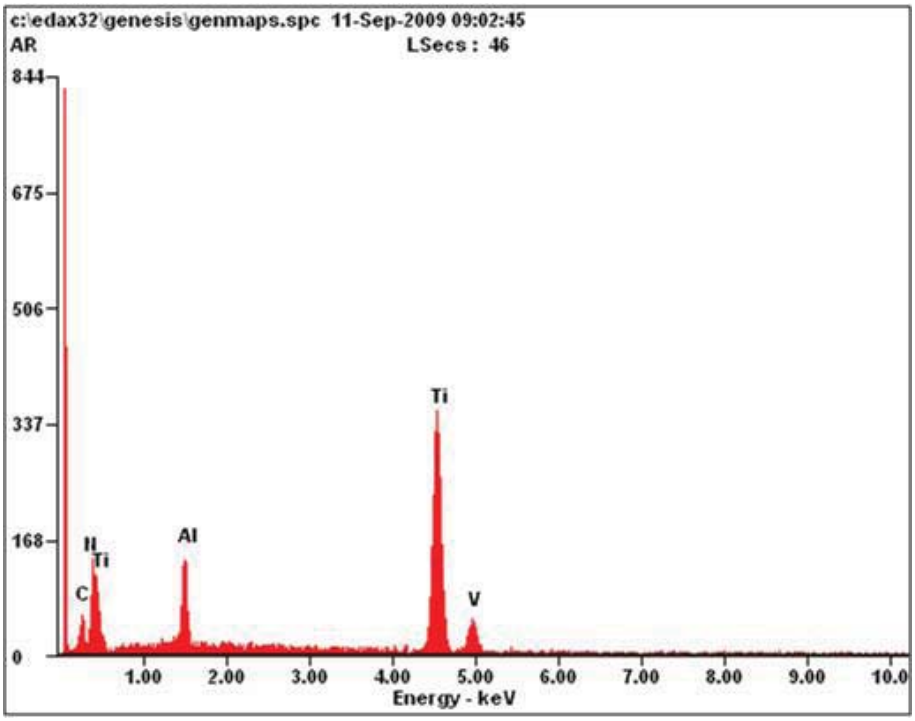

Figure 3.3: EDS analysis of the titanium bar

3.2 Turning tests

Turning tests were conducted for the purpose of validating the FE models and to assemble the orthogonal cutting database for milling force predictions using the "unified" mechanics model described in Chapter 6. The database requires that orthogonal turning tests be performed at a variety of feeds, cutting speeds and rake angles corresponding to the milling conditions which are to be simulated. To this end turning tests were conducted at speeds ranging from 15 m/min to 200 m/min and feeds ranging from 0.005 mm to 0.3 mm. Figure 3.4 shows the cutting conditions under which tests were carried out for both zero and five degree rake angles. Cutting was conducted without cooling to simplify the FE analysis in that cooling of the cutter and chip due to conduction and convection can be omitted from the model.

3.2.1 Test setup

The turning tests were conducted using an Oerlikon-Boehringer type PNE 480, inclined bed, CNC Lathe. Some of its pertinent technical specifications are listed in Table 3.3. This is considered to be a stiff machine and little vibration and no chatter was evident during testing.

To measure machining forces, the toolholder is mounted on a 3 component Kistler 9265B dynamometer so that forces applied to the tool may be measured. The dynamometer measures forces in the three principal directions using piezoelectric quartz crystals, which generate an electrical charge when subjected to strain through an applied external loading to the dynamometer.The dynamometer has a total range of ± 15 kN in the x and y direction and $0 - 30$ kN in the vertical or z direction. It has a calibrated

Table 3.3: Oerlikon Boehringer CNC lathe specifications

CNC control	Fanuc type oi-TB
Country of origin	Germany
spindle drive	34 kW
max spindle torque	1000 Nm
turning diameter	350 mm
turning length	1000 mm
turning speed range	14 - 3550 U/min
longitudinal feed	0,1 - 6000 mm/min
cross feed	0,1 - 6000 mm/min

Figure 3.4: Test setup on the Oerlikon Boehringer CNC lathe

partial range of $0 - 1.5$ kN in x and y and $0 - 3$ kN in the z direction with linearity better than 0.5 %. The natural frequency of the dynamometer occurs at 2.5 kHz which is well suited to measuring the dynamic forces present in machining.

The charge from the dynamometer is amplified through a Kistler type 5019a multi-channel charge amplifier. At the output of the amplifier the voltage corresponds to the force, depending on the scaling parameters set in the charge amplifier. The interface hardware module consists of a National Instruments BNC-2110 connecting plan block, and a multi-channel A/D interface board. In the A/D board, the analogue signal is transformed into a digital signal so that the TLC software is able to read and receive the data. The voltages are converted into forces in x, y and z directions by the TLC program. The TLC software is a custom made "continuous monitoring and analysis" package by TLC software and is designed to capture data from the dynamomter, and temperature measurement systems.

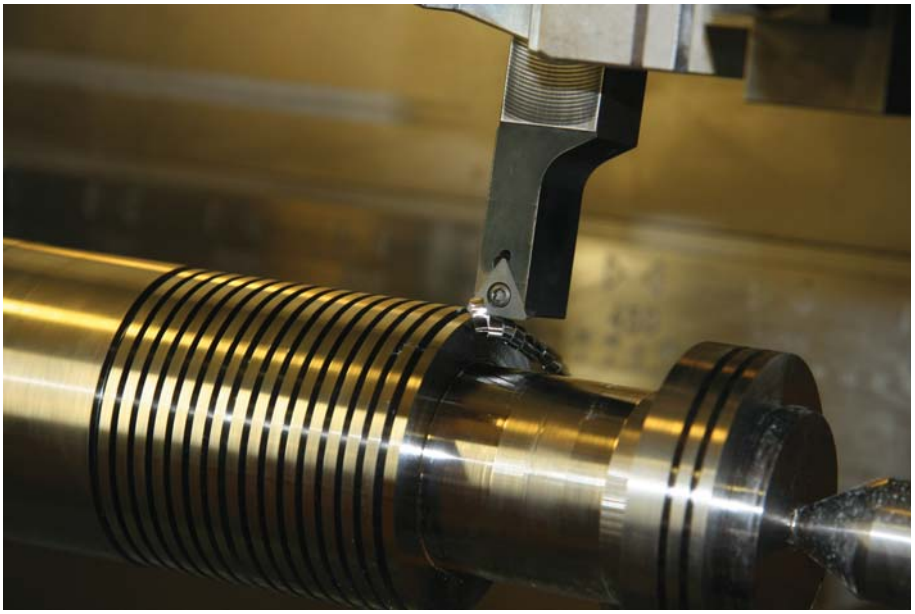

Figure 3.5: Orthogonal turning test configuration

3.2.2 Tool holder and insert

The turning operation is a radial plunge operation in which the tool is fed radially into a pre-grooved bar. The grooves on the bar provide clearance for the tool nose radius so that the insert cuts only along a portion of the straight edge in a typical orthogonal machining configuration. The bar was grooved using a 2 mm grooving/parting tool at 5 mm intervals so that a series of 3 mm discs were obtained for turning tests to be conducted. Figure 3.5 shows a disc being machined.

In order to perform orthogonal cutting, a tool with a zero entry or inclination angle was selected from the Sandvik range, which ensured that the cutting edge of the tool was perpendicular to the direction of feed and thus only tangential and radial force components are generated, with the axial component being negligible. The selected tool holder is the CoroTurn 107 Screw clamp unit, designated STFCL 2020M 11-AB1. CoroTurn 107 triangular uncoated carbide inserts were used for all turning tests. The inserts have a sharp cutting edge, 7° clearance angle and a flat rake face with no chip breaker. The inserts measure 16mm from corner to corner, are 3.97 mm thick and have a nose radius of 0.8 mm. The carbide grade used is Sandvik's H13A grade which is an uncoated sintered carbide with good abrasive wear resistance and toughness and is recommended for use in machining heat resistant alloys such as titanium under moderate cutting speeds and feeds.

The tool holder and insert had no rake angle but was later modified to incorporate a 5° rake so that milling predictions could be performed for mills with both zero and 5° rake angles. This was done by cutting a 5° wedge from the bottom of the tool holder shank with an EDM cutter. The wedge was then glued to the top surface of the shank, using cyano-acrylate, to produce the desired rake angle. Figure 3.6 shows the arrangement.

Figure 3.6: Tool modification for 5° rake angle

3.2.3 Force measurements

Force measurements were conducted not only to satisfy the requirements of the mechanistic model, but also for comparison with FEA models. Very small feeds were considered so that edge forces could be found by extrapolating cutting and feed forces to zero cut thickness; this is a requirement of the "unified" mechanics model. High feed rate tests were conducted so that the HPM region could be investigated. Feeds were limited to a maximum of 0.3 mm in this study as rapid tool failure occurred at higher rates in the form of tool chipping and rapid tool wear.

High cutting speeds were also investigated so that the HSM could be characterized to some degree. Speeds were limited to 200 m/min due to chip combustion under dry cutting conditions at a cutting speed of 300 m/min; however temperature measurements were conducted at this cutting speed. Tool wear at high speeds was also very high and this resulted in difficulties in obtaining reliable force data. Wear rates were prohibitively high at a combination of high cutting speed and high feed rate and this region of cutting conditions was not considered, as it does not represent practical machining conditions. Tool wear manifested itself as an increase in feed forces, after an initial reduction with tool break in. Tool wear does not form part of this study and all tests were thus conducted with a new insert or one with negligible wear.

The tests were conducted with the standard tool holder described and then repeated with the tool holder modified for 5° rake angle. This allows for validation of FEM predictions in terms of the effect of rake angle on cutting forces and also allows for the prediction of milling operations for tools with rake angles within this range.

Cutting and feed forces increase almost linearly with increasing feed, while cutting speed, on the other hand, has very little effect. At very low speeds (15 m/s), a slight increase in machining forces is observed which may be attributed to a reduction in thermal softening effect at the low temperatures associated with this cutting speed ($375°C$ see section 3.2.4).

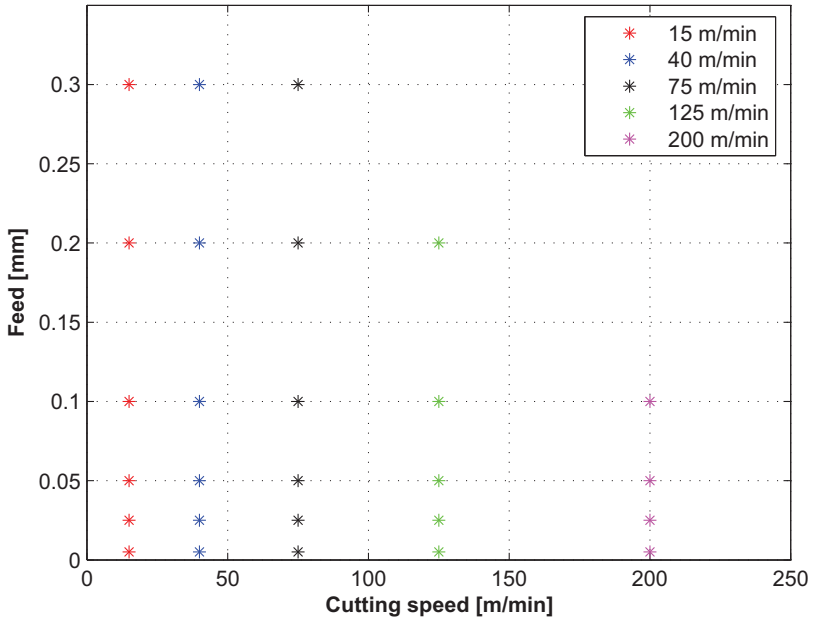

Figure 3.7: Cutting conditions for orthogonal turning tests

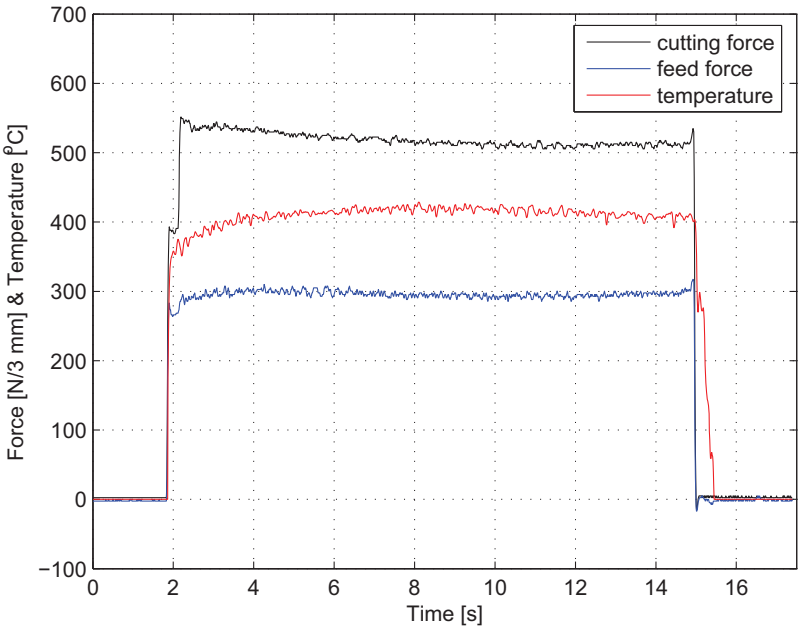

Figure 3.8: Machining forces and temperature for 3 mm cut width at v=40 m/min; feed=0.1 mm/rev

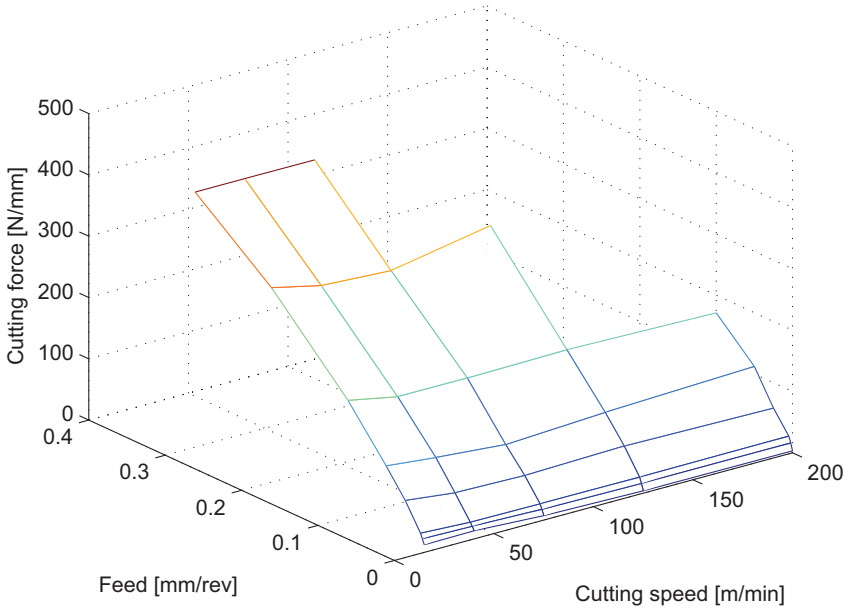

Figure 3.9: Measured cutting forces [N] in orhtogonal turning

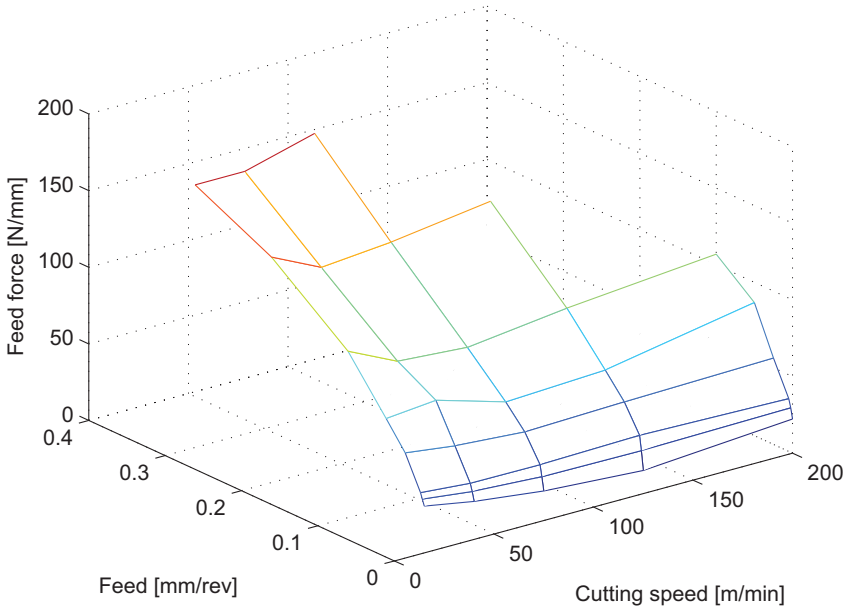

Figure 3.10: Measured feed forces [N] in orhtogonal turning

In Figure 3.11 it can be seen that at very low feed rates there remain residual machining forces referred to as edge forces. These are the forces associated with rubbing and ploughing in cutting and are generated through friction at the cutting edge and ploughing of the workpiece material due to the radius of the cutting edge. These forces are found by extrapolating machining forces to zero cut thickness or feed. The cutting or shear forces forces are taken as the machining forces minus the edge forces and represent those forces in machining which are due to shearing of the material in the chip formation process. This data is used in the milling models to establish the orthogonal database and a detailed description can be found in Chapter 6.

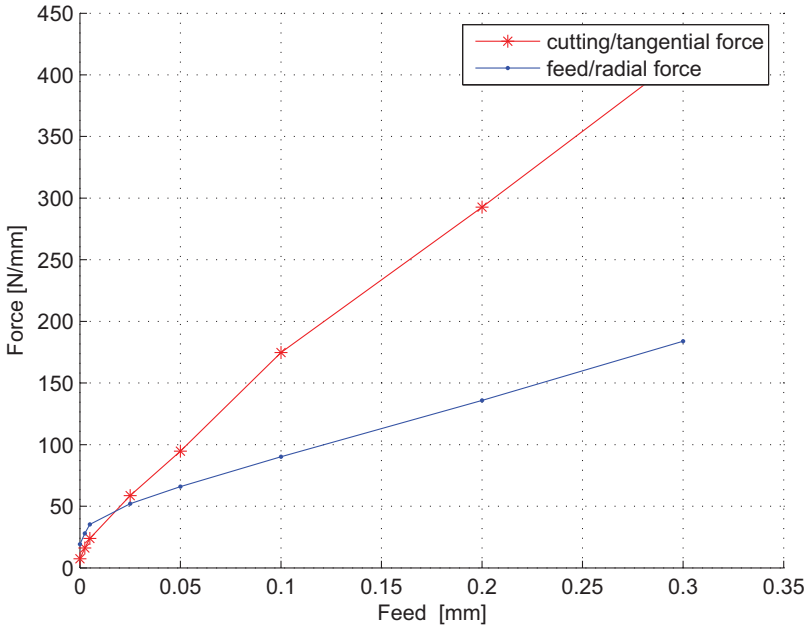

Figure 3.11: Machining forces vs. feed at V=40 m/min in orhtogonal turning

3.2.4 Temperature measurements

Chip temperature measurements were conducted using the Pyro2 infrared temperature measurement instrument that uses a fibre optic system with two colour infrared lighting to measure temperatures up to 1600 K with a resolution of 1°C and an accuracy of 2%. Tests were carried out using the turning setup for force measurements, with modifications to the tool holder and inserts to accommodate the fibre optic system.

The optic fibre is inserted in a hole, laser drilled perpendicular to the top surface, near the cutting edge and measures the temperature of the chip underside as it passes. This measurement is also indicative of tool temperatures at this location. The hole has a 0.2 mm diameter and is situated 1 mm from the cutting edge.

Temperatures were measured for a speed range of 5 m/min to 300 m/min and feeds of 0.05 mm and 0.1 mm. In Figure 3.12 a steady increase in temperature with increasing cutting speed is observed, due to the increased strain rates at higher speeds and a resultant increase in heat addition into the system. Feed has negligible effect on the

temperatures observed, as chip load plays only a small role and the temperatures at the two feeds showed very close correlation. At cutting speeds of 300 m/min, energetic chip combustion occurred under dry cutting conditions, and cutting speeds could thus not be increased due to the fire hazard imposed.

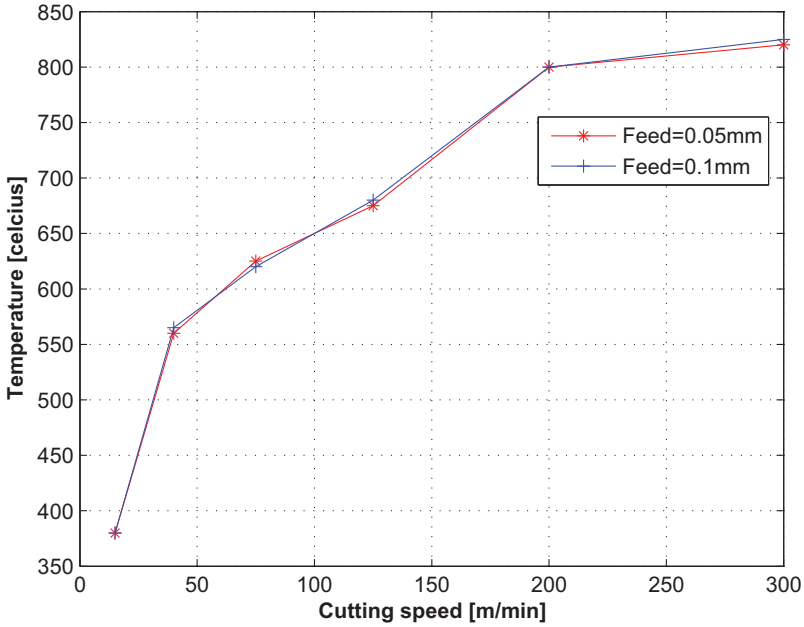

Figure 3.12: Chip temperatures measured in orhtogonal turning

3.2.5 Chip Microscopy

Chip samples were collected for each of the orthogonal turning tests so that microscope analysis could be performed. Data collected from this exercise is used in the mechanistic models, uncut to cut thickness ratio, and for comparison with FEA models in terms of geometry such as chip shape, segmentation period, shear angle and shear band size.

In preparation for optical microscopy the chips were mounted in resin so that polishing and etching could be performed. The chips were mounted on their edges with their machined surface perpendicular to the viewing plane so that the chips could be examined in section. Polishing and etching was conducted using the same procedure as in section 3.1.

3.3 Milling tests

Fifty ball nose slot milling tests were conducted to measure milling forces for comparison with predictions from the unified mechanics of cutting model. Tests were conducted on a Johnford VMC-1050 4-axis vertical machining centre with the material mounted on a three component dynamometer shown in Figure 3.13. The machining centre has a maximum spindle speed of 8000 rpm with a power rating of 8 hp. CNC control is achieved with the use of a Fanuc type oi-MC controller.

Figure 3.13: Johnford milling centre with dynamometer and titanium test pieces mounted

Material for the milling tests was obtained, as in section 3.1, by EDM cutting discs from the same titanium bar used in turning and hardness tests. The titanium discs were bolted to the top surface of the dynamometer, which in turn was mounted on the bed of the machining centre. The arrangement is shown in Figure 3.14. Slot milling was performed by milling across the tops of the titanium discs with a ball nose cutter at various axial depths of cut and feed rates. In the case of partial radial immersion tests, a rectangular slot was first milled into the material to allow for the appropriate clearance required.

Tooling consisted of a Sandvik carbide ball nose end-mill, CoroTurn R216. The tool has a 12 mm diameter, a 1° rake angle and a 30° helix angle. The mill has two cutting flutes, one of which was ground away so that testing could be conducted with a single cutting edge. In milling with tools with two or more oblique cutting flutes, each flute is in cut for more than 180° in the case of full immersion slotting. This is due to the helix angle of the flutes which results in an overlap of cutting forces from the flutes when one is entering the cut and the other exiting. For sake of simplicity, and to avoid potential cutter eccentricity problems, tests were thus conducted with a single flute tool.

A feed range of $0.025 - 0.2$ mm and axial immersion of 1 mm to 6 mm in 1 mm increments, were used for the slotting tests. All tests were conducted at 240 rpm to reduce tool temperature and combat wear under dry cutting conditions. Partial radial immersion tests were conducted in both up and down milling configurations at 50% immersion at a variety of axial immersions at a single feed rate.

Figure 3.15 shows a sample force trace for a ball nose slotting operation obtained from tests. Here X is in the radial direction aligned with the direction of tool advance, Y is the radial direction perpendicular to X and Z is in the axial direction. This coordinate system is used in Chapter 6 where the milling model is implemented.

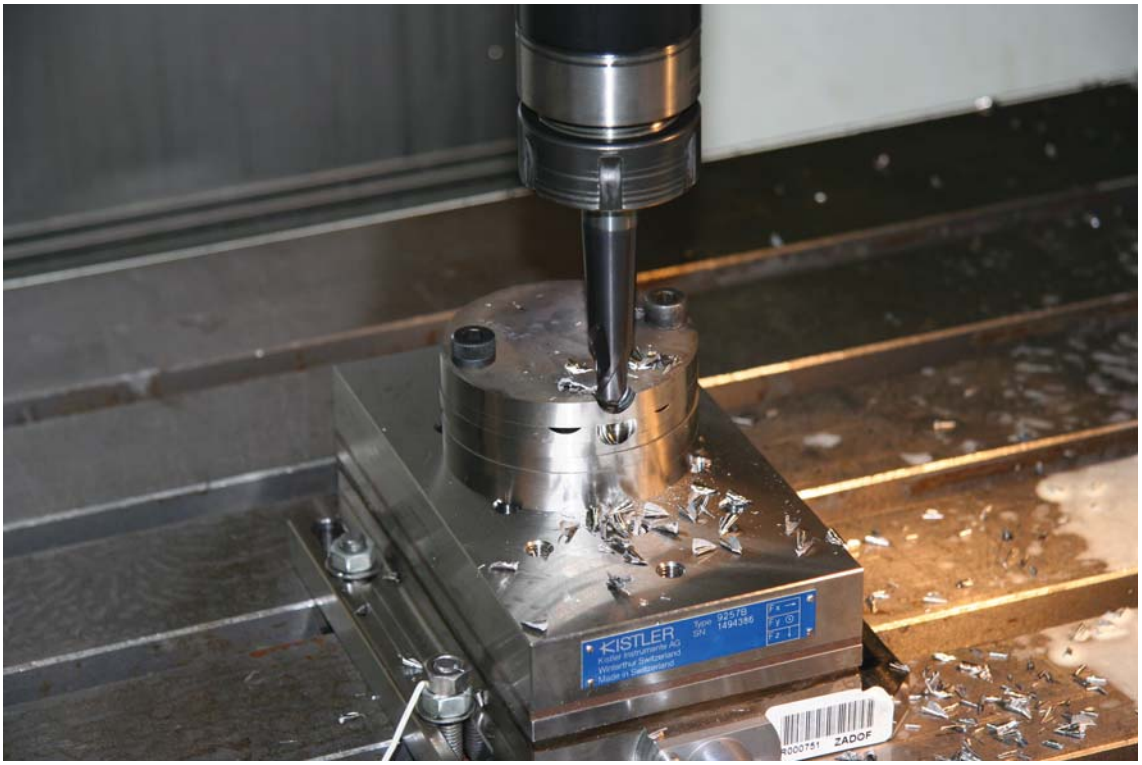

Figure 3.14: Milling test setup

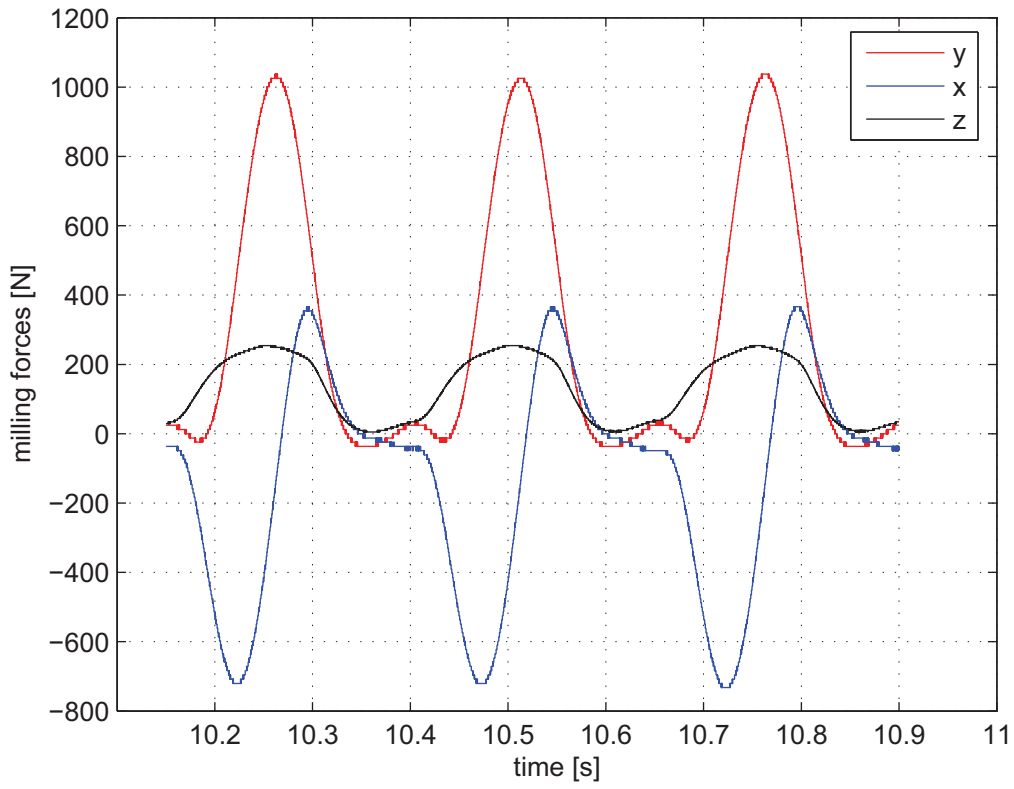

Figure 3.15: Ball nose milling test: slot milling; feed:0.1 mm/rev; depth=4 mm; 240 rpm

Chapter 4

Finite element orthogonal cutting model

Finite element modelling of metal cutting has been achieved to a greater or lesser degree by various methods ranging from implicit to explicit integration schemes and using Eulerian, Lagrangian and mixed Eulerian-Lagrangian formulations.

Finite element formulations can be classified as either quasi-static implicit or dynamic explicit time integration schemes. Implicit formulations require convergence at every time step or load increment while explicit formulation solves an uncoupled equation system based on information from the previous time step [24]. The use of finite element modelling to simulate machining processes dates back to the early 70's with the work of Okushima and Kakino [25] and Tay et al. [26]. Tay used an Eulerian formulation which is an implicit scheme in which the the finite element grid is fixed spatially and material particles are allowed cross grid boundaries. This formulation is thus also commonly referred to as the flow formulation and is utilized to model the flow of the chip from the workpiece. The Eulerian formulation can be described by

$$\vec{K}_{n+1}\Delta\vec{\mu}_{n+1} = \vec{F}_{n+1} \tag{4.1}$$

$$\vec{\mu}_{n+1} = \vec{\mu}_n + \Delta\vec{\mu}_{n+1} \tag{4.2}$$

in which $\vec{K}_{n+1}$ is the stiffness matrix, $\Delta\vec{\mu}_{n+1}$ is the vector of unknown incremental velocities, $\vec{F}_{n+1}$ is the load vector and $\vec{\mu}_{n+1}$ and $\vec{\mu}_n$ are the current and previous total nodal velocities. When applied to machining problems, this method requires knowledge of the chip thickness and shear angle from experimental work to determine chip geometry. It can also only be used in steady-state simulations and so only continuous type chips can be modelled using this method [24]. The major benefits of using the Eulerian formulation is that no chip separation criteria are required (see Lagrangian formulation) and fewer elements are required to specify the chip and workpiece, thereby reducing the computation time. Another advantage is that there is no need to simulate the lengthy transition from incipient to steady state cutting conditions as in Lagrangian formulations. In implicit algorithms, the requirement of convergence at every solution increment provides better accuracy.

The disadvantage of using such an approach is that experimental work must be carried

out in order to determine the chip geometry in terms of the ratio of cut to uncut chip thickness or shear angle. Furthermore, only continuous chip formation can be modelled using this approach so the method is not suitable for modelling titanium chip formation. This formulation is also unable to deal effectively with segmental and discontinuous chip formation and its restrictive contact conditions are also drawbacks of this scheme.

The Lagrangian formulation can be expressed as both quasi-static implicit and dynamic explicit time integration schemes. In recent years much of the focus has moved to the use of Lagrangian formulations, due to the ability of this approach to model dynamic problems as well as segmental and discontinuous chip formation. The finite element equations for the quasi-static implicit Lagrangian formulations can be written as

$$\vec{K}_{n+1}\Delta\vec{\mu}_{n+1} = \vec{F}_{n+1} \tag{4.3}$$

$$\vec{\mu}_{n+1} = \vec{\mu}_n + \Delta\vec{\mu}_{n+1} \tag{4.4}$$

in which $\vec{K}_{n+1}$ is the stiffness matrix, $\Delta\vec{\mu}_{n+1}$ is the vector of unknown incremental displacements, $\vec{F}_{n+1}$ is the load vector and $\vec{\mu}_{n+1}$ and $\vec{\mu}_n$ are the current and previous nodal displacements [24].

Implicit schemes can be used for simulation of continuous chip formation due to simple requirements of frictional contact. On the other hand, complex geometry and contact detection/interaction of discontinuous chip formation recommends the use of explicit schemes. Dynamic explicit time integration schemes have been employed in metal forming problems which involve high non-linearity, complex friction-contact conditions and fragmentation [27][28][24]. The explicit finite element equations can be expressed as

$$\vec{M}_{n+1}\ddot{\vec{\mu}}_n + \vec{C}_{n+1}\dot{\vec{\mu}}_n + \vec{P}(\vec{\mu}) = \vec{F}(t_n) \tag{4.5}$$

$$\vec{\mu}_{n+1} = \vec{\mu}_1 + \Delta\vec{\mu}_{n+1}(\Delta t, \ddot{\vec{\mu}}_n, \dot{\vec{\mu}}_n) \tag{4.6}$$

where $\ddot{\vec{\mu}}$, $\dot{\vec{\mu}}$ and $\vec{\mu}$ are the nodal acceleration, velocity and displacement at time t_n, M and C are mass and damping matrices and P and F are internal and external forces [24]. Although no iterative procedure is required, the time step size affects the stability of the solution and is invariably much smaller than that of the implicit formulation. The time step is a function of the time it takes for a stress wave to pass through the smallest element and mesh refinement therefore results in an increase in solution increments.

The main advantages of this scheme is that the chip geometry is a result of the simulation, so that no experimental work needs to be conducted as in the Eulerian scheme. Furthermore, it is possible to model continuous, segmented and discontinuous chip formation using this method.

The Lagrangian formulation has some significant disadvantages, however. The first is the requirement of chip separation from the parent or workpiece material. This has been an area of much discussion and several solutions exist, such as nodal separation or element deletion along a predetermined cutting line as well as adaptive and continuous remeshing schemes. The other major disadvantage of this scheme is that of large element distortions, which affects the solution accuracy or may result in the simulation

failing and being dumped.

Usui et al. [29] produced one of the first FE models with the ability to model segmental chip formation in 1984, using the Lagrangian formulation. The model employed "in-house" FEM code to simulate orthogonal machining of titanium alloys and makes use of a fracture criteria for crack nucleation and growth to model segmental chip formation, through nodal separation. Chip separation is again achieved by node separation along a parting line. The Fracture criterion used is a function of plastic strain, strain rate, fracture strain, hydrostatic pressure and cutting speed.

In the mid 1990s, Marusich and Ortiz [28] developed an improved Lagrangian model with a fracture criterion based on workpiece toughness and critical crack distance. The criteria were applied not only to the depth of cut but also within the deformed chip for a given stress magnitude, enabling nucleation and propagation of a crack through the chip. Continuous and adaptive remeshing was used to reduce element distortion and achieve chip separation. The FE code was again "in-house" software which was later developed into the commercial Windows based software package, AdvantEdge^{TM} for the simulation of orthogonal machining.

Table 4.1 details the capabilities of the various formulations applied to machining models. From this it can be seen that the explicit Lagrangian model is the only method suited to the modelling of segmental chip formation observed in titanium machining.

Table 4.1: Strains and strain rates associated with common processes

	Eulerian	Updated Lagrangian	Arbitrary Lagrangian Eulerian
Nodal location	fixed	moving and deforms with material	Fixed and moving
solver	implicit	implicit or explicit	explicit
cutting stage	continuous	continuous & incipient	continuous
chip type	continuous	continuous, segmented and discontinuous	continuous
nodal separation or element deletion	no	yes & no (remesh)	no
chip geometry prediction	no	yes	yes
residual stress prediction	no	yes	yes
tool nose radius	yes	yes & no (remesh)	yes

Over 70% of researchers used "in-house" finite element code up until the mid 1990s, however in recent years there has been a dramatic increase in the number of commercial software packages capable of simulating metal cutting such as NIKE2D^{TM}, ABAQUS/Standard^{TM}, MARC^{TM}, DEFORM 2D^{TM}, FORGE 2D^{TM}, ALGOR^{TM}, FLUENT^{TM}, ABAQUS/Explicit^{TM} and LS DYNA^{TM} [30]. However the choice of formulation type, chip separation method, fracture criterion, remeshing ability, material models are dependant on the software package. The choice of software thus determines the capabilities of the FE model to a large degree.

In this study the decision was made to use ABAQUS/explicit^{TM} due to several factors. The package is a general FE program which may be customized through the use of 'user sub-routines', and although sub-routines were not used in this study, they allow

for further development of the model in terms of user defined material models and the incorporation of remeshing schemes. Furthermore, it is a popular and powerful platform and its use was a requirement of one of the sponsors of this study (Element Six), because of their use of the software.

4.1 Updated Lagrangian orthogonal cutting model description

The model developed in this study is a dynamic explicit Lagrangian model with temperature-displacement coupling so that heat flux and conduction between the tool and work may be included in the model. Chip separation from the workpiece and segmental chip formation through crack growth and adiabatic shear banding is modelled using elements which fail according to the Johnson Cook or J-C fracture criteria and flow stress is modelled using the J-C material model. These material models are described in 4.1.1. All other aspects of the orthogonal cutting model are discussed in the following sections. Thermal aspects such as heat generation and conduction are discussed in section 4.1.2 while friction and contact issues are dealt with in section 4.1.3.

4.1.1 Material modelling

According to Johnson and Cook [31], materials subjected to dynamic loading conditions such as high velocity impact, explosive detonation and metal forming operations are subject to a wide range of strains, strain rates, temperatures and pressures. In many instances there has been a tendency to distinguish between dynamic and static properties, where the difference is due to strain rate alone. However, large strains, pressures and temperatures are associated with high strain rates and it is therefore important that the effects of all these variables are accounted for.

Metal machining represents a combination of the highest strains, strain rates and temperatures found in common metal forming processes. Table 4.2 lists the values of strain, strain rate and the ratio of process temperature to material melting temperatures associated with some common metal forming operations. Titanium exhibits behaviour that is dependent of all these parameters and, as such, modelling titanium machining requires a material model which accounts for these factors.

Table 4.2: Strains, strain rates and temperatures associated with common processes [32]

Process	Strain	Strain rate $[s^{-1}]$	$T_h = (t)/(t_{melt})$
Extrusion	$2-5$	10^1-10^2	$0.16-0.7$
Forging/rolling	$0.1-0.5$	$100-10^3$	$0.16-0.7$
Sheet-metal forging	$0.1-0.5$	$100-10^2$	$0.6-0.7$
Machining	$1-10$	10^3-10^6	$0.16-0.9$

In FE modelling of metal machining, a wide range of constitutive material models have been employed to model the workpiece behaviour. In general, these can be described as rigid-plastic, rigid-viscoplastic, elasto-perfectly-plastic, elasto-plastic and elasto-viscoplastic. Elasto-plastic and elasto-viscoplastic are the most commonly used materials and account for elastic as well as plastic deformations. The elasto-viscoplastic

model accounts for plastic strain rate, while the elasto-plastic model has no rate dependency. Both of the models can, however, model springback effects, thermal strains and residual stress [24].

The elasto-viscoplastic model has been adopted by Shih [33][34][35][36], while Iwata et al. [37] adopted a rigid-plastic model. A rigid-viscoplastic model was used by Kim and Sin [38], Joshi et al. [39], Skhon and Chenot [40], Eldridge et al. [41], Strenkowski and Moon [42], Carrol and Strenkowski [8] and Wu et al. [43]. The use of rigid-viscoplastic material models can simplify the analysis as no elastic deformation is allowed, however thermal strains, residual stresses and spring-back effects cannot be evaluated using these models.

Xie et al., [44] Vaz Jr. et al., 1998a [45]; Vaz Jr. et al., 1998b [46]; Owen and Vaz Jr. [47] and Obikawa and Usui [48] made use of specialised material models to model adiabatic shear-banding and fracture when machining Ti6Al4V titanium alloy. Adiabatic shear localisation, which can cause material failure, is caused by thermal softening in materials of low thermal diffusivity or in high-speed processes. Vaz Jr. et al. [46] introduced the use of a two-parameter model to describe material failure due to shear banding, with the use of a failure indicator and an energy release factor. The failure indicator defines the onset of failure and the energy release factor is a damage progression relation which defines the amount of energy released by the element during the softening process before the actual element failure [24].

This study makes use of the Johnson-Cook plasticity model which is widely employed in FE cutting and ballistic models [6]. The J-C material model is typically used in transient adiabatic FE simulations to model flow stress and was introduced in 1983 by Johnson and Cook [49] for modelling problems such as ballistic impacts and metal machining. The J-C material model is a phenomenological relation, in that it is not based on traditional plasticity theory. It reproduces several important material responses at high deformation rates and is thus a popular model for FE simulations which involve high strain rate deformation. It is an elastic-plastic, Von Mises stress model with analytical forms of the hardening law, as well as rate and temperature dependence. The model was developed in conjunction with the Johnson-Cook fracture model [31], which is intended to show the relative effects of various parameters and attempts to account for path dependency by accumulating damage as the deformation proceeds, and is primarily dependent on the strain, strain rate, temperature and pressure.

The parameters for the Johnson-Cook material model may be obtained by several methods: high-speed compression tests, Split Hopkinson Pressure Bar (SHPB) tests, practical machining tests, integration of conventional tests at low strain rates and machining tests combined with inverse analysis using FEA techniques [49].

High speed compression tests often employ a punch driven by compressed air to compress specimens at high speed, resulting in strain rates in the order of $450s^{-1}$ [49]. Specimens may be pre-heated in a furnace to obtain flow stress at elevated temperatures, however, the heating rate is considerably lower than those obtained in practical machining and may thus introduce age hardening or anneal softening of the material.

The Split Hopkinson Pressure Bar SHPB technique was introduced in the early 20th century to study material behaviour at high strain rates. With this technique the specimen is placed between two lengthy compression bars one of which is referred to as the input bar. A striker bar is propelled toward the input bar at high velocity and upon impact, an elastic stress wave is induced in the input bar. The wave travels along the

length of the bar and is transferred to the sample resulting in deformation of the specimen. The strain histories for the incident and transmitted waves in the elastic pressure bars are measured and analysed to determine the nominal stress-strain and strain-rate response of the samples. This may also be accompanied by high speed photographic analysis and other methods. The SHPB technique is also used to determine material failure parameters [31].

Flow stress modelling

The formulation for the J-C model is empirically based and represents the flow stress with an equation of the form

$$\sigma_{flow} = \overbrace{(A + B(\epsilon_{pl})^n)}^{strain}\overbrace{(1 + Clog(\dot{\epsilon}_{pl}/\dot{\epsilon}_{ref}))}^{strainrate}\overbrace{(1 - T^m)}^{temperature} \tag{4.7}$$

where

$$T = (t - t_{tr})/(t_{melt} - t_{tr}) \tag{4.8}$$

where t is the current temperature, t_{melt} is the melting temperature, and t_{tr} is the transition temperature defined as the temperature at, or below which, there is no temperature dependence on the expression of the yield stress. The material parameters must be measured at or below the transition temperature. A, B, n and m are material parameters measured at or below the transition temperature. The first part of 4.7 is the strain dependent component, while the second part is a strain rate modifier which introduces strain rate hardening. The third part is a temperature dependent component which accounts for thermal softening of the material at elevated temperatures.

The strength of the material is thus a function of strain, strain rate, and temperature. The model assumes that the strength is isotropic and independent of mean stress. The values of A, B, C, n, and m are determined from an empirical fit of flow stress data as a function of strain, strain rate, and temperature to 4.7.

When $t = t_{melt}$, the material will be melted and will behave like a fluid and there will be no shear resistance. The hardening memory will thus be removed by setting the equivalent plastic strain to zero. $\dot{\epsilon}_{ref}$ is the reference plastic strain rate, which is generally normalized to a strain rate of $1s^{-1}$.

Table 4.3 gives a sample of J-C flow stress model parameters for Ti6Al4V found in literature. The data shows a large variation in these coefficients which can be attributed, in part, to the variations in actual material properties which are due to variations in post processing of the material, such as heat treatment. Sample preparation and grain orientation also play a role, while other variations are due to the method, and inherent variability, of the test procedure used in acquiring the model parameters [57]. In this study only the J-C material parameters found by Johnson and Holmquist [10] were considered and are used in all FE model predictions. The material constants reported by Johnson [58] were fitted based on eight torsion tests, four SPHB tests, and two quasi-static tensile tests, while the others used the SHPB tests only. Furthermore, the material used in their study is of HRC30 Ti6Al4V with no heat treatment and is thus similar to the material used in this study (see section 3.1).

Table 4.3: A sample of Johnson Cook coefficients from literature

Source	A [MPa]	B [MPa]	n	C	m
Lee and Lin [50]	782.7	498.4	0.28	0.028	1
Dumitrescu et al [51]	870	990	0.25	0.011	1
Khan [52]	1080	1007	0.5975	0.01304	0.7701
Lesuer [53]	1098	1092	0.93	0.014	1.1
Macdougall and Harding [54]	984.0	520.3	0.5102	0.01500	0.8242
Nemat-Nasser et al.[55]	1119	838.6	0.4734	0.01921	0.6437
Johnson and Holmquist [10]	862	331	0.34	0.012	0.8
Songwon Seo et al. [56]	997.9	653.1	0.45	0.0198	0.7

To investigate and illustrate the workings of the J-C model and its sensitivity to the various material parameters or coefficients, each component (strain, strain rate and thermal) is now considered in turn. In Figures 4.1-4.4 the sensitivity of the first component is investigated. With B and n fixed and A varied, it can be shown that A determines the initial plastic flow stress magnitude at zero plastic strain and is thus similar to the yield stress of a material when strain rate and thermal effects are ignored. A has no effect on the gradient or hardening response of the curve and simply scales its magnitude.

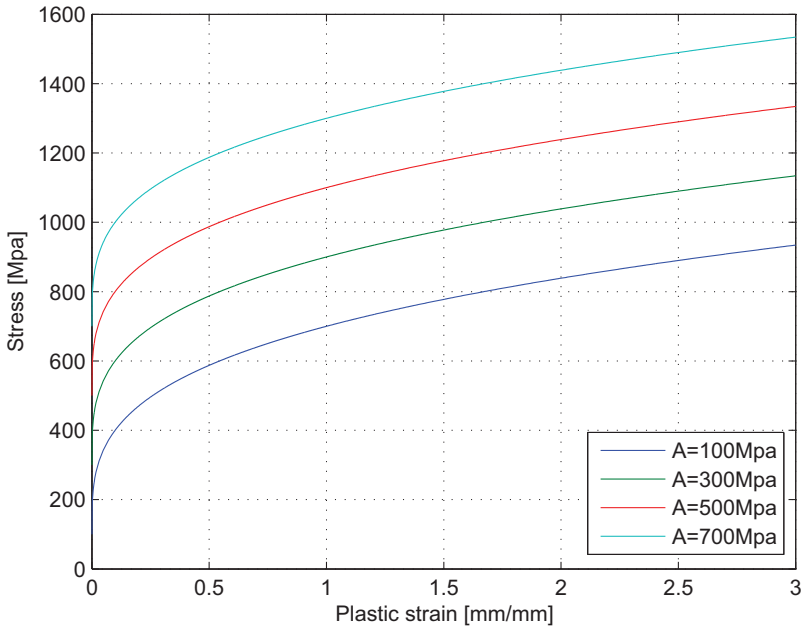

Figure 4.1: Flow stress vs plastic strain for $A + B(\epsilon_{pl})^n$ with $B = 600$ MPa and $n = 0.3$

When A and n are held constant ($A = 400$ MPa and $n = 0.1$) and B is varied, as illustrated in figure 4.2, it can be shown that an increase in B elevates the flow stress magnitude at values of plastic strain which are larger than zero. Furthermore, B has an influence on the strain hardening gradient in that an increase in B increases the gradient of the material hardening response.

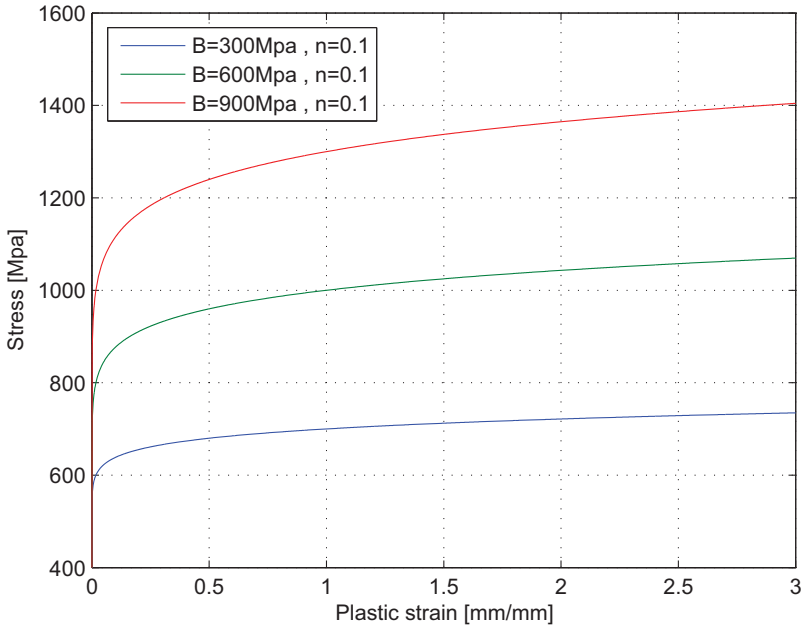

Figure 4.2: Flow stress vs plastic strain for $A + B(\epsilon_{pl})^n$ with $A = 400$ MPa

In Figure 4.3, when the strain index is increased to $n = 0.3$, the sensitivity to strain hardening is increased through an increase in the gradient of the flow stress curve.

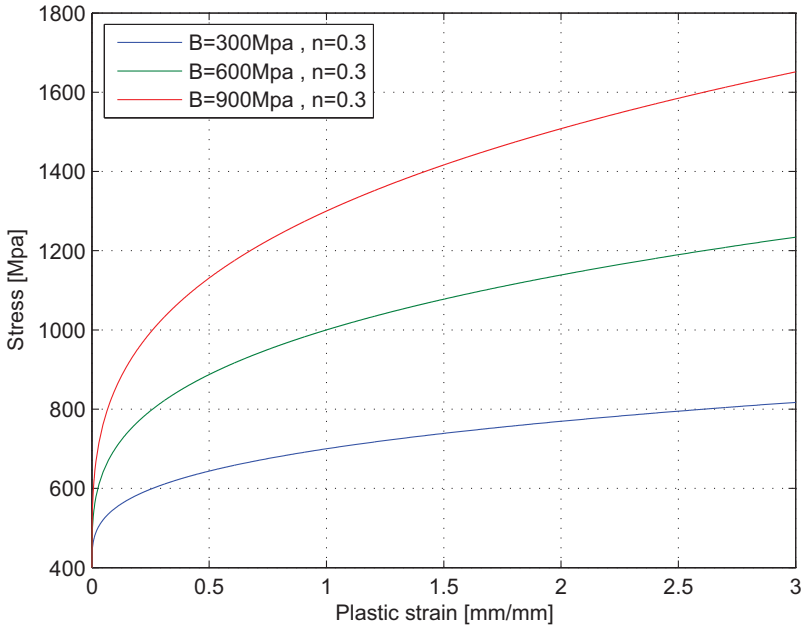

Figure 4.3: Flow stress vs plastic strain for $A + B(\epsilon_{pl})^n$ with $A = 400$ MPa

From Figure 4.4 it is clear that when B is held constant and the strain hardening index, n, is increased the slope of the stress-strain curve is increased. However, the value of

stress at a strain of 1 remains unchanged, with the consequence that stress below this value of strain is reduced, while stresses at strains higher than 1 are increased.

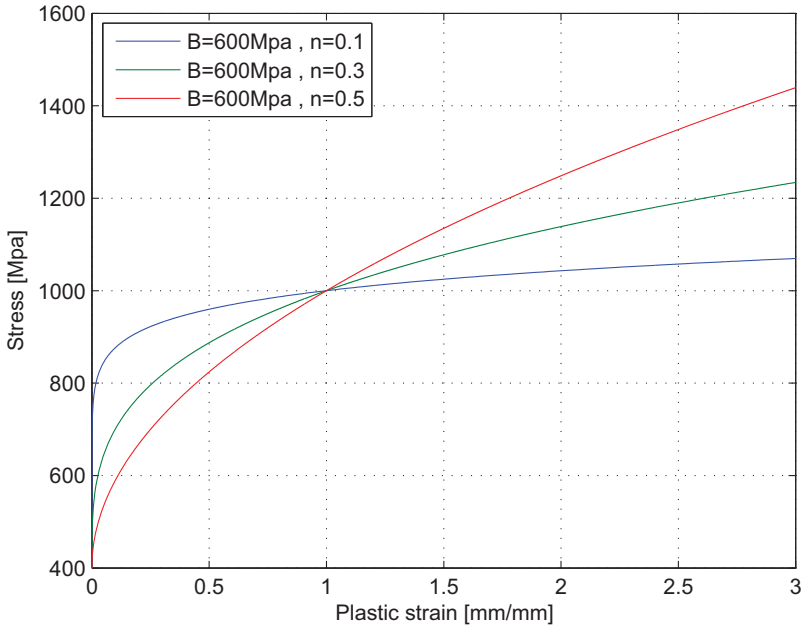

Figure 4.4: Flow stress vs plastic strain for $A + B(\epsilon_{pl})^n$ with $A = 400$ MPa

When $Clog(\dot{\epsilon}_{pl}/\dot{\epsilon}_{ref})$ is plotted against $\dot{\epsilon}_{pl}/\dot{\epsilon}_{ref}$ as in Figure 4.5, it can be seen that strain rate sensitivity is greatest when $\dot{\epsilon}_{pl}$ approaches $\dot{\epsilon}_{ref}$. Increasing the strain hardening index, C, results in both an increase in the magnitude of the strain rate multiplier and a higher gradient of the resulting curve so that strain rate sensitivity is increased.

The temperature component is sensitive to both m and t_{melt}. At higher temperatures, the temperature coefficient, T, tends to unity, which results in a decrease of the thermal multiplier, resulting in thermal softening of the material through a reduced flow stress magnitude. This is illustrated in Figure 4.6. It can also be seen that when m is less than one, the material shows strong thermal sensitivity, while higher values of of m indicate that strength is retained at higher operating temperatures.

Material failure modelling: Chip separation and segmental chip formation through crack growth

Chip separation has always been a matter of controversy among researchers on the experimental analysis of metal cutting [24]. The discussions are reflected by the numerical simulations where no clear direction is given as to which is the best approach. In literature, several methods are employed to model the chip separation process in which the chip is sheared from the parent material. Many models use a predetermined cutting line along which nodal separation or element failure can occur along a line which coincides with the path which the cutting tool tip makes as it is advanced [59] [48] [60] [6]. Nodal separation is achieved through the generation of new nodes or the

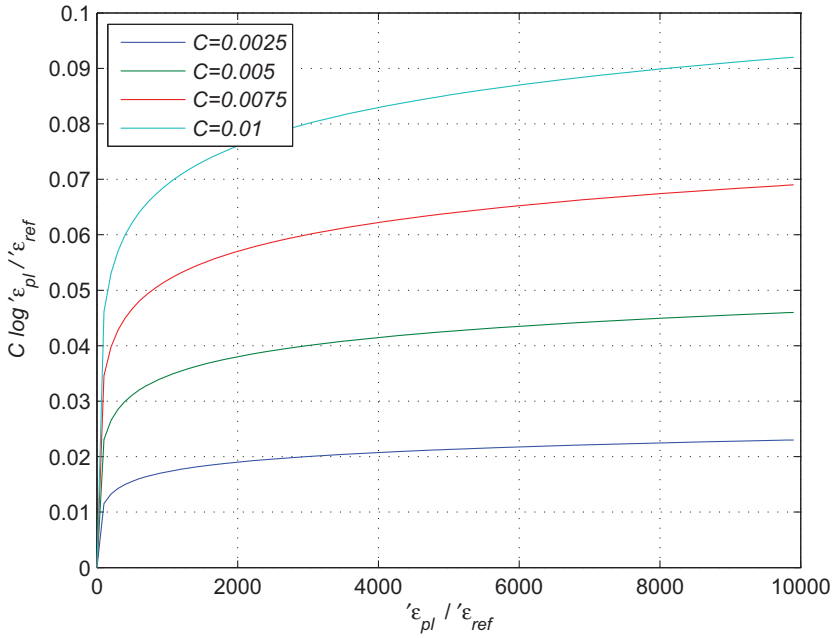

Figure 4.5: Strain rate sensitivity in J-C model

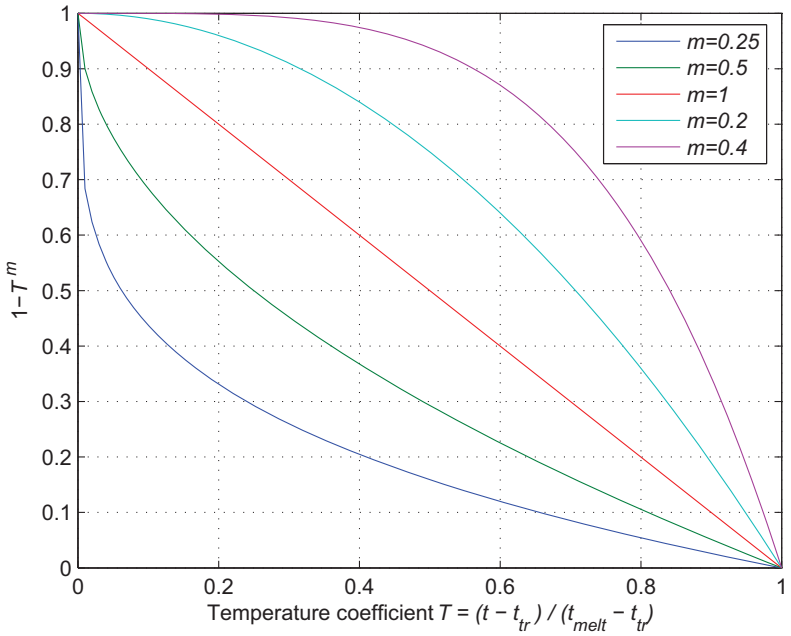

Figure 4.6: Temperature sensitivity in J-C model

removal of constraints placed on superimposed nodes when the separation criterion is met.

Chip separation criteria based on nodal separation which are used in literature are varied and range from nodal distance formulations (geometric) to physical criteria which make use of various critical indicators to determine failure and which are illustrated in Figure 4.7. Usui and Shirakashi [59] pioneered the discussion of chip separation by employing a separation criterion based on the distance between the tool tip and the nearest node along a pre-defined cutting path, as illustrated in Figure 4.7(a). The criterion is based on geometrical considerations and does not account for possible chip breakage outside the cutting line [59] [33] [48] [61] [62] [36]. In simulations using this strategy, as the tool advances, the distance between the node $F_{w,c}$ and the tool tip decreases and, at a critical distance, d_{cr}, either a new node is created or a restriction in superimposed nodes is removed, which makes it possible for the material to separate. Critical indicators have been based on equivalent plastic strain, total strain energy, maximum principle stress or ductile and brittle fracture concepts [24].

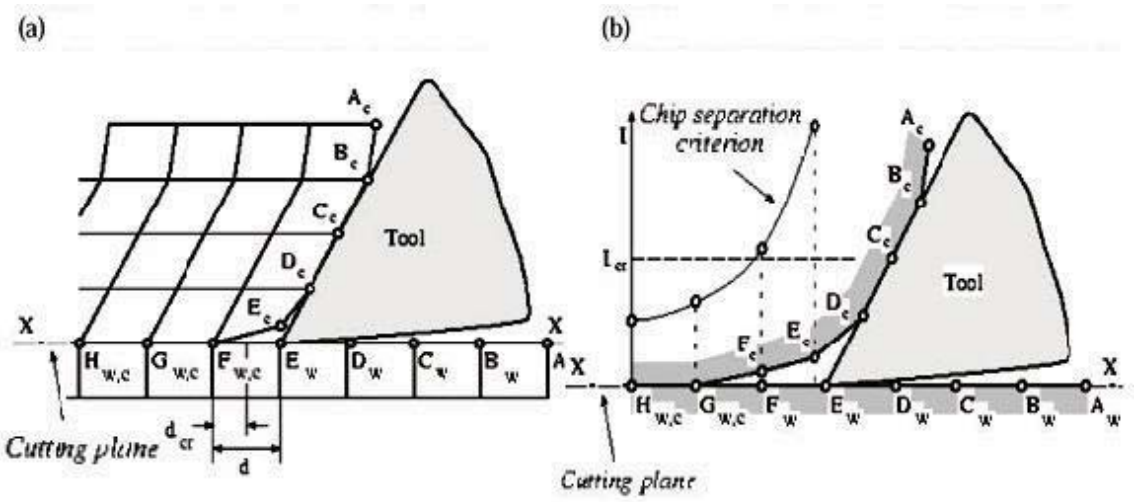

Figure 4.7: Chip separation along predetermined cutting line [24] (a) nodal distance criterion (b) critical indicator

Owen and Vaz Jr. [47], used a chip breakage criterion based on damage considerations in conjunction with an adaptive re-meshing scheme and element erosion. Chip separation is accomplished by multiple re-meshing procedures to model the crack growth around failed elements. This method does not rely on a pre-defined cutting line, and can thus model the effects of cutting edge radius on the simulation.

In this study chip separation is achieved through element failure and subsequent deletion in a row of elements which represent the cutting line. The elements in the cutting line are much smaller than the surrounding elements, and have little effect on the simulation. The method is the same used by Ng and Aspinwall [6]. Failure is determined according to the J-C shear fracture/failure criteria. The elements have a relatively insignificant height compared to the surrounding elements so that the effects of element deletion on the solution is minimised. Chip segmentation is also initiated through crack propagation by applying the J-C failure criteria to elements along the surface of

the chip being formed. Although simple, the model is rational and is an improvement over other fracture models based only on plastic strain or the current condition of other variables. Furthermore, from a computational viewpoint it is attractive since it requires little additional computational time and only one additional element array to store the accumulated damage [31].

The J-C fracture model is intended to show the relative effects of various parameters and attempts to account for path dependency by accumulating damage as the deformation proceeds. Unlike more complicated Nucleation and Growth (NAG) models [8], the model uses a limited number of constants and is primarily dependent on the strain, strain rate, temperature and pressure.

Abaqus/Explicit provides a dynamic failure model specifically for the Johnson-Cook plasticity model which is suitable for high-strain-rate deformation of metals. Abaqus/-Explicit also offers a general implementation of the Johnson-Cook failure model as part of the family of damage initiation criteria, which is the recommended technique for modelling progressive damage and failure of materials. Fracture in the J-C material model is derived from a cumulative damage law which is a function of mean stress, strain rate, and temperature. The damage to an element is defined by

$$E = \sum \frac{\Delta\epsilon}{\epsilon_f} \tag{4.9}$$

where

$$\epsilon_f = (d_1 + d_2 \exp(d_3(\frac{p}{q})))(1 + d_4 \ln(\frac{\dot{\epsilon}_p l}{\dot{\epsilon}_{ref}}))(1 + d_5 T) \tag{4.10}$$

and failure is assumed to occur when

$$E = 1 \tag{4.11}$$

Here $\Delta\epsilon$ in 4.9 is defined as the increment of effective plastic strain during an integration cycle and ϵ_f is the equivalent strain to fracture, under the current conditions of strain rate, temperature, pressure and equivalent stress. The Johnson-Cook dynamic failure model is based on the value of the equivalent plastic strain at element integration points and the summation is performed at each increment of the solution. Fracture is assumed to occur when $D = 1.0$. ϵ_f is calculated from 4.10 where p is the mean stress normalized by the effective stress q and the parameters d_1, d_2, d_3, d_4, and d_5 are constants determined from high strain, strain rate fracture tests. ϵ_f is assumed to be dependent on a non-dimensional plastic strain rate, a dimensionless pressure-deviatoric stress ratio, (where p is the pressure stress and q is the Von Mises stress) and the non-dimensional temperature, T, defined earlier in the Johnson-Cook hardening model.

Table 4.4: Johnson Cook failure coefficients [63]

d_1	d_2	d_3	d_4	d_5	$\dot{\epsilon}_{ref}$
-0.09	0.25	-0.5	0.014	3.87	1

As mentioned, the Johnson-Cook failure model is also used to model crack initiation

along the chip surface and growth into the chip resulting in segmented chip formation. The formation of surface cracks in segmental chip formation is well documented and along with thermal softening, brings about catastrophic adiabatic shearing in the material [57].

General contact in Abaqus allows the use of element-based surfaces to model surface erosion for analyses. If an interior surface is included in the general contact definition, the surface topology will evolve to match the exterior of elements that have not failed. The general contact algorithm modifies the list of contact faces and contact edges that are active in the contact domain based on the failure status of the underlying elements. General contact considers a face only if its underlying element has not failed and it is not coincident with a face from an adjacent element that has not failed; thus, exterior faces are initially active, and interior faces are initially inactive. Once an element fails, its faces are removed from the contact domain, and any interior faces that have been exposed are activated. A contact edge is removed when all the elements that contain the edge have failed. Based on this algorithm, the active contact domain evolves during the analysis as elements fail.

In Abaqus, when the failure criterion is met, the deviatoric stress components are set to zero and remain zero for the rest of the analysis. Depending on the user's choice, the pressure stress may also be set to zero for the rest of calculation, this option specifies that the element is removed from the analysis and results in element deletion. This results in an unrealistic, instantaneous degradation of the element stiffness which is not representative of ductile material failure in reality. This is confirmed in the observation in which a large crack opened ahead of the cutting tool when the model was run using published values of J-C failure constants for Ti6Al4V. Furthermore a sudden drop of the stress at the material point may lead to dynamic instabilities in the solution. It is therefore necessary to include a progressive damage and failure model in the FE model so that material response during failure can be more accurately modelled.

Abaqus offers a general capability for modelling damage evolution and failure in ductile metals and can be used in conjunction with the a number of plasticity models, including the Johnson-Cook type. The capability supports the specification of one or more damage initiation criteria, including ductile, shear, forming limit diagram and many others. After damage initiation, which occurs when $D = 1$ in (4.11), the material stiffness is degraded progressively, according to the specified damage evolution response. The progressive damage models allow for a smooth degradation of the material stiffness, which makes them suitable for both quasi-static and dynamic situations, a great advantage over the dynamic failure models.

To help in understanding of the failure modelling, consider the response of a typical metal specimen during a simple tensile test. The stress-strain response, such as that illustrated in Figure 4.8, will show distinct phases. The material response is initially linear elastic, $a - b$, followed by plastic yielding with strain hardening, $b - c$. Beyond point c there is a marked reduction of load-carrying capacity until rupture, $c - d$. The deformation during this last phase is localised in a neck region of the specimen. Point c identifies the material state at the onset of damage, which is referred to as the damage initiation criterion. Beyond this point, the stress-strain response $c - d$ is governed by the evolution of the degradation of the stiffness in the region of strain localisation. In the context of damage mechanics $c - d$ can be viewed as the degraded response of the curve $c - d'$ that the material would have followed in the absence of damage.

Figure 4.9 illustrates the characteristic stress-strain behavior of a ductile material un-

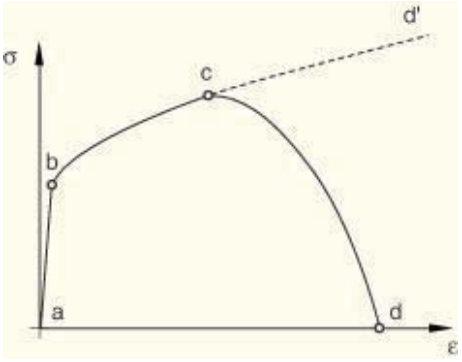

Figure 4.8: Progressive damage and failure model

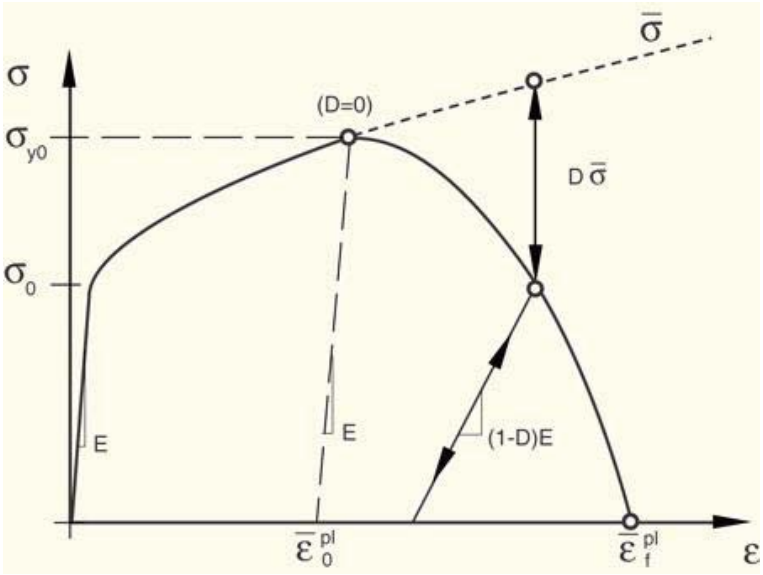

Figure 4.9: Stress-strain curve with progressive damage degradation

dergoing damage. In the context of an elastic-plastic material with isotropic hardening, the damage manifests itself in two forms: softening of the yield stress and degradation of the elasticity. The solid curve in the figure represents the damaged stress-strain response, while the dashed curve is the response in the absence of damage. As discussed later, the damaged response depends on the element dimensions such that mesh dependency of the results is minimised. σ_{y0} and ϵ_0^{pl} are the yield stress and equivalent plastic strain at the onset of damage. ϵ_f^{pl} is the equivalent plastic strain at failure, which occurs when the overall damage variable reaches unity, D=1.

The evolution of the damage variable with the relative plastic displacement can be specified in tabular, linear, or exponential form. In this study, a simple linear law is used. This predicts a linear evolution of the damage variable with effective plastic displacement, as shown in Figure 4.10. The value of the damage variable then increases linearly with u^{pl} according to

$$D = \frac{L\dot{\epsilon}^{pl}}{u^{pl}} = \frac{\dot{u^{pl}}}{u_f^{pl}} \tag{4.12}$$

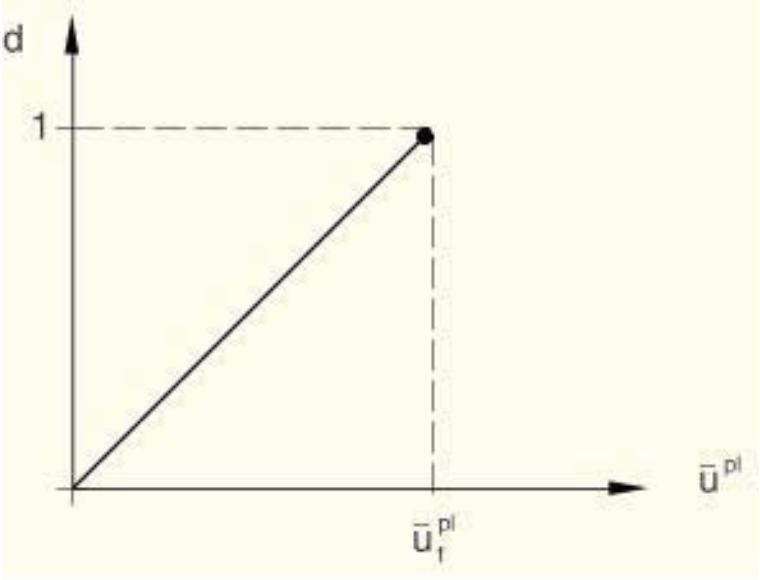

Figure 4.10: Progressive damage: linear progression

This definition ensures that when the effective plastic displacement reaches the value $u^{pl} = u_f^{pl}$, the material stiffness will be fully degraded. The linear damage evolution law defines a truly linear stress-strain softening response only if the effective response of the material is perfectly plastic (ie there is a constant yield stress) after damage initiation. The value of the equivalent plastic strain at failure depends on the characteristic length, L, of the element and cannot be used as a material parameter for the specification of the damage evolution law. Instead, the damage evolution law is specified in terms of equivalent plastic displacement, u^{pl}. These concepts are explained in the following paragraphs.

In continuum mechanics the constitutive model is normally expressed in terms of stress-strain relations. When the material exhibits strain-softening behaviour, leading to strain localisation, this formulation results in a strong mesh dependency of the finite element results, in that the energy dissipated decreases upon mesh refinement. In Abaqus, damage evolution models use a formulation intended to alleviate this mesh dependency. This is accomplished by introducing a characteristic length into the formulation, which in Abaqus is related to the element size, and by expressing the softening part of the constitutive law as a stress-displacement relation. In this case the energy dissipated during the damage process is specified per unit area, not per unit volume. This energy is treated as an additional material parameter, which is used to compute the displacement at which full material damage occurs. This is consistent with the concept of critical energy release rate as a material parameter for fracture mechanics. This formulation ensures that the correct amount of energy is dissipated and greatly alleviates the mesh dependency.

A different approach is required to follow the strain-softening branch of the stress-strain response curve. Hillerborg's fracture energy proposal is used to reduce mesh dependency by creating a stress-displacement response after damage is initiated [64]. Using brittle fracture concepts, Hillerborg defines the energy required to open a unit area of crack as a material parameter. With this approach, the softening response after damage initiation is characterised by a stress-displacement response rather than a

stress-strain response.

The implementation of this stress-displacement concept in a finite element model requires the definition of a characteristic length associated with an integration point. The definition of the characteristic length depends on the element geometry and formulation, for the elements used in this study, it is half the length of a line across an element for a second-order element. Therefore, elements with large aspect ratios will have rather different behaviour, depending on the direction in which they crack. Some mesh sensitivity thus remains due to this effect, and elements that have aspect ratios of unity are thus employed. The value of the critical length was determined by an iterative procedure with the criterion that no crack should open ahead of the cutting tool along the cutting line.

4.1.2 Thermal modelling

In a fully coupled thermo-mechanical analysis, a coupled temperature-displacement procedure is used to solve simultaneously for the stress/displacement and the temperature fields. In Abaqus/Explicit the heat transfer equations are integrated using an explicit forward-difference time integration rule given in 4.13, and the mechanical solution response is obtained using an explicit central-difference integration rule.

$$\theta^N_{(i+1)} = \theta^N_{(i)} + \Delta t_{(i+1)} \dot{\theta^N_{(i)}} \tag{4.13}$$

where $\theta^N_{(i)}$ is the temperature at node N and the subscript i refers to the increment number in an explicit dynamic step. The forward-difference integration is explicit in the sense that no equations need to be solved when a lumped capacitance matrix is used. The current temperatures are obtained using known values of $\dot{\theta^N_{(i)}}$ from the previous increment. The values of $\dot{\theta^N_{(i)}}$ are computed at the beginning of the increment by

$$\dot{\theta^N_{(i)}} = (C^{NJ})^{-1}(P^J_{(i)} - F^J_{(i)}) \tag{4.14}$$

where C^{NJ} is the lumped capacitance matrix, $P^J_{(i)}$ is the applied nodal source vector, and $F^J_{(i)}$ is the internal flux vector. Since both the forward-difference and central-difference integrations are explicit, the heat transfer and mechanical solutions are obtained simultaneously by an explicit coupling. Therefore, no iterations or tangent stiffness matrices are required.

For high rate deformation problems, it can be assumed that an arbitrary percentage of the plastic work done during deformation produces heat in the deforming material. This is referred to as the inelastic heat fraction which is typically used in the simulation of high-speed manufacturing processes involving large amounts of inelastic strain, where the heating of the material caused by its deformation significantly influences temperature-dependent material properties. The heat generated is treated as a volumetric heat flux source term in the heat balance equation. For many materials, 90-100 percent of the plastic work is dissipated as heat in the material. Thus, the temperature used in (4.13) can be derived from the increase in temperature according to the following expression

$$\Delta t = \frac{\alpha}{\rho c} \int \sigma(\epsilon) d\epsilon \tag{4.15}$$

where Δt is the temperature increase, α is the percentage of plastic work transformed to heat, c is the heat capacity and ρ is the density. In Abaqus, the default value of the inelastic heat fraction is 0.9, which is also the value used by many researchers [7][6][65][9].

The conductive heat transfer between the contact surfaces is assumed to be defined by

$$q = k(\theta_A - \theta_B) \tag{4.16}$$

where q is the heat flux per unit area crossing the interface from point A on one surface to point B on the other, and θ_A and θ_B are the temperatures of the points on the surfaces, and k is the gap conductance. Point A is a node on the slave surface; and point B is the location on the master surface contacting the slave node or, if the surfaces are not in contact, the location on the master surface with a surface normal that intersects the slave node.

In Abaqus, k may be defined as a function of temperature, distance, pressure etc.

$$k = k(\bar{\theta}, d, p, \bar{f}_\gamma, m) \tag{4.17}$$

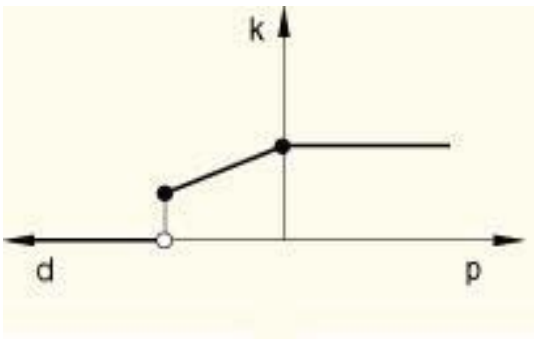

Figure 4.11: Gap conductance model

A table of data can be created, defining the dependence of k on the variables listed in 4.17. The default in Abaqus is to make k a function of the clearance d which is the method used in this study. When k is a function of gap clearance, d, the tabular data must start at zero clearance and define k as d increases. At least two pairs of points must be given to define k as a function of the clearance. The value of k drops to zero immediately after the last data point, so there is no heat conductance when the clearance is greater than the value corresponding to the last data point. If gap conductance is not also defined as a function of contact pressure, k will remain constant at the zero clearance value for all pressures, as shown in Figure 4.11.

Table 4.5: Thermal properties for Ti6Al4V and WC used in simulations [66]

Heat capacity ($x10^6 J/(m^3 K)$)	Conductivity ($W/(mK)$)
Ti6Al4V	
$2.35(0°C)$	$7(0.C)$
$2.52(200°C)$	$8.6(200°C)$
$2.76(400°C)$	$11.5(400°C)$
$3.5(600°C)$	$14.4(600°C)$
$3.9(800°C)$	$17.2(800°C)$
WC ISO P20	
$2.10(0°C)$	$24(0.C)$
$2.21(350°C)$	$26.7(350°C)$
$2.48(750°C)$	$27.2(750°C)$

4.1.3 Contact modelling and friction model

The Coulomb friction model relates the maximum allowable frictional or shear stress across an interface to the contact pressure between the contacting bodies. In the basic form of the Coulomb friction model, two contacting surfaces can carry shear stresses up to a certain magnitude across their interface before they start sliding relative to one another; this state is known as sticking. The Coulomb friction model defines this critical shear stress, τ, at which sliding of the surfaces starts, as a fraction of the contact pressure, p, between the surfaces [65][9][6]. The stick/slip calculations determine when a point transitions from sticking to slipping or from slipping to sticking and the fraction, μ, is known as the coefficient of friction.

$$\tau = \mu p \qquad \text{when} \qquad \tau < \bar{\tau}_{max} \tag{4.18}$$

$$\tau = \bar{\tau}_{max} \qquad \text{when} \qquad \tau > \bar{\tau}_{max} \tag{4.19}$$

where $\bar{\tau}_{max}$ can be defined as

$$\bar{\tau}_{max} = \sigma_y/\sqrt{3} \tag{4.20}$$

Here σ_y is defined as the uni-axial yield stress of the work material [65]. The formulation indicates that the friction is sliding when the friction stress is below $\bar{\tau}_{max}$, and it becomes sticking when the friction stress is equal to or larger than the $\bar{\tau}_{max}$ regardless of the contact normal stress. Sticking and sliding friction conditions along the tool/chip interface are dependent on the direct stress magnitude. Sticking will occur at high contact pressure and when the contact pressure is low, as is the case away from the tool cutting edge, sliding friction will dominate [9].

There are many variations on the value of friction coefficient which are used in literature. Köenig et al. suggest a constant friction coefficient of $\mu = 0.3$ [67], while others use a variable friction coefficient calculated from orthogonal cutting tests according to 4.21 [65].

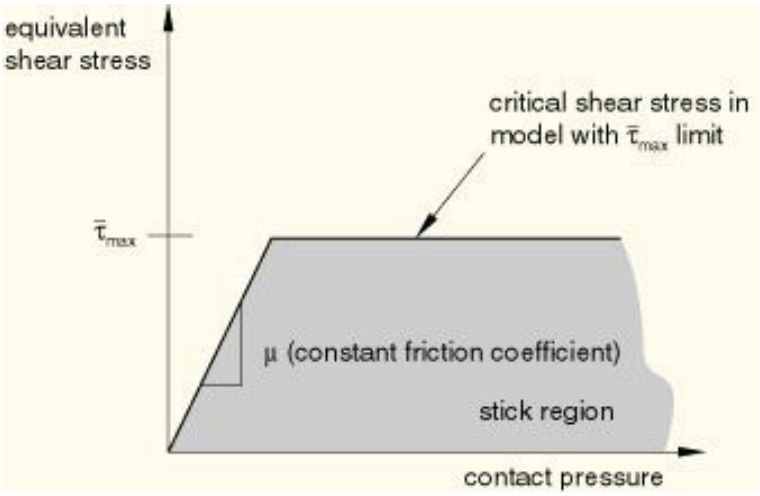

Figure 4.12: Stick-slip region for Coulomb friction [7]

$$\mu = \frac{F_x + F_y \tan\alpha}{F_y - F_x \tan\alpha} \tag{4.21}$$

In a study of FE modelling of titanium machining, Chen et. al. formulated an expression for μ from orthogonal cutting data, although the method used was not stated. The workpiece material in question was Ti6Al4V at 35ś2 HRC and regression analysis was used to determine the relation between the coefficient of friction with cutting speed U, feed f, and depth of cut d [9].

$$\mu = e^{-2.04077} \times 3.3U^{-0.474} \times 0.04f^{-0.043} \times 0.04d^{-0.4034} \tag{4.22}$$

The values of μ obtained in this study correspond well with values used by other researchers which generally range from 0.1 to 0.5 [7]. In this study, the friction coefficient was calculated according to Merchant's machining theory from 4.21, using the data from the orthogonal cutting tests, and is found to be primarily dependent on the feed, with cutting speed having little effect. This is due to the lack of influence of cutting speed on the cutting forces. Figure 4.13 shows the values of μ obtained for a cutting speed of 75 m/min as a function of feed and these values were used in all FE simulations unless otherwise stated. For comparison, the results of 4.22 are plotted for the same conditions.

In Abaqus, when employing a fully coupled temperature-displacement analysis, all dissipated frictional energy is converted into heat and distributed equally between the two surfaces by default. This behaviour can be modified in terms of the fraction of frictional energy, η, which is converted into heat, as well as the distribution of heat between the contacting surfaces, which is controlled by the variable f. $f = 1.0$ indicates that all of the generated heat flows into the slave surface of the contact pair while a value of $f = 0$ indicates that all of the generated heat flows into the master surface. The Abaqus manual and Ng et al. [7] suggest that it is reasonable to assume the default value of $f = 0.5$ because this value evenly distributes the generated heat between the two surfaces.

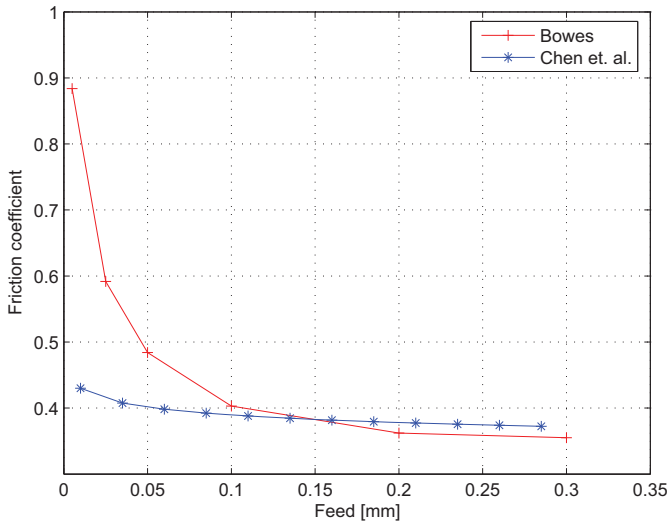

Figure 4.13: Friction coefficient vs. feed for cutting speed $75m/min$ calculated from orthogonal turning data

Chapter 5

Finite element model implementation and results

The dynamic explicit cutting model was implemented as described in the previous sections and a custom Matlab^{TM} pre-processor was developed for this study to generate the input file for the ABAQUS/Explicit^{TM} solver. The pre-processor is designed to provide a simple means of controlling all the parameters of the model including workpiece and tool geometry and mesh densities, as well as all material parameters such as flow stress properties, fracture criteria, thermal properties and friction properties. The pre-processor includes a visual interface for viewing the model geometry and the mesh that is generated. The source code is included in the appendix C. Figure 5.1 illustrates a simple mesh generated using the pre-processor. The tool is shown with red elements, the uncut chip in light blue and the parent material in dark blue. The chip is meshed with pre-distorted elements in anticipation of high shear deformations.

The tool is modelled so that it resembles the insert used in turning tests. The tool model has a flat rake face and a 7° rake angle. As is typical with FE models utilising a predefined cutting line, the tool is modelled with an infinitely sharp edge and is meshed as an elastic part with ABAQUS' C3D8RT elements, as is the workpiece. These are 8-node thermally coupled brick elements with reduced integration and hourglass control. The model employs 3D elements due to the ease with which contact on eroding surfaces can be handled. This is explained in further detail in section 4.1.1 and a plane strain boundary condition is enforced on the front and back surfaces of the workpiece and cutting tool.

The model makes use of mass scaling to increase the explicit time step so that simulation time is reduced, however, due to the pitfalls associated with this technique only moderate values of mass scaling are used. For a 2mm cut length at a cutting speed of 40m/min the simulation time on a 2Ghz machine is about 8 hours when one processor is employed. When conduction between the chip and tool is included the computational time becomes high and is implemented only in selected cases.

The model is not able to predict ploughing forces associated with machining when there is a finite radius on the cutting edge, thus, as described in section 3.2.3, the cutting forces can be separated into forces due to shearing the material, $F_{Pc}$and F_{Qc} and those due to plouging and rubbing. These forces are known as the cutting edge, F_{Pe}, and feed edge, F_{Qe}, forces. The edge forces do not vary significantly with increasing cut thickness and can thus be found by extrapolating edge force data to zero cut thickness. This is

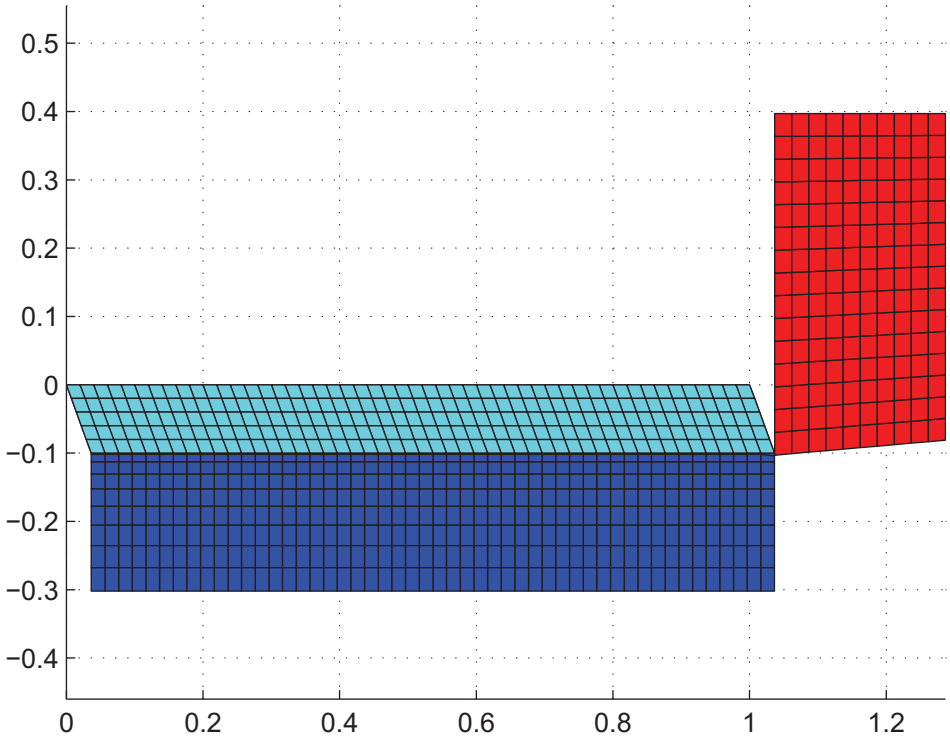

Figure 5.1: Sample plot of geometry and generated by matlab input file builder

consistent with the method used in the milling model in Chapter 6, which is described in greater detail in section 6.2. Experimentally obtained edge forces are thus added to the finite element force prediction to account for the model's inability to predict these forces.

$$\begin{aligned} F_{Pt} &= F_{Pe} + F_{Pc} \\ F_{Qt} &= F_{Qe} + F_{Qc} \end{aligned} \tag{5.1}$$

5.2 shows the process by which segmental chips are formed. In 5.2a, the surface of the material begins to bulge and the beginnings of the shear zone is observed. In 5.2b, the shear band is well defined and the bulge of the surface becomes greater and the geometry of the segment being formed is now fairly well defined. In image c, the surface of the material fractures as elements in the region fail according to the J-C failure criterion. Local plastic deformation results in high temperatures in the shearing zone and the material softens according to the J-C material model. Due to the low thermal conductivity of the material, heat is confined in the narrow shear band and large scale adiabatic shearing is observed in 5.2d-f as the chip segment is advanced to the point where the next segment begins to form (5.2f). High temperatures are observed, both in the shear zone and along the chip underside, due to high plastic strains in these regions

Figure 5.3 compares the chip shapes of the FE prediction (5.3a) and an experiment chip (5.3b). The chips show a striking resemblance and the model predicts the general shape well. The model, however, does not capture the inconsistent segment size which is

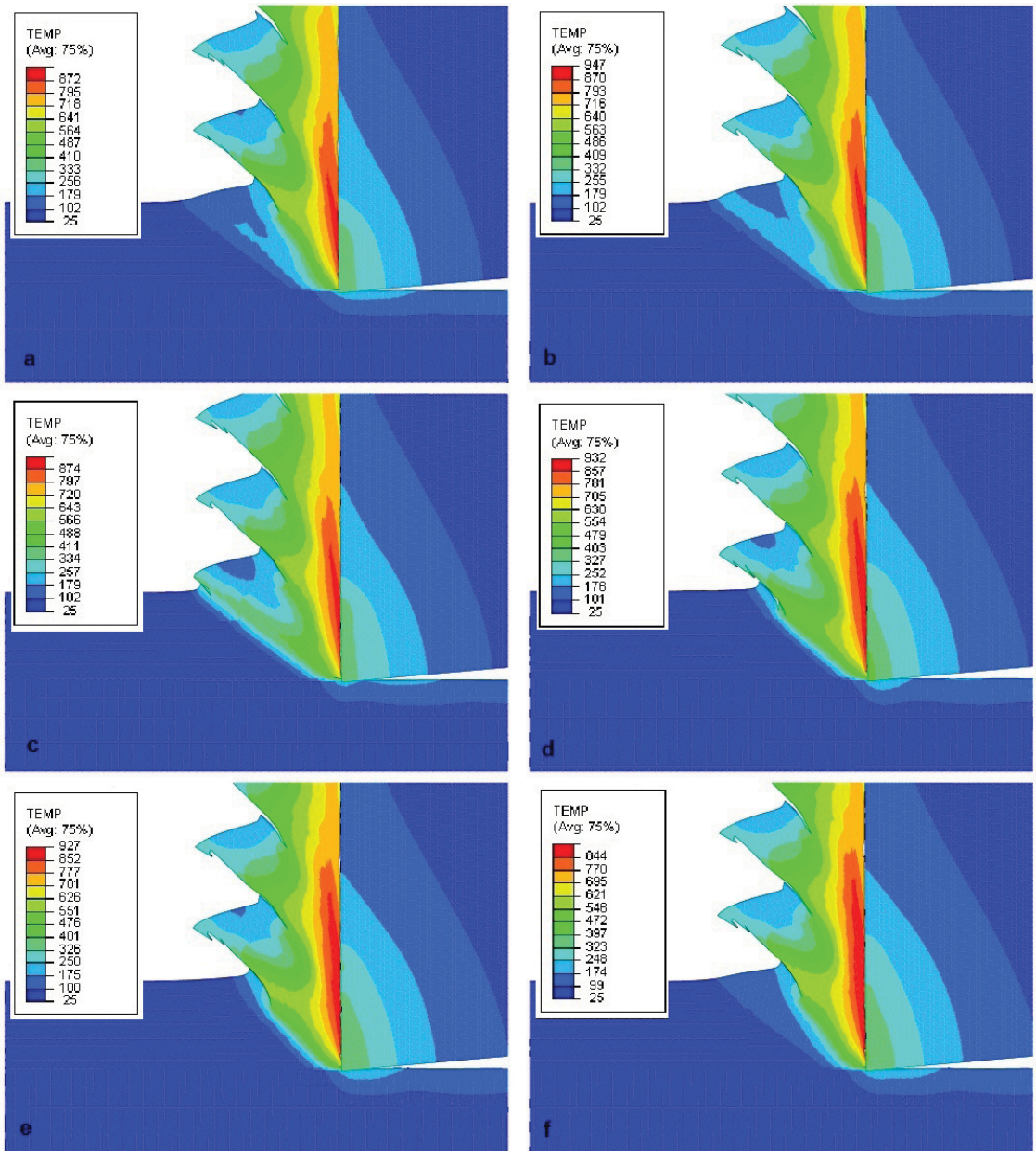

Figure 5.2: FE prediction of adiabatically sheared chip formation in titanium machining

observed in the experimental work. This may be attributed to vibrations and machine deflection during machining and even changes in microstructure.

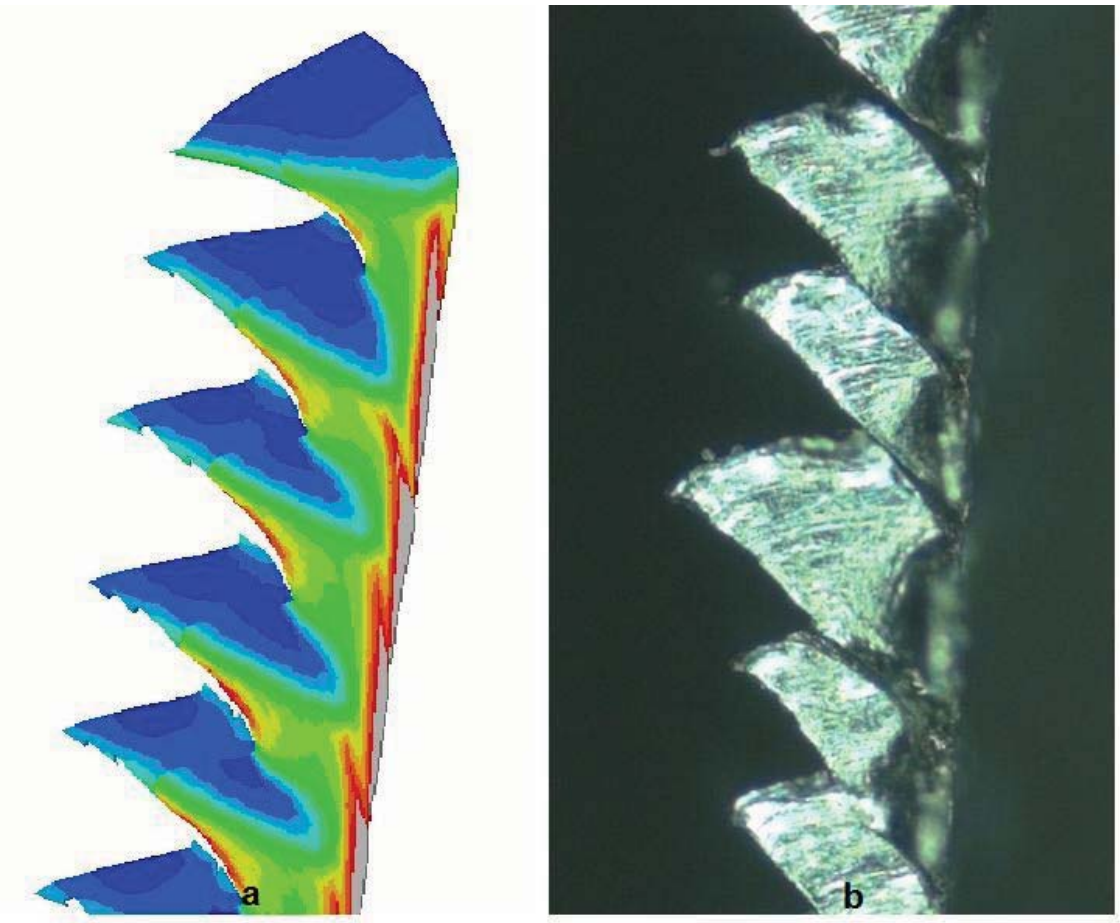

Figure 5.3: Comparison of chip geometries from turning tests and FE prediction $v = 75$ m/min $feed = 0.3$ mm

5.0.4 Mesh dependency

In order to investigate the mesh dependency of the model, results were generated for increasing mesh densities. Energy checks were conducted and the cutting forces extracted to determine when a sufficiently converged solution was reached. Cubic elements were used, with an element count of 4, 8, 12, 16 and 20 elements in the vertical direction of the uncut chip. The underlying material is meshed with the same density. Figure 5.4 shows the results of the mesh dependency in terms of cutting forces. It can be seen from the force plots that segmented chip formation, and the associated fluctuating forces are only well predicted when 16 or 20 elements are used. Some noise is observed in the force plots, which is due to acoustic waves traveling in the machined material and vibrations which are set up in the elastic cutting tool. This is also due to element failure and deletion along the cutting line, but this contribution is small, due to the use of damage progression criteria detailed in section 4.1.1, which enables smooth degradation of element stiffness.

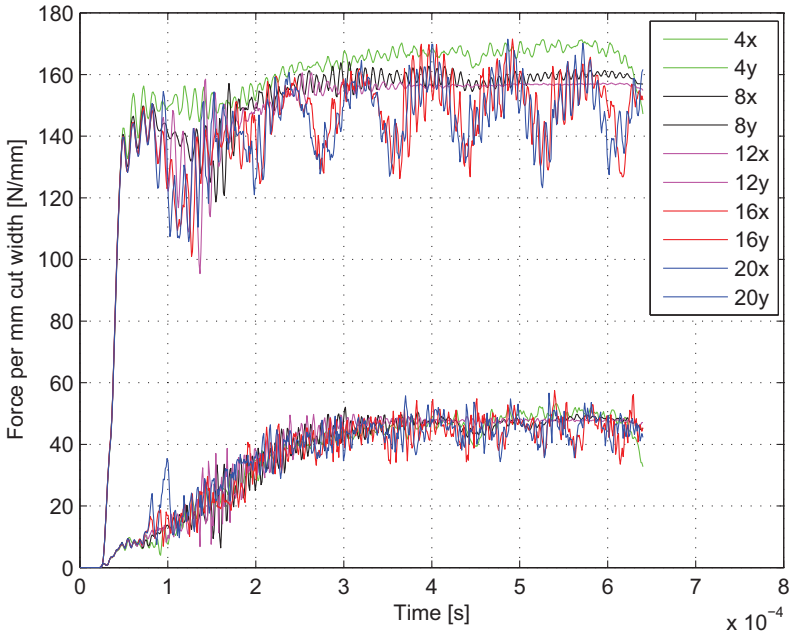

Figure 5.4: Cutting and feed forces with mesh refinement

In figure 5.5, the average of each of the forces is plotted and for the purpose of this study it is assumed that the solution is sufficiently well converged when 20 elements are used in the vertical direction of the chip. Feed forces, F_y, are not highly dependent on the mesh density. However cutting forces, F_x, are more strongly influenced by the mesh size and number of elements. For the remainder of this study the model is meshed with 20 elements in the vertical direction, the cutting length is fixed at $2mm$ and meshed with brick elements of equal aspect ratio. The underlying or parent material is meshed with 15 elements with decreasing element size from the bottom of the material toward the uncut chip.

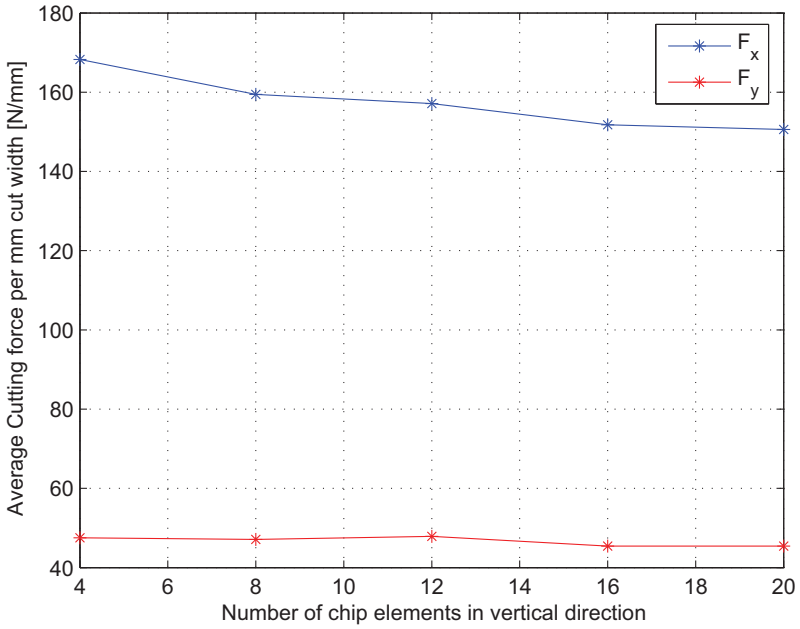

Figure 5.5: Comparison of average cutting and feed forces with mesh refinement

5.0.5 Cutting force prediction

In this section finite element predictions of cutting forces are compared with experimentally determined cutting forces for orthogonal machining as described in section 3.2.

Figure 5.7 shows the plastic strain for cut thicknesses of 0.025; 0.05; 0.1; 0.2 and 0.3 mm. Lower feeds result in a shorter, thicker chips. The magnitude of the plastic strain in the chip increases with increasing depth of cut and the shear angle increases. This is inconsistent with experimental findings where the, r_t, the chip thickness ratio(the ratio of uncut to cut chip thickness ratio) does not vary significantly. Table 5.1 compares the FE predictions of r_t with experimental findings. Contour plots of the FE predictions for temperature, Von Mises and Tresca stress are included in appendix B.

Table 5.1: Chip thickness ratio

Feed	0.025	0.05	0.1	0.2	0.3
r_t Experiment	0.59686	0.67344	0.56829	0.55556	0.52692
r_t FEM	0.571	0.613	0.625	0.645	0.653

Figure 5.9 shows the cutting force prediction compared with the average force data determined experimentally. In this case the friction coefficient is set at 0.3 and then later the experimentally determined coefficients are employed. Forces are predicted with good accuracy, especially at lower depths of cut. At high feeds the error for both the cutting and feed forces becomes large. The model over-predicts the machining forces under these conditions.

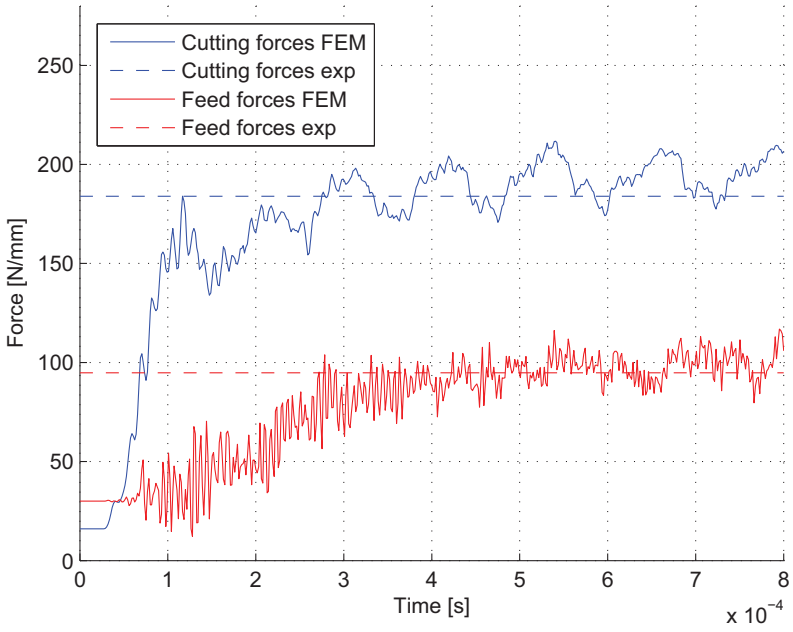

Figure 5.6: Comparison of cutting and feed forces for $feed = 0.1$ mm $v = 125$ m/min, experimental values are averaged

Figure 5.10 shows the results when experimentally determined friction coefficients are used. The feed forces at greater depths of cut are better predicted but the error at lower feeds is increased. Experimentally determined friction coefficients are used in the remainder of the study.

In figure 5.12, the cutting forces are plotted as a function of cutting speed and compared with experimental data for a feed of $0.1mm$. The forces are again predicted with reasonable accuracy. Results are plotted for zero and five degree rake in figures 5.12, 5.13 and 5.14, . Cutting forces are not highly dependent on cutting speed, as the effects of strain rate hardening at increasing cutting speed is offset by the thermal softening behaviour of the material

The FE model differs in that the increasing rake angles result in lower cutting and feed forces. Figure 5.17 shows the FE prediction, while Figure 5.16 plots the test data. Experimental data shows little sensitivity to rake angle. This may be due to the tool edge radius and material spring back on the insert rack face.

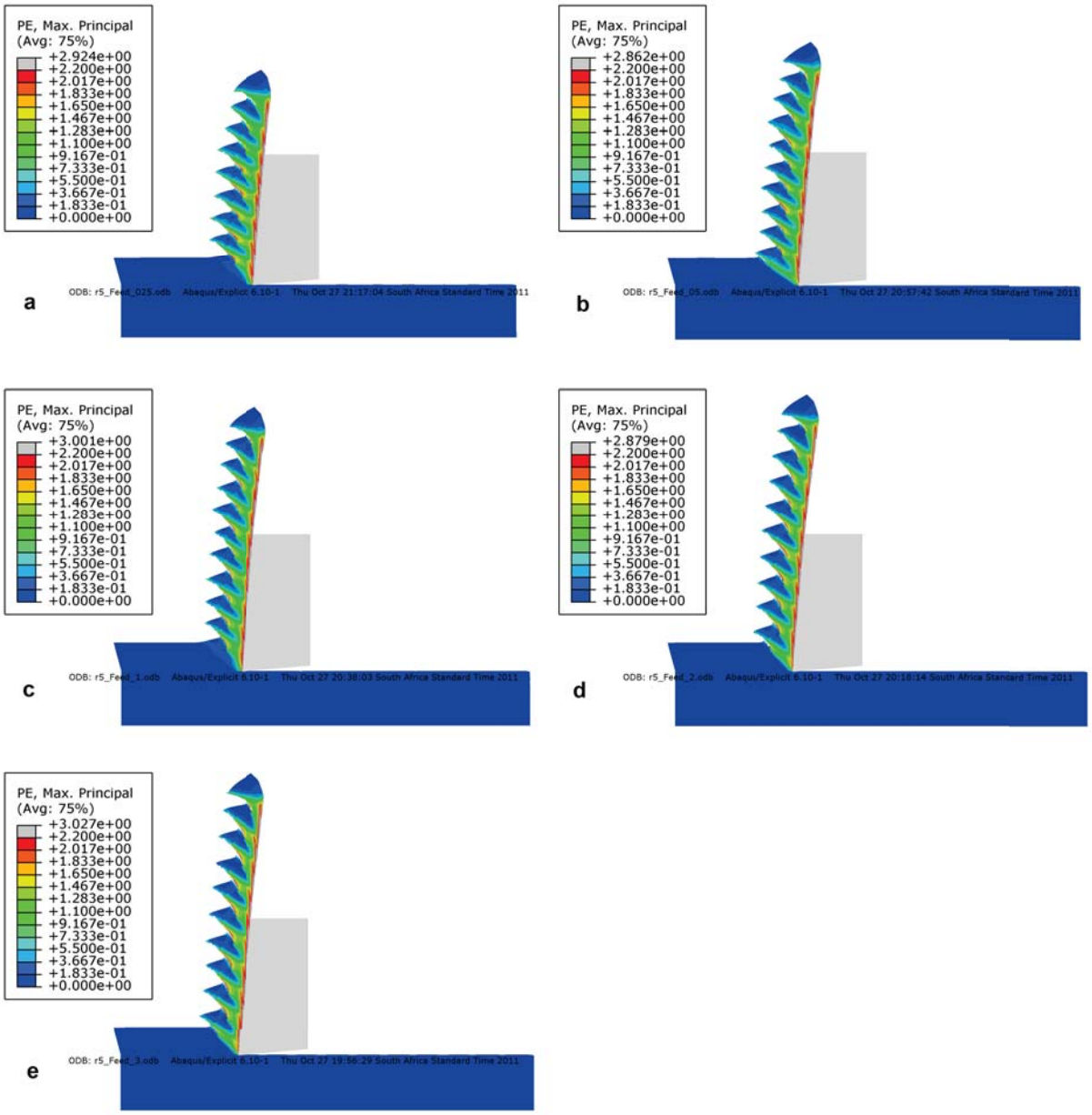

Figure 5.7: Max plastic strain prediction with $v = 75$ m/min and $feed = 0.025; 0.5; 0.1; 0.2; 0.3$ mm (image a-e)

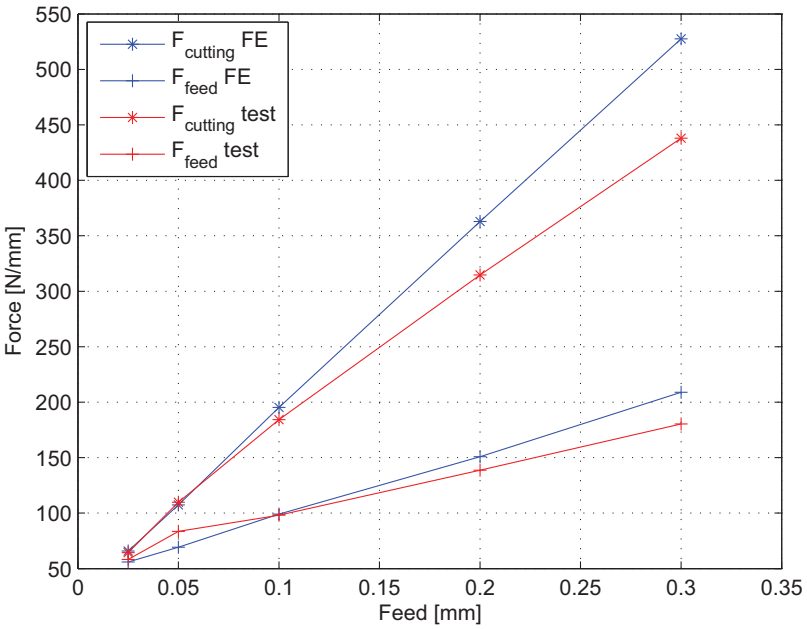

Figure 5.8: Comparison of cutting and feed forces with test data for $feed = 0.1 : 0.3$ mm, $v = 75$ m/min and $\mu = 0.3$

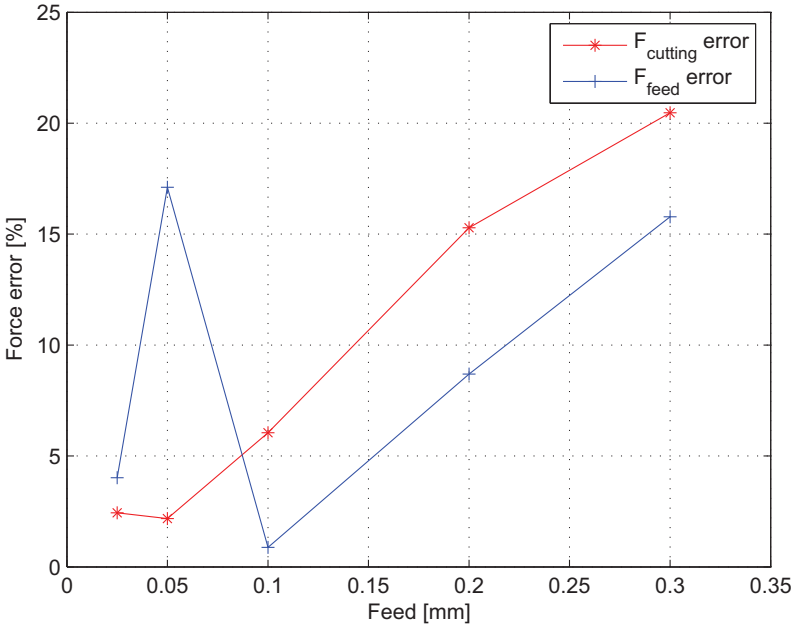

Figure 5.9: Error in cutting and feed forces in comparison test data for $feed = 0.1 : 0.3$ mm, $v = 75$ m/min and $\mu = 0.3$

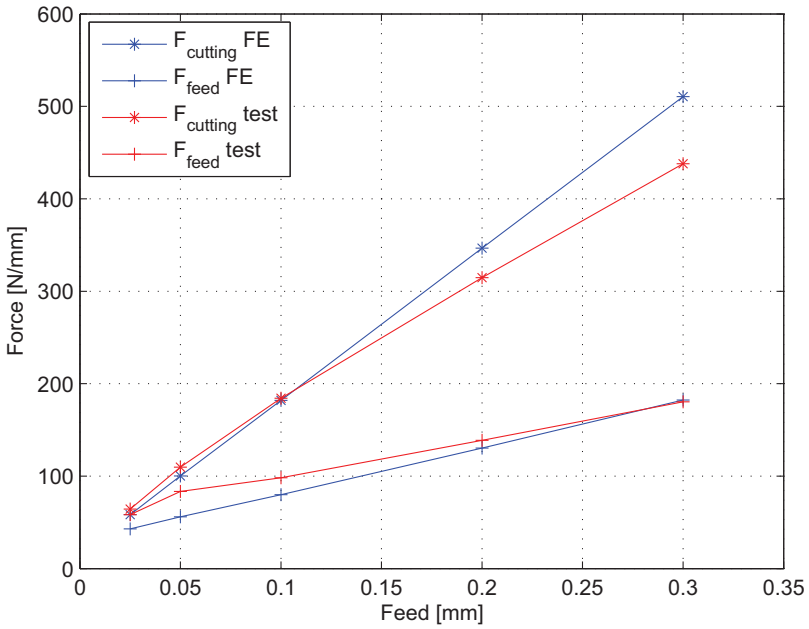

Figure 5.10: Comparison of cutting and feed forces with test data for $feed = 0.1 : 0.3$ mm, $v = 75$ m/min with μ calculated from test data

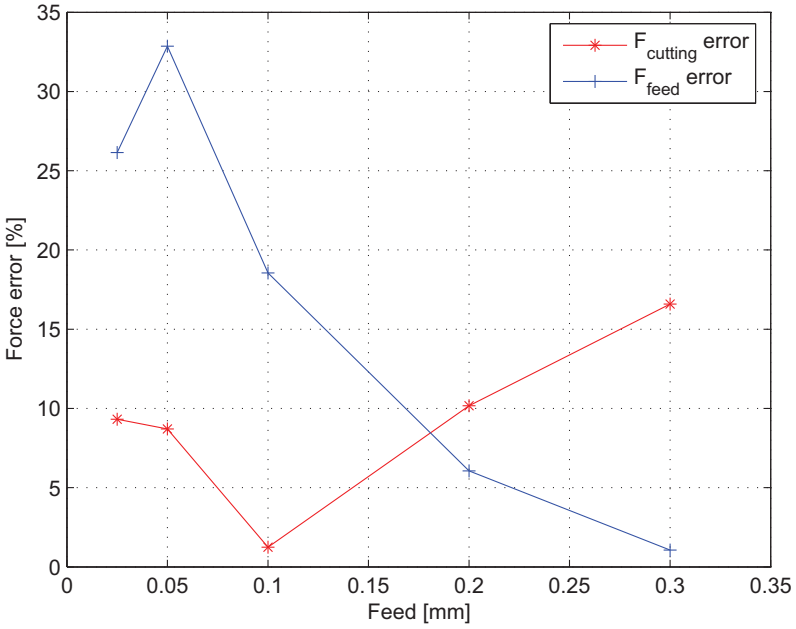

Figure 5.11: Error in cutting and feed forces when compared to test data for $feed = 0.1 : 0.3$ mm, $v = 75$ m/min with μ calculated from test data

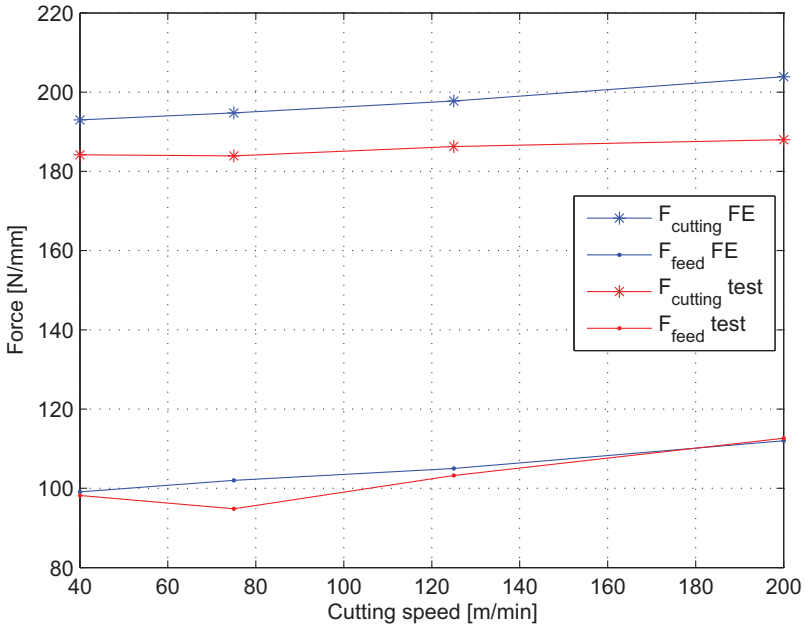

Figure 5.12: Cutting forces with increasing cutting speed $feed = 1$, $rake = 0$

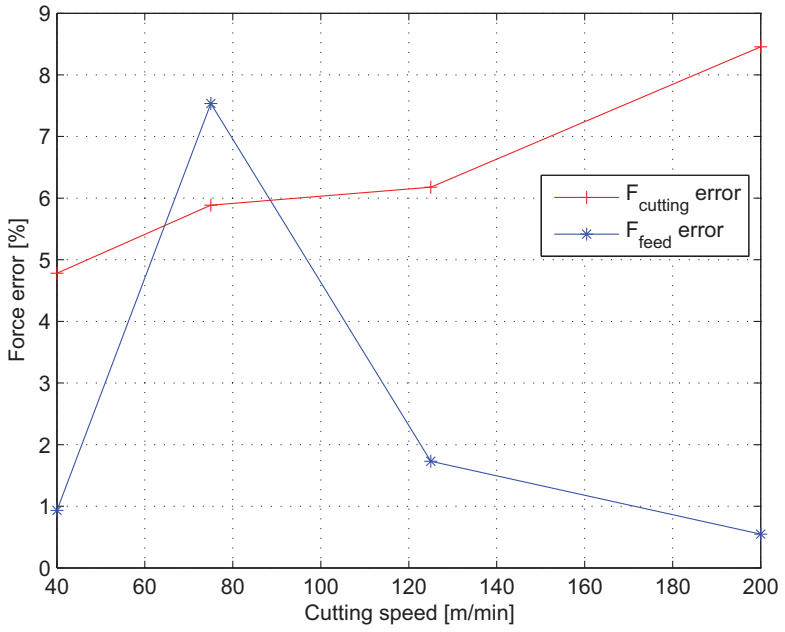

Figure 5.13: Error in cutting forces with increasing cutting speed $feed = 1$, $rake = 0$

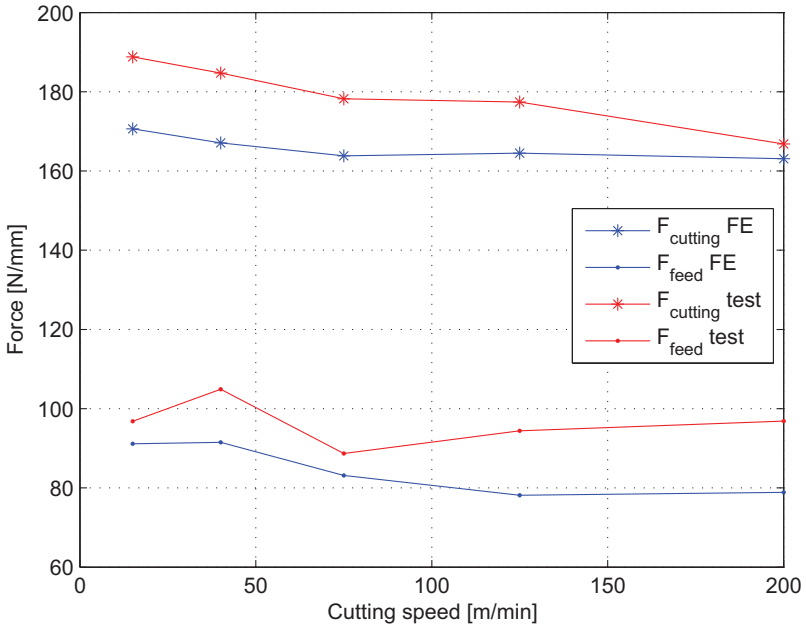

Figure 5.14: Cutting forces with increasing cutting speed: FE versus test ($feed = 1$ $rake = 5$)

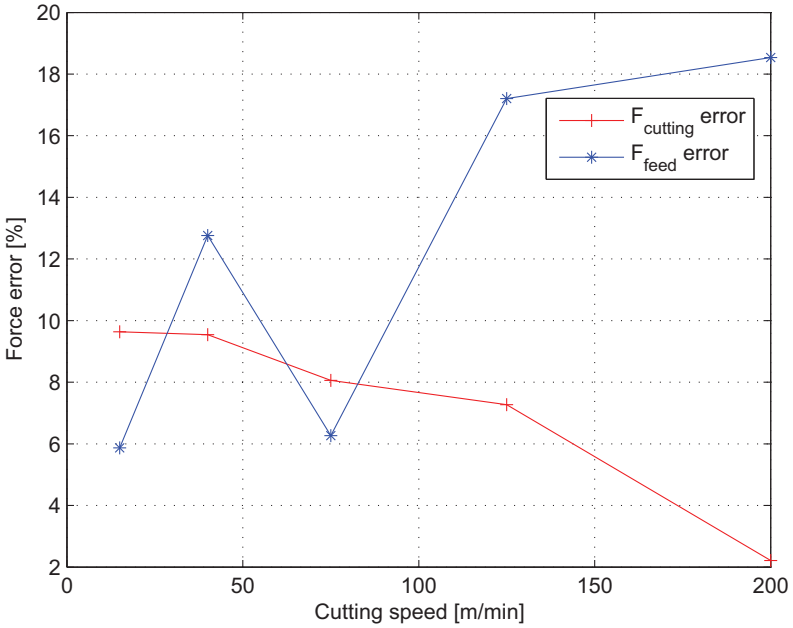

Figure 5.15: Error in cutting forces with increasing cutting speed: FE versus test ($feed = 1$ $rake = 5$)

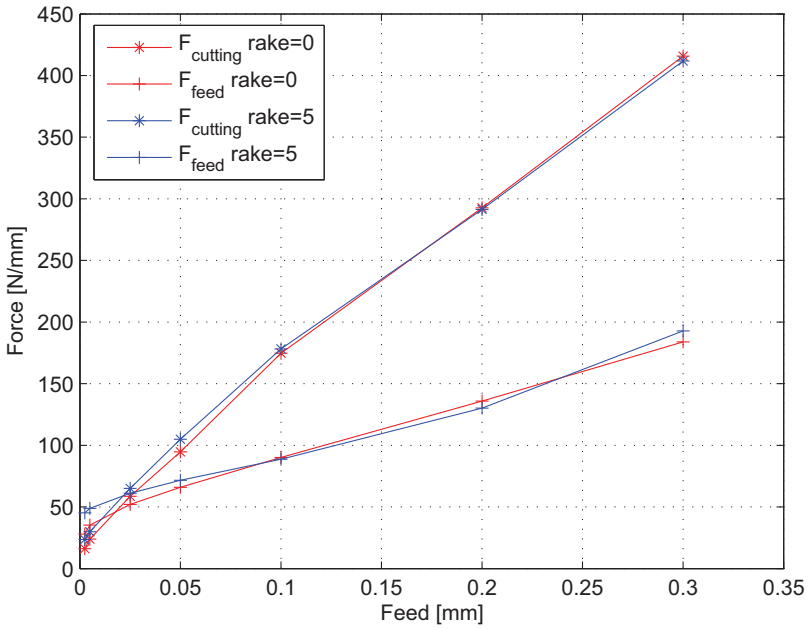

Figure 5.16: Cutting forces for different rake angles experimentally determined ($velocity = 75$ m/min $feed = 0.1$ mm)

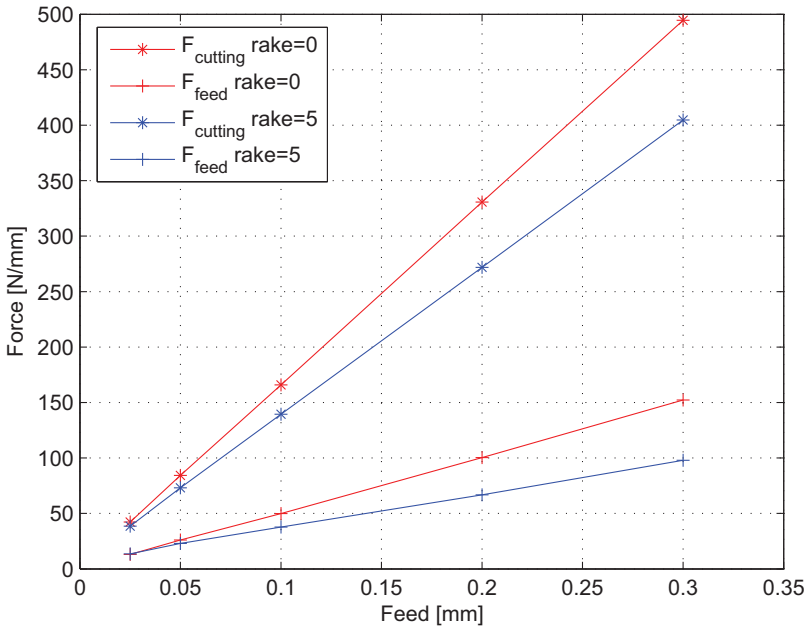

Figure 5.17: Cutting forces for different rake angles finite element prediction ($velocity = 75$ m/min $feed = 0.1$ mm)

5.0.6 Machining temperature

In this section the FE temperature prediction is compared with the experimental data. The sequence of images in Figure 5.18a-d shows the generation of heat through plastic deformation and frictional effects during machining. It can be seen that the highest temperatures occur on the chip back, near the cutting edge. This is due to shearing and flattening of the chip in this region, combined with the frictional heat generation. High temperatures in this region contribute greatly to tool wear and failure.

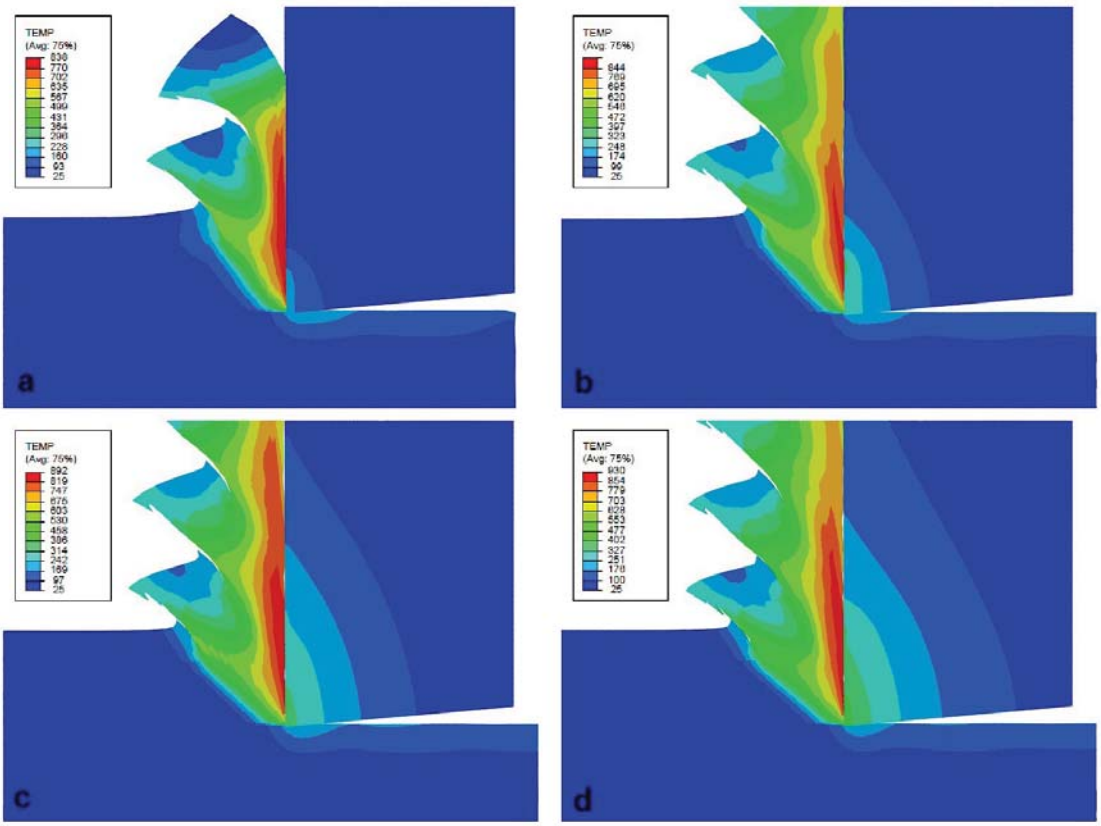

Figure 5.18: Temperature distribution in the chip and cutting tool $v = 75m/min\ feed = 0.1mm$

Figures 5.19 and 5.20 show the temperature contour plot for increasing cutting speed (15, 40, 75, 125, 200 and 300 m/min). Figure 5.19 plots the temperatures on the same scale, while in Figure 5.20, the temperatures are plotted to a scale that ranges from 25°C to the maximum temperature observed in each model. Contour plots of the maximum principle, Von Mises and Tresca stress are included in appendix B for reference.

Increased cutting speeds results in increased chip temperatures. At low speeds heat conduction in the titanium plays a greater role and a more homogeneous temperature distribution is observed as heat flows from areas of high plastic strain to cooler regions. Lower temperatures are also generated because the shear zone becomes broader at lower cutting speeds as can be seen in figure 5.21 which plots the plastic strain distribution in the chip. This occurs as the shear banding becomes a more adiabatic process as machining speed is increased and thermal softening occurs over a narrower region.

Figure 5.22 shows the measured chip underside temperatures, 0.8 mm from the cutting edge. The finite element prediction is plotted for comparison, calculated at the same

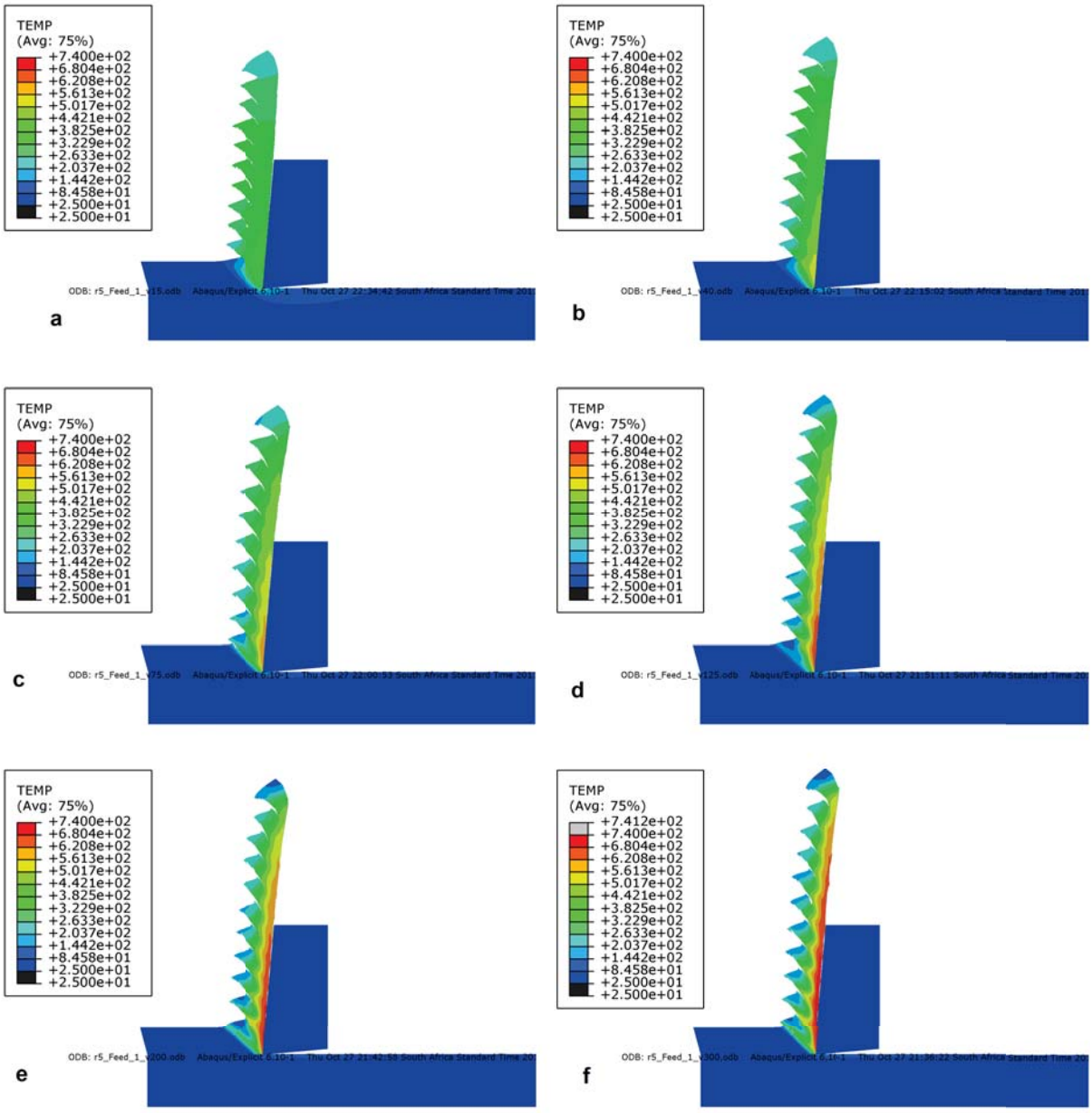

Figure 5.19: FE prediction of temperature distribution in the chip with $feed = 0.025$ mm/rev and $v = 15; 45; 75; 125; 200; 300$ m/min (image a-f)(equal legend scaling)

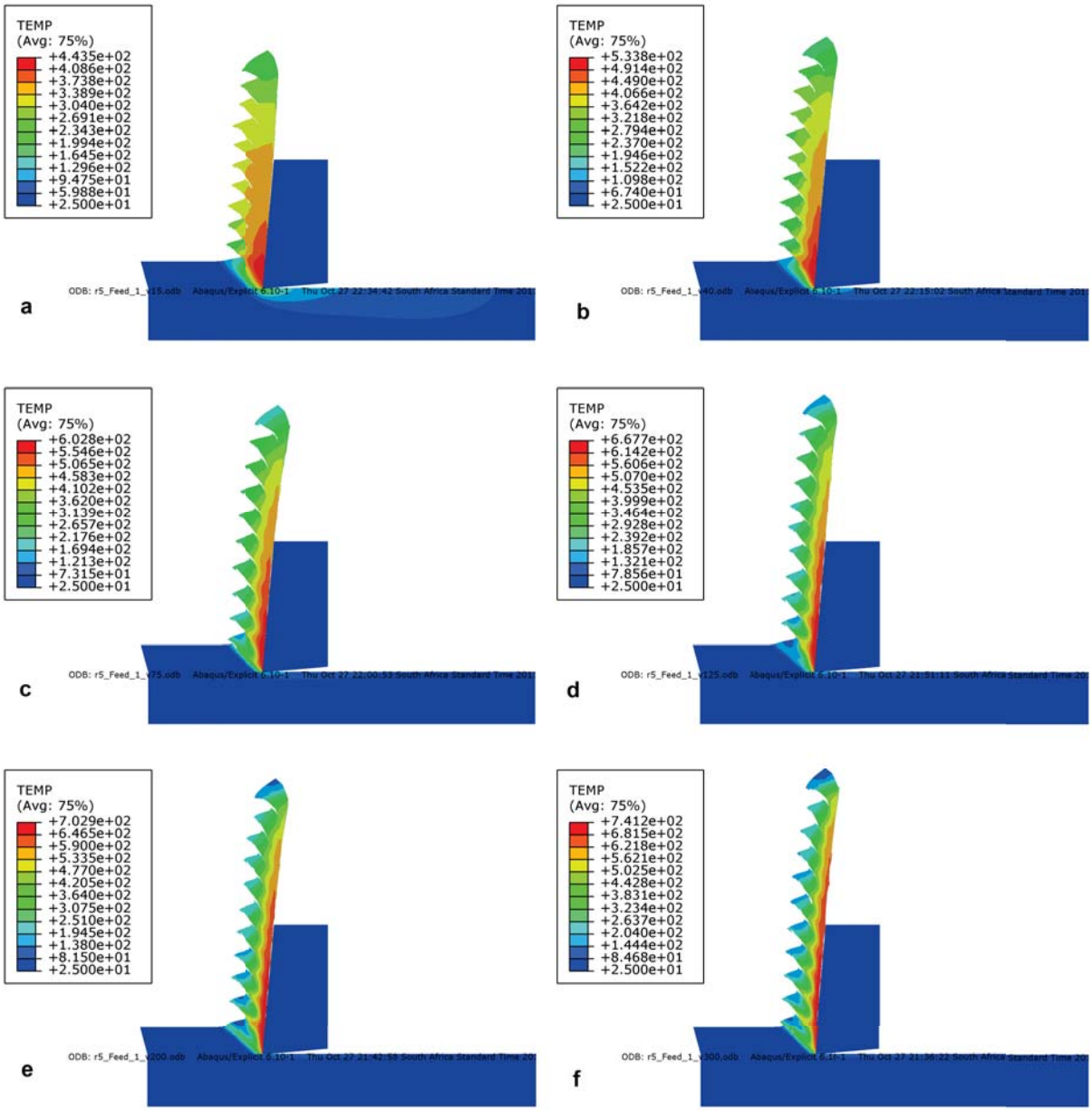

Figure 5.20: FE prediction of temperature distribution in the chip with $feed = 0.025$ mm/rev and $v = 15; 45; 75; 125; 200; 300$ m/min (image a-f)

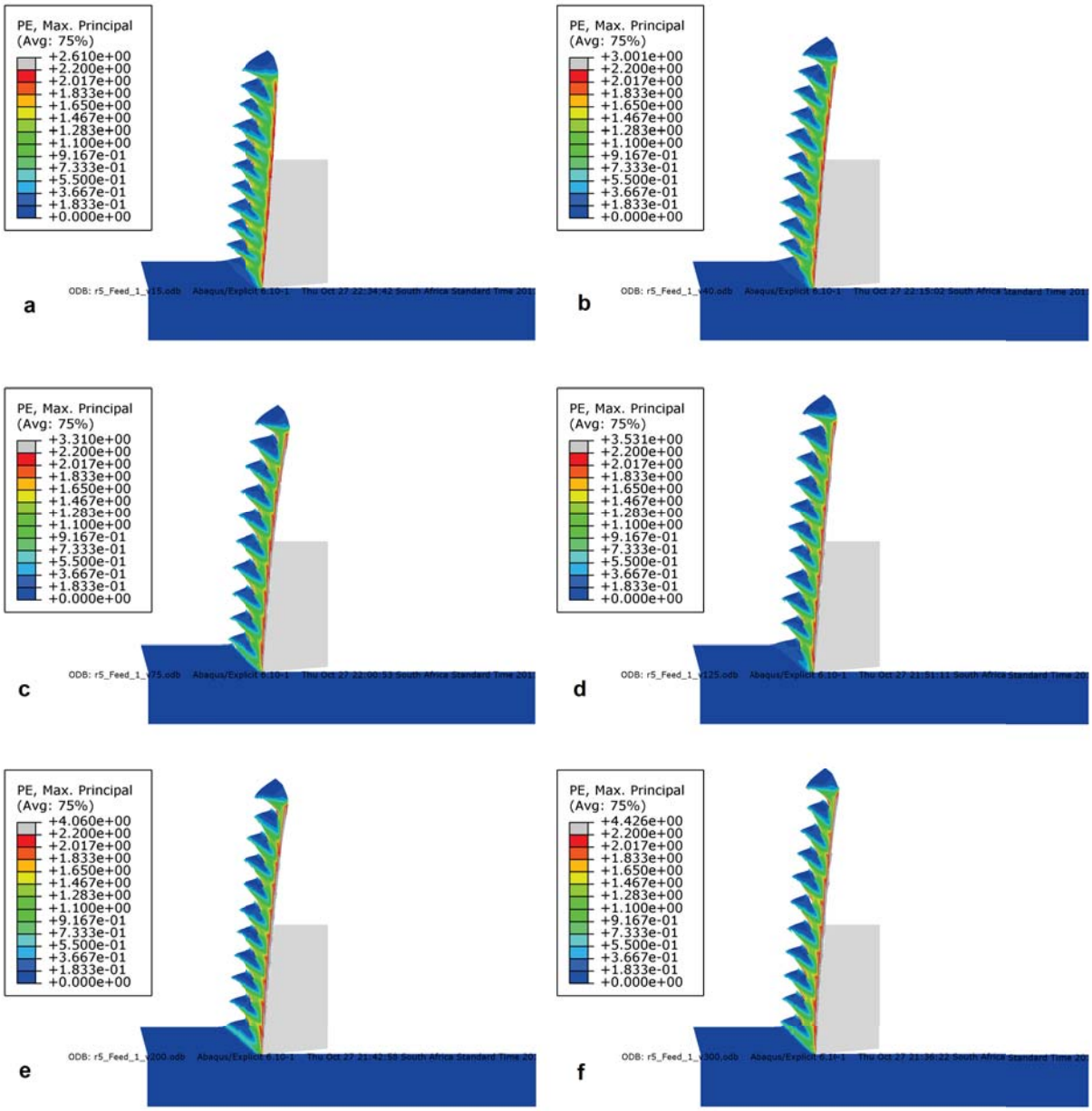

Figure 5.21: FE prediction of plastic strain distribution in the chip with $feed = 0.025$ mm/rev and $v = 15; 45; 75; 125; 200; 300$ m/min (image a-f)

distance along the chip underside. The model predicts cutting temperatures with good accuracy, except at low cutting speeds. The maximum chip underside temperature is also plotted for comparison and is approximately $200°C$ higher than at the measured location. When steady state conditions are reached in machining, tool temperatures can be expected to approach these levels.

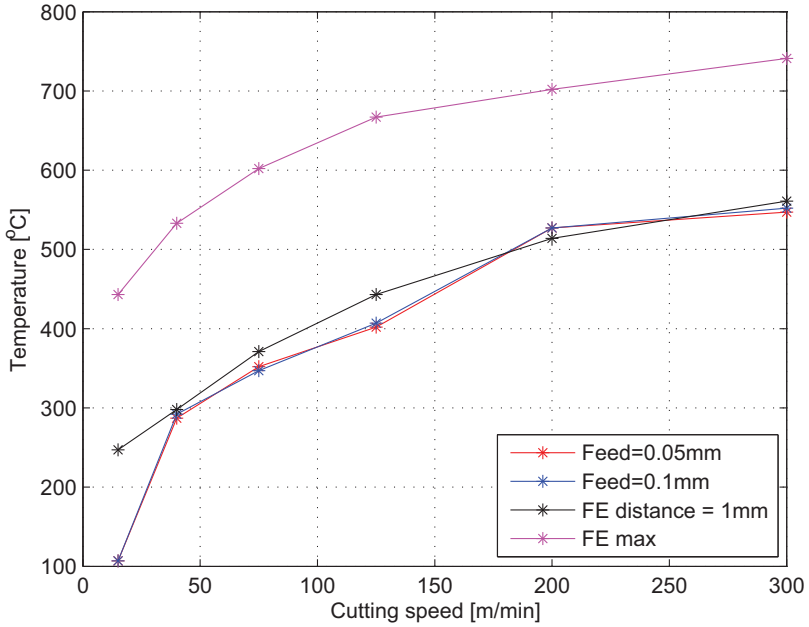

Figure 5.22: FE prediction vs experimentally determined chip temperatures $1mm$ from the cutting edge

5.1 Summary

A fully coupled temperature-displacement, explicit finite element model is implemented in this chapter to model the orthogonal cutting of Ti6Al4V alloys. The model employs the Johnson-Cook material model to describe the material flow and fracture behaviour so that chip separation and segmentation through element deletion is achieved. The model is thus able to predict the formation of segmental or saw-toothed chips, as observed in actual machining of titanium alloys.

The segmental chip shape prediction shows a close resemblance to the actual chips obtained and the cutting forces are well predicted, but there some discrepancies due to limitations of the model and the use of material model parameters obtained from literature. The temperature prediction compares well with the values obtained in orthogonal turning tests and the model is useful in the analysis of temperature in the material and the cutting tool. The model, however, cannot predict the effects of tool edge radius and the associated forces generated.

Chapter 6

Milling force prediction model

Predictions of the components of cutting forces in machining operations are required for the determination of power requirements, geometrical errors as well as chatter and vibration characteristics. Furthermore, predictions may assist in the design of fixtures and tools in terms of strength requirements in machining setups [68]. The optimisation of cutting strategies in computer-aided process planning also requires force predictions. Knowledge of machining forces can assist in the selection of cutting conditions that reduce excessive cutter wear and breakage [69].

Up to the late 1990's the traditional approach to modelling practical machining operations had been an empirical approach where process parameters such as cutting speed, feed and depth of cut are related to experimentally determined, average force components through curve fitting techniques [68]. These models provide only an average value of force components and are, therefore, only applicable to operations where the forces do not vary cyclically, such as in turning and drilling operations.

For operations where forces fluctuate cyclically, such as in milling, semi-empirical or mechanistic approaches have been adopted in the past. With these techniques, force component coefficients are related to chip load through milling tests using curve fitting techniques. The empirically established force coefficients are used in mechanistic analyses to predict instantaneous force components and fluctuations during cutter rotation. The force component coefficients here, and in other empirical approaches, are valid only for a given tool-workpiece combination and a range of machining tests has to be repeated for every combination of tool and workpiece.

In contrast, the "fundamental" or "unified mechanics of cutting" approach is a non-empirical method which incorporates "edge forces" and relates the developed analyses of practical operations such as turning, drilling and milling to the "classical" oblique cutting process, together with the basic cutting quantities found from orthogonal cutting tests. The basic cutting quantities from orthogonal tests form a generic data bank for a tool-workpiece material combination and may be used to model any machining operation. The orthogonal data base consists of shear stress, shear and friction angle data from tests conducted at a range of cutting speeds, feeds and rake angles and Budak *et al.* showed accurate transformation between these quantities and oblique cutting processes applied to cylindrical end mills [68]. The model incorporates all tool and cut geometrical variables, as well as cutting conditions and can, as result, be used to model any machining operation and cutter geometry.

6.1 Unified mechanics of cutting

In general, the elemental forces acting on a discrete, oblique cutting edge segment can be described by 6.1 in the tangential, axial and radial directions. Here the total force in a particular direction is separated into two components. The first component describes the edge forces, which are the forces due to rubbing and ploughing at the cutting edge, due to the radius found on practical cutting edges. The edge forces are represented by the edge force coefficients, K_{te}, K_{re} and K_{ae}, on a unit width of cut basis. The second part represents the cutting forces, which are due to shearing of the material in the shear zone and friction along the rake face. The coefficients K_{tc}, K_{rc} and K_{ac}, on a unit area of cut basis, make up the cutting force component of 6.1.

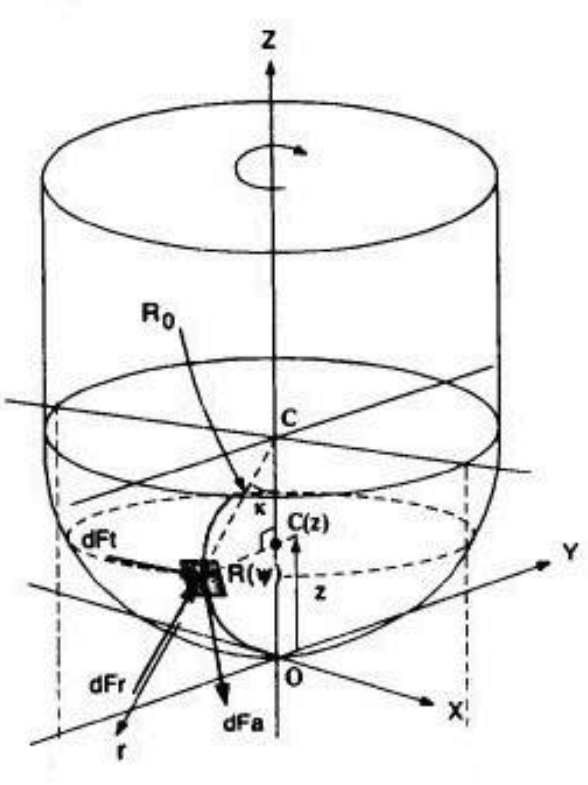

Figure 6.1: Ball nose end-mill coordinate system and differential forces acting on an edge segment [69]

In traditional mechanistic milling models, K_{te}, K_{re}, K_{ae}, K_{tc}, K_{rc} and K_{ac} are referred to as milling force coefficients and are determined through specific milling tests and mechanistic analyses. Tests consist of a series of slot milling tests run at various speeds and feeds and are valid only for the specific cutter geometry with which the tests are conducted. In contrast, with the unified mechanics of cutting approach, the coefficients are identified from an orthogonal cutting database, calculated from oblique or orthogonal cutting analysis, and can thus be predicted for any cutter geometry.

$$
\begin{aligned}
dF_t &= \overbrace{K_{te}\,dS}^{\text{edge}} + \overbrace{K_{tc}t_n\,db}^{\text{shear}} \quad (a)\\
dF_r &= K_{re}\,dS + K_{rc}t_n\,db \quad (b)\\
dF_a &= K_{ae}\,dS + K_{ac}t_n\,db \quad (c)
\end{aligned}
\tag{6.1}
$$

The method of predicting machining forces in milling, or indeed any other type of cutting operation, using the "unified mechanics of cutting" approach is based on the formulation described in 6.1. The general procedure for modelling milling is to divide the cutter geometry into discrete cutting edge elements and to define the geometry in terms of rake angle, helix or obliquity angle i in terms of a local coordinate system, the velocity U of each edge segment and the variation of cut thickness with cutter rotation angle θ. Once this information is known the cutting and edge force coefficients for each edge segment can be calculated at each increment of cutter rotation from the orthogonal cutting data base. The forces acting on each segment can then be calculated in the local tangential radial and axial directions and transformed to a global coordinate system and integrated over all the segments to give the total cutting forces in the global coordinate system as a function of cutter rotation.

6.2 Oblique analysis from orthogonal data

As stated in Chapter 6, the orthogonal data base can be assembled from oblique or orthogonal cutting tests. In order to achieve this, the cutting and feed force data, as well as chip thickness data, is collected from a range of cutting tests as detailed in Chapter 3.2.

For each particular cutting speed investigated, the cutting and feed forces are extrapolated to zero cut thickness through a data fit of the force data at various feeds. This is illustrated in Figure 6.2, where the values for cutting and feed forces at $feed = 0\,\text{mm/rev}$ have been calculated by fitting a cubic spline to the data. These forces are known as the cutting, F_{Pe}, and feed, F_{Qe}, edge forces. These forces represent the forces generated due to rubbing and ploughing of the cutting edge radius. Theoretically, an infinitely sharp cutting edge would thus have no edge forces while a large radius would generate higher edge forces.

Once the edge forces have been determined, those power, F_{Pc}, and thrust, F_{Qc}, force components that are due to cutting alone can be determined from 6.2 and 6.3, where F_{Pt} and F_{Qt} are the total cutting and feed forces as measured from the cutting tests. F_{Pc} and F_{Qc} represent the forces generated in the cutting operation due to shearing of the material and friction along the rake and flank faces of the cutting edge and are thus the dominant forces present at higher feeds, as the edge forces remain constant, while the cutting forces increase almost linearly with feed in most materials.

$$F_{Pt} = F_{Pe} + F_{Pc} \tag{6.2}$$

$$F_{Qt} = F_{Qe} + F_{Qc} \tag{6.3}$$

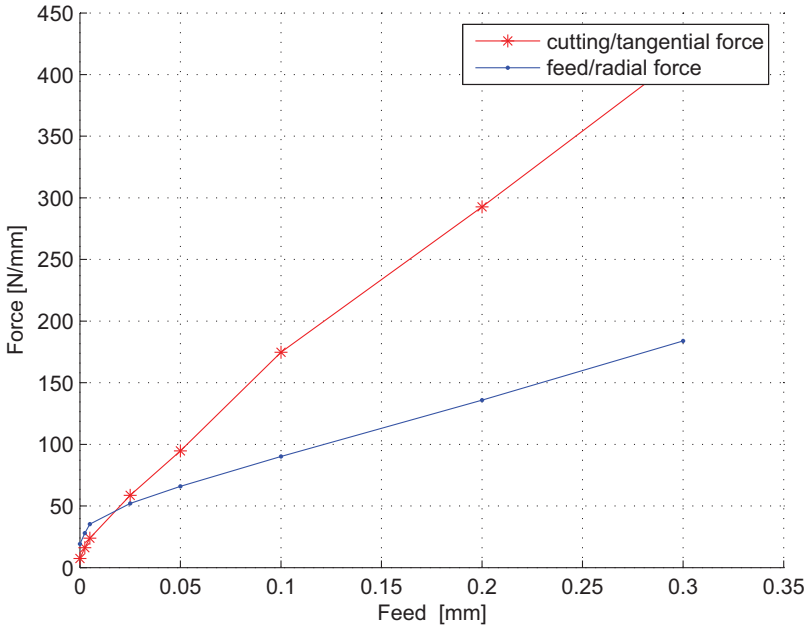

Figure 6.2: Machining forces vs. feed at V=40 m/min extrapolated to zero feed

The orthogonal database can now be calculated from 6.5-6.6. τ is the shear stress in the primary shear zone detailed in section 2.4 and ϕ is the shear angle or the angle the shear plane makes with the machined surface described in section 2.3. β is the average friction angle at the rake face of an orthogonal cut, while b, t and r are the cut width, uncut chip thickness and ratio of cut to uncut chip thickness, or compression ratio, respectively.

$$\tau = \frac{(F_{Pc}\cos\phi - F_{Qc}\sin\phi)\sin\phi}{bt} \tag{6.4}$$

$$\tan\phi = \frac{r\cos\alpha}{1 - r\sin\alpha} \tag{6.5}$$

$$\tan\beta = \frac{F_{Qc} + F_{Pc}\tan\alpha}{F_{Pc} + F_{Qc}\tan\alpha} \tag{6.6}$$

Once τ, ϕ and β have been established, the cutting coefficients can be determined for oblique cutting conditions within the bounds of the test conditions: the range of cut thicknesses, rake angles and cutting speeds. The formulation and procedure for determining the cutting coefficients is detailed in the following paragraphs and a more detailed description can be found by referring to [68].

The oblique cutting geometry for an infinitesimal cutting edge element, AB, on a ball end mill is detailed in Figure 6.3. The chip velocity , V_c, is inclined to the plane P_n normal to the cutting edge at an angle i. The resultant cutting forces can be resolved into three mutually perpendicular components F_p , F_q and F_r using Merchant's theory [68][16]. F_p , F_q and F_r are the power, thrust and radial forces acting on the oblique cutting edge segment, respectively.

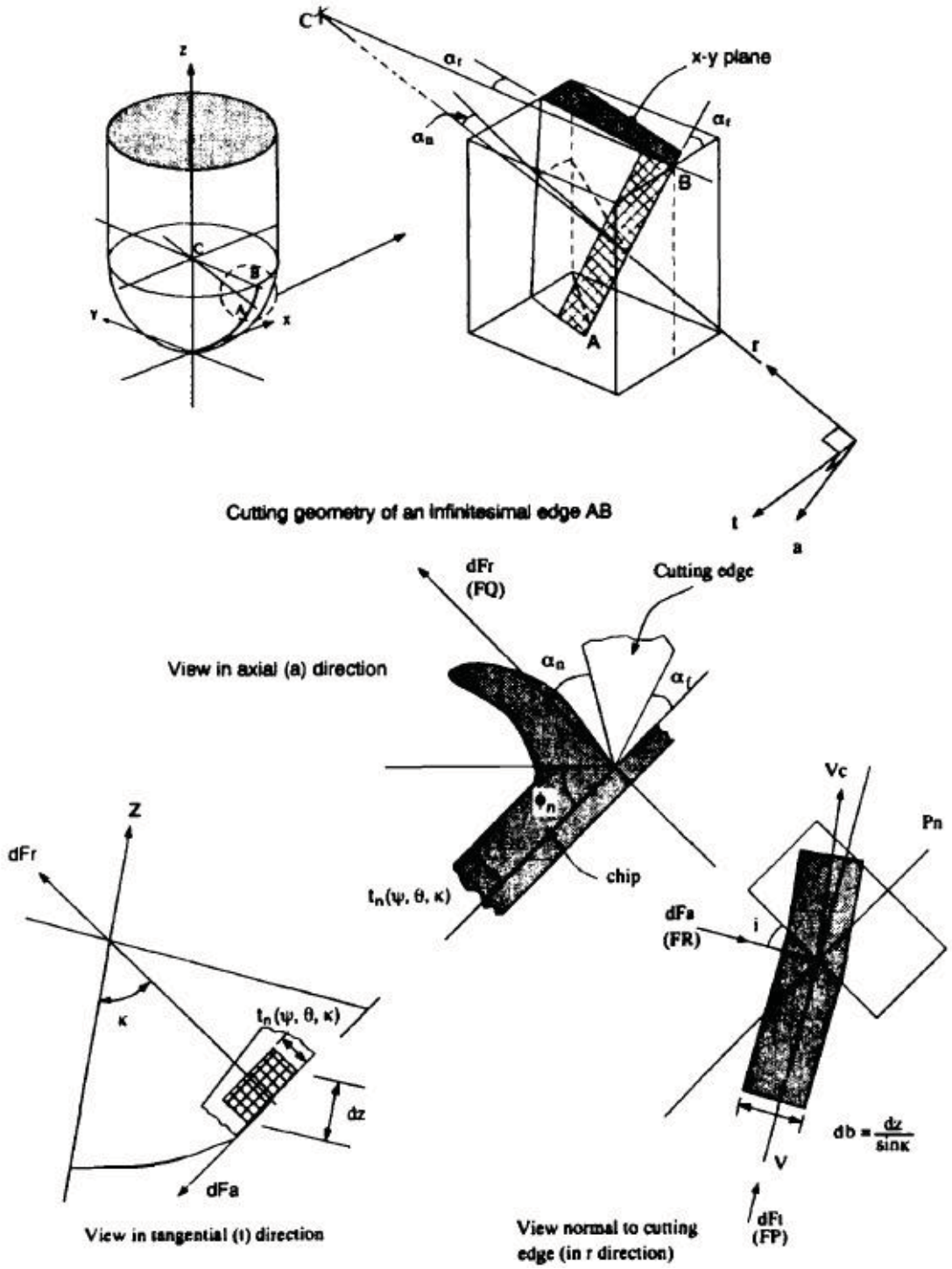

Figure 6.3: Oblique cutting geometry

$$F_p = \frac{\tau bt}{\sin\phi_n}\frac{\cos(\beta_n-\alpha_n)+\tan\eta_c\sin\beta_n\tan i}{c} \quad (a)$$

$$F_q = \frac{\tau bt}{sin\phi_n\cos i}\frac{sin(\beta_n-\alpha_n)}{c} \quad (b) \qquad (6.7)$$

$$K_r = \frac{\tau bt}{\sin\phi_n}\frac{\cos(\beta_n-\alpha_n)\tan i-\tan\eta_c\sin\beta_n}{c} \quad (c)$$

where

$$c = \sqrt{\cos^2(\phi_n+\beta_n-\alpha_n)+\tan^2\eta_c\sin^2\beta_n} \qquad (6.8)$$

The normal friction angle, β_n is defined as

$$\tan\beta_n = \tan\beta\cos\eta_c \qquad (6.9)$$

where η_c is known as the chip flow angle or the angle between a perpendicular to the cutting edge and the direction of chip flow over the rake face in the plane of the tool rake face. The normal shear angle can be obtained from the cutting ratio

$$\tan\phi_n = \frac{r_t\cos\alpha_n}{1-r_t\sin\alpha_n} \qquad (6.10)$$

α_n is normally constant and set during cutter grinding, while r_t, the chip thickness ratio in oblique cutting, can be related to the orthogonal parameter r by the following relation

$$r_t = r\frac{\cos\eta_c}{\cos i} \qquad (6.11)$$

The model may be further simplified by applying the Stabler rule, which states that the chip flow angle, η_c is approximately equal to the local inclination or helix angle i. Then r_t is approximately equal to r. The force components, dF_t, dF_r and dF_a, on a small edge segment in Figure 6.3 are compatible with the power, thrust and axial force components in oblique cutting. This is true when the elemental thickness t and width of cut b are given by the instantaneous chip thickness, $t_n(\Psi,\theta,\kappa)$ and length $dz/\sin\kappa$. The milling force coefficients due to cutting in 6.1 can be expressed in terms of the transformed cutting coefficients.

$$K_{tc} = \frac{\tau}{\sin\phi_n}\frac{\cos(\beta_n-\alpha_n)+\tan\eta_c\sin\beta_n\tan i}{c} \quad (a)$$

$$K_{rc} = \frac{\tau}{sin\phi_n\cos i}\frac{sin(\beta_n-\alpha_n)}{c} \quad (b) \qquad (6.12)$$

$$K_{ac} = \frac{\tau}{\sin\phi_n}\frac{\cos(\beta_n-\alpha_n)\tan i-\tan\eta_c\sin\beta_n}{c} \quad (c)$$

6.3 Unified mechanics of cutting for ball-end mills

In this section the "unified" mechanics of cutting method is applied to model a constant lead, ball-end mill geometry which was presented by Altintas and Lee [69]. This model is used as verification of orthogonal data obtained from cutting tests in this study, and forms the precursor to a more general milling case where a ball end mill of unknown geometry is modelled in this study. This is achieved through the use of a coordinate measuring machine to determine cutter geometry and demonstrates the flexibility of the method of unified mechanics in predicting machining forces for an arbitrary cutter. This will be presented in the next section.

6.3.1 Ball mill geometry

Figure 6.4(a)-(d) illustrates the detailed geometry of a ball end milling cutter. The cutter is ground with constant lead flutes which lie on the surface of a hemispherical plane. The flutes may be defined as having a helix angle i_0 at the intersection of the shank and the ball of the cutter. The local helix angle, $i(\psi)$, varies toward the tip of the cutter due to the reduction in the radius of the cutter in the $x-y$ plane with increasing distance in the z direction. The envelope of a sphere may be described in cartesian coordinates by

$$x^2 + y^2 + (R_0 - z)^2 = R_0^2 \tag{6.13}$$

where R_0 is the radius of the sphere at the centre, $z = 0$. The cutter radius at a location along the z axis is

$$R^2(z) = x^2 + y^2 \tag{6.14}$$

The z-coordinate of a point located on the cutting edge is

$$z = \frac{R_0 \psi}{\tan i_0} \tag{6.15}$$

Where ψ is the lag angle, due to the cutter helix, between the flute tip at $z = 0$ and at an axial location z. This concept is shown in Figure 6.4(b) and is measured clockwise from the positive y-axis. The centre of the local coordinate system is coincident with the global $X - Y - Z$ and is located at the tip of the cutter at point 0 in the figure.

The local helix angle, $i(\psi)$, in a constant lead cutter can be found from the following expression

$$\tan i(\psi) = \frac{R(\psi)}{R_0} \tan i_0 \tag{6.16}$$

The cutter radius at a point in the $x-y$ plane on the cutting flute, at an angle ψ, can be formulated from the previous equations and is expressed as

$$R(\psi) = \sqrt{1 - (\psi \cot i_0 - 1)^2} \tag{6.17}$$

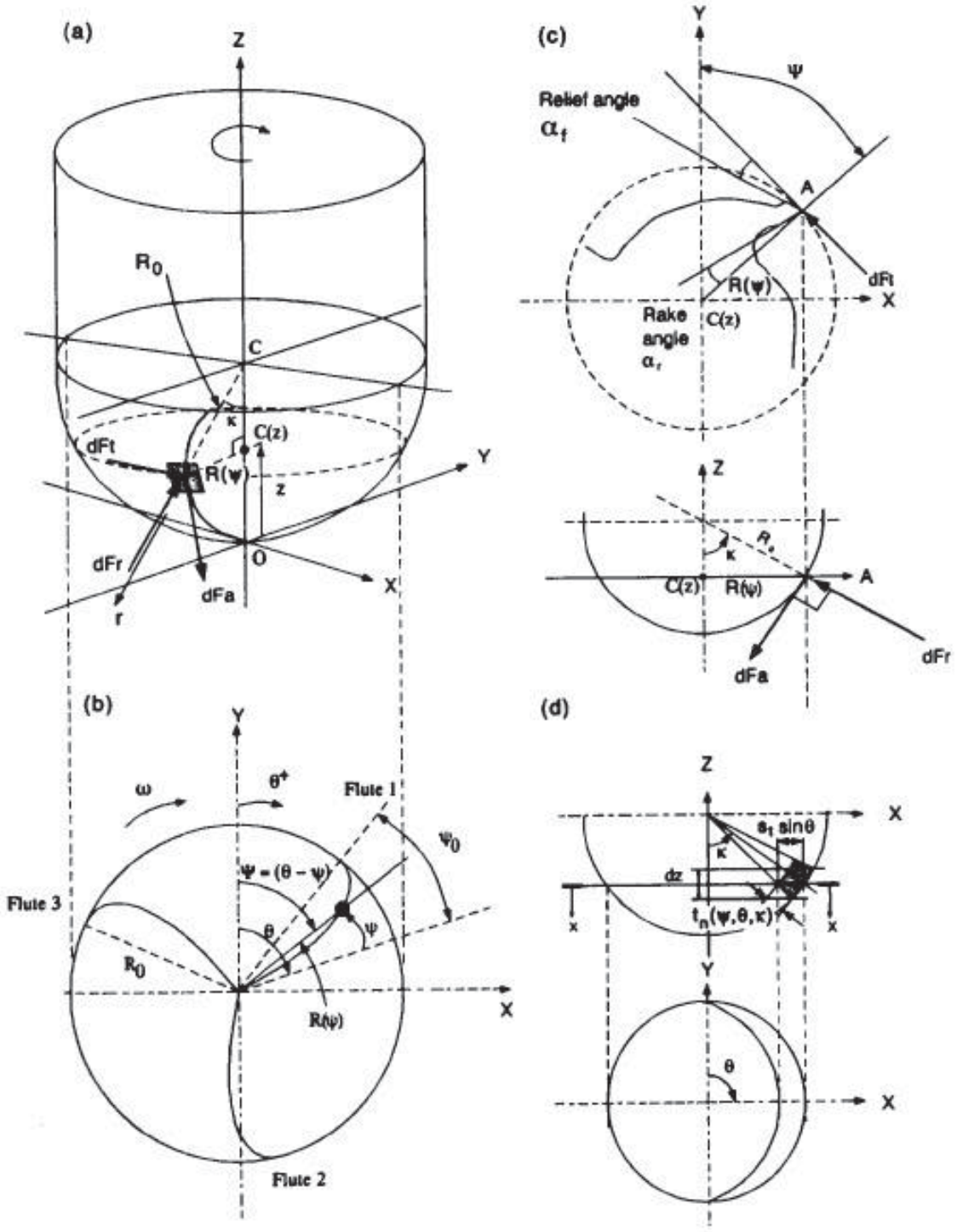

Figure 6.4: Ball nose mill geometry and coordinate system [69]

Equation 6.18 describes a vector drawn from the cylindrical coordinate centre, C, to a point on the cutting edge or flute

$$r(\psi) = R(\psi)(\sin\psi i + \cos\psi j) + R_0\psi\cot i_0 k \tag{6.18}$$

The length, dS, of an infintesimal curved cutting edge segment is defined by

$$dS = \sqrt{(R'(\psi))^2 + R^2(\psi) + R_0^2\cot^2 i_0}d\psi \tag{6.19}$$

where $R'(\psi)$ is the derivative of $R(\psi)$ and can be calculated from equation

$$R'(\psi) = \frac{-R_0(\psi\cot i_0 - 1)\cot i_0}{\sqrt{1-(\psi\cot i_0 - 1)^2}} \tag{6.20}$$

A point on flute j, at a height z, is referenced by its angular position, ψ in the global coordinate system according to

$$\Psi_j(z) = \theta + (j-1)\phi_p - \frac{z}{R_0}\tan i_0 \tag{6.21}$$

where

$$\phi_p = 2\pi/N_f \tag{6.22}$$

is the the pitch angle of the cutter flutes and N_f is the number of flutes on the cutter.

The instantaneous chip thickness normal to the cutting edge can be expressed by the following analytical expression and is a function of the radial position angle, θ, and the axial angle κ. This expression introduces an error which is only significant for small cut depths, a_p or when the ratio of a_p to cutter rotational velocity is high. An exact formulation for cut thickness may be found in references [70][17].

$$t_n(\psi,\theta,\kappa) = s_t\sin(\psi)\sin(\kappa) \tag{6.23}$$

κ is the angle measured between a line extending from the local origin, C, to a point on the cutting flute and the z-axis in Figure 6.4. It is described by the following relation

$$\kappa = sin^{-1}\frac{R(\psi)}{R_0} \tag{6.24}$$

With the ball end-mill geometry completely defined, the resultant elemental cutting forces, dF_t, dF_t and dF_t, acting on a cutting flute can be calculated from 6.25 in the tangential, radial and axial directions of the curvilinear local coordinate system. As mentioned in section 6.1, the cutting forces are separated into edge, (e), and shear, (c), force components. The edge force coefficients K_{te}, K_{tc} and K_{tc} in N/mm are constant and lumped at the edges of a cutting edge element and the magnitude of these components is found by multiplying them by the respective differential length, dS, (from 6.19) of the edge segment. K_{te}, K_{tc} and K_{tc}, identified from orthogonal cutting tests using an oblique transformation and detailed in 6.12. They represent the shearing forces

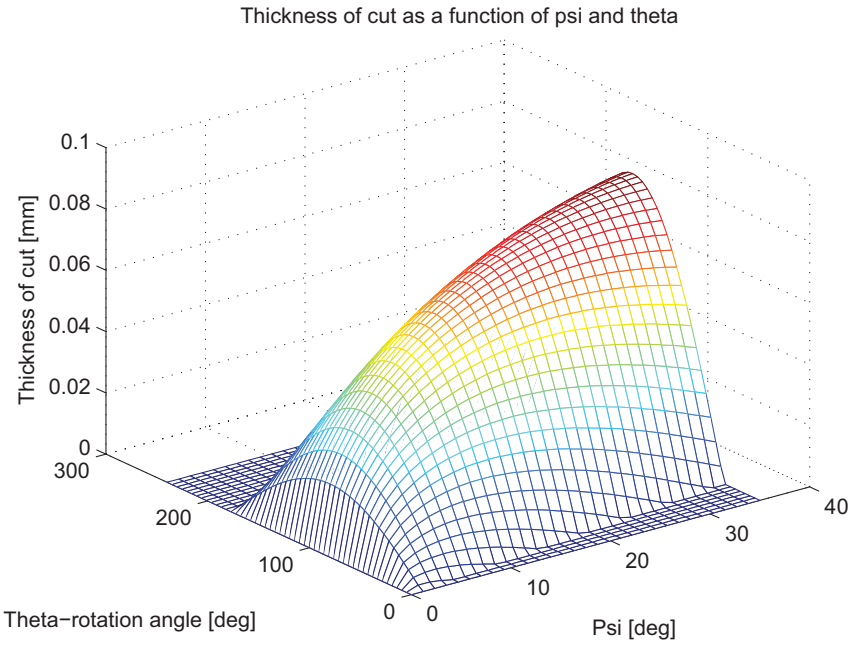

Figure 6.5: Uncut chip thickness as a function of cutter rotation θ and location on cutting flute Ψ. Full radial immersion, axial immersion=6 mm $feed = 0.1$ mm/rev

per unit area and are thus in the units N/mm^2. The force component of this part of 6.25 is found by multiplying the coefficient by the instantaneous chip thickness, t_n and the projected cut length or width of cut, db.

$$\begin{aligned} dF_t(\theta, z) &= K_{te}\, dS + K_{tc} t_n(\theta, \psi, \kappa)\, db \quad (a) \\ dF_r(\theta, z) &= K_{re}\, dS + K_{rc} t_n(\theta, \psi, \kappa)\, db \quad (b) \\ dF_a(\theta, z) &= K_{ae}\, dS + K_{ac} t_n(\theta, \psi, \kappa)\, db \quad (c) \end{aligned} \tag{6.25}$$

where

$$db = \frac{dz}{\sin \kappa} \tag{6.26}$$

The resultant forces in the global cartesion coordinate system may now be found by introducing a transformation matrix T, in 6.27 and 6.28, which is a function of κ and ψ. Figures 6.6-6.8 show the forces generated along the length of a cutting flute for a cutter revolution in the global coordinate system

$$dF_{xyz} = [T] dF_{rta} \tag{6.27}$$

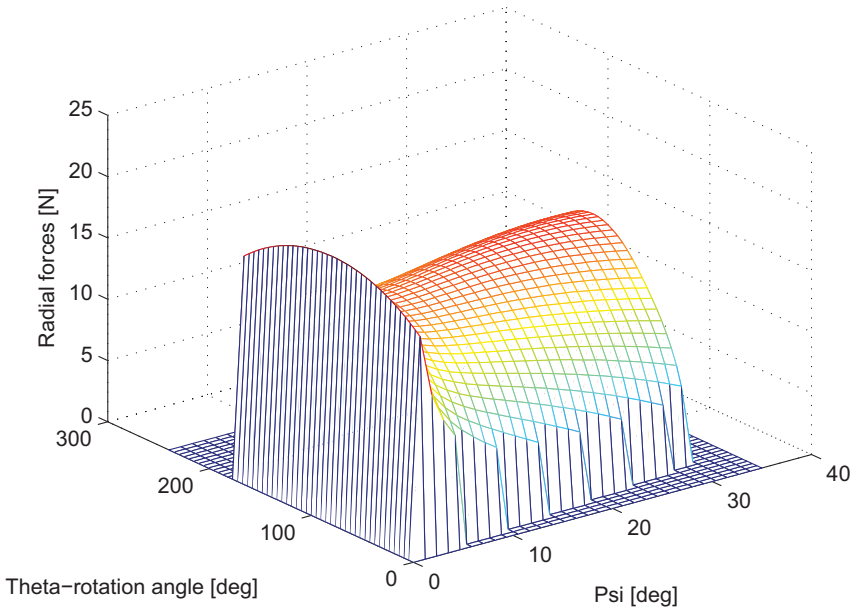

Figure 6.6: Radial machining forces as a function of Ψ and θ. Full radial immersion, axial immersion=6 mm $feed = 0.1$ mm/rev

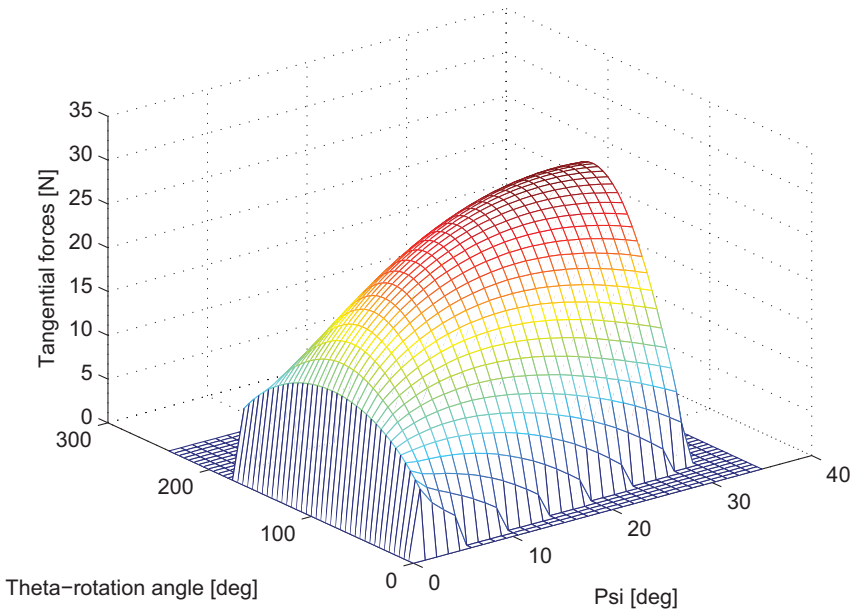

Figure 6.7: Tangential machining forces as a function of Ψ and θ. Full radial immersion, axial immersion=6 mm $feed = 0.1$ mm/rev

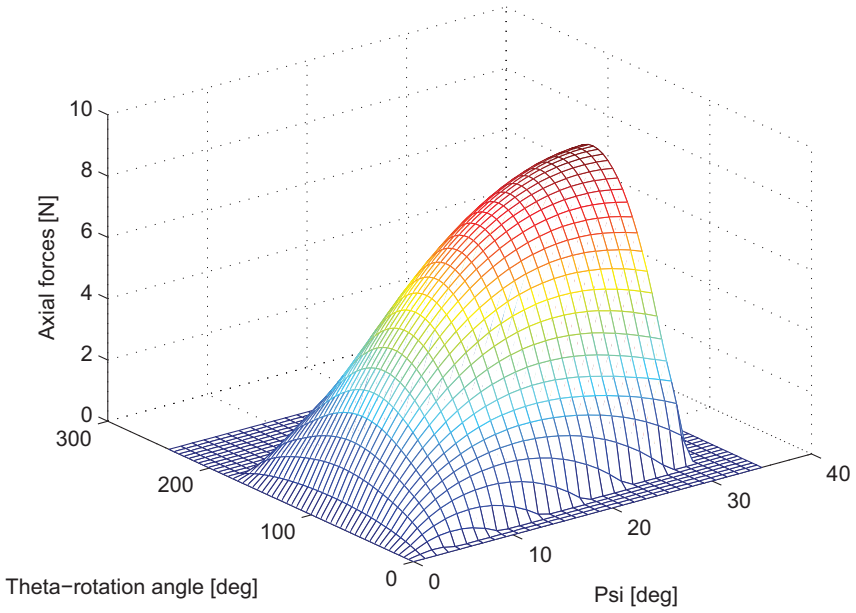

Figure 6.8: Axial machining forces as a function of Ψ and θ. Full radial immersion, axial immersion=6 mm $feed = 0.1$ mm/rev

$$\begin{pmatrix} dF_x \\ dF_y \\ dF_z \end{pmatrix} = \begin{pmatrix} -\sin(\kappa)\sin(\Psi) & -\cos(\Psi) & -\cos(\kappa)\sin(\Psi) \\ -\sin(\kappa)\cos(\Psi) & \sin(\Psi) & -\cos(\kappa)\cos(\Psi) \\ \sin(\kappa)\sin(\Psi) & 0 & -\sin(\kappa) \end{pmatrix} \begin{pmatrix} dF_r \\ dF_t \\ dF_a \end{pmatrix} \tag{6.28}$$

The forces acting on a particular flute, j, at a depth of cut, z, can then be found from

$$\begin{aligned} F_{xj}[\theta(z)] &= \int_{z1}^{z2} (-dF_{rj}\sin(\kappa_j)\sin(\Psi_j) \quad -dF_{tj}\cos(\Psi_j) \quad -dF_{aj}\cos(\kappa_j)\sin(\Psi_j))\,dz \quad (a) \\ F_{yj}[\theta(z)] &= \int_{z1}^{z2} (-dF_{rj}\sin(\kappa_j)\cos(\Psi_j) \quad +dF_{tj}\sin(\Psi_j) \quad -dF_{aj}\cos(\kappa_j)\cos(\Psi_j))\,dz \quad (b) \\ F_{zj}[\theta(z)] &= \int_{z1}^{z2} (\,dF_{rj}\sin(\kappa_j)\sin(\Psi_j) \quad -dF_{aj}\sin(\kappa_j))\,dz \quad (c) \end{aligned} \tag{6.29}$$

where the differential force components area function of the flute segment length, dS, instantaneous chip load, $t_n(\theta z \kappa)$, the cutter rotation angle, θ and the lag angle, ψ. Figure 6.12 shows the total forces generated for a cutter revolution.

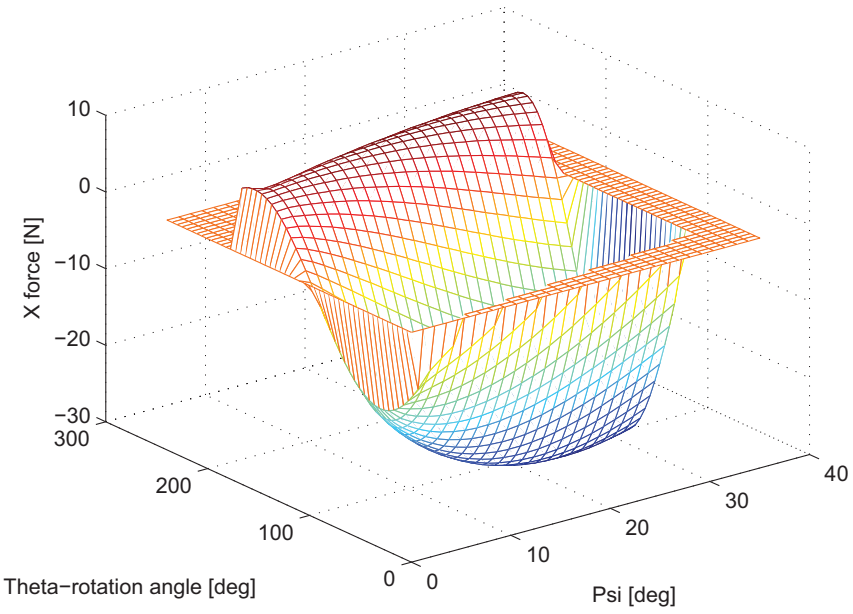

Figure 6.9: Machining forces in the global x direction as a function of cutter rotation. Full radial immersion, axial immersion=6 mm $feed = 0.1$ mm/rev

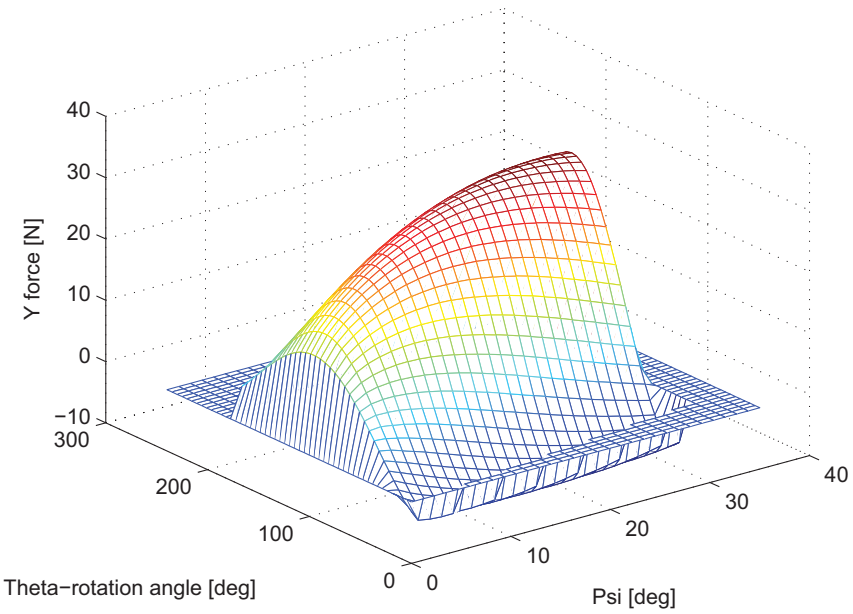

Figure 6.10: Machining forces in the global y direction as a function of cutter rotation. Full radial immersion, axial immersion=6 mm $feed = 0.1$ mm/rev

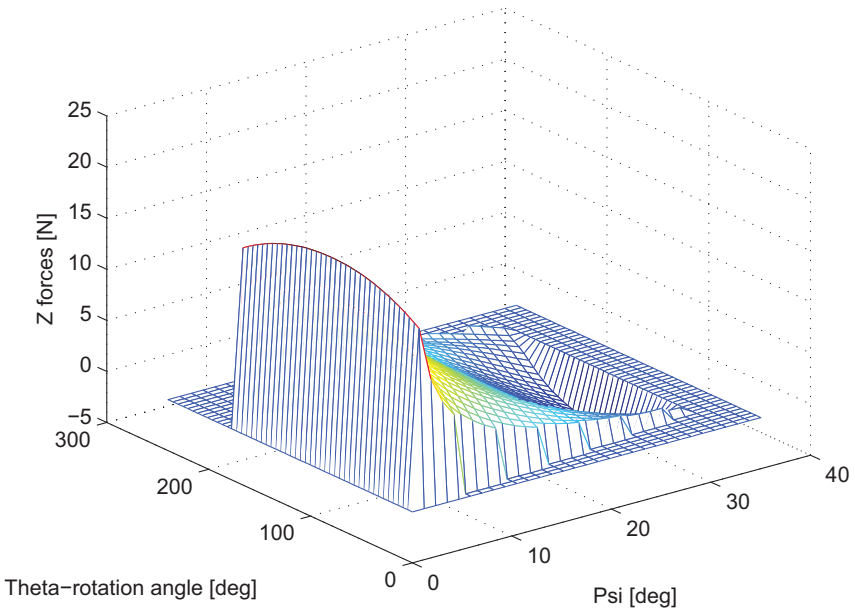

Figure 6.11: Machining forces in the global z direction as a function of cutter rotation. Full radial immersion, axial immersion=6 mm $feed = 0.1$ mm/rev

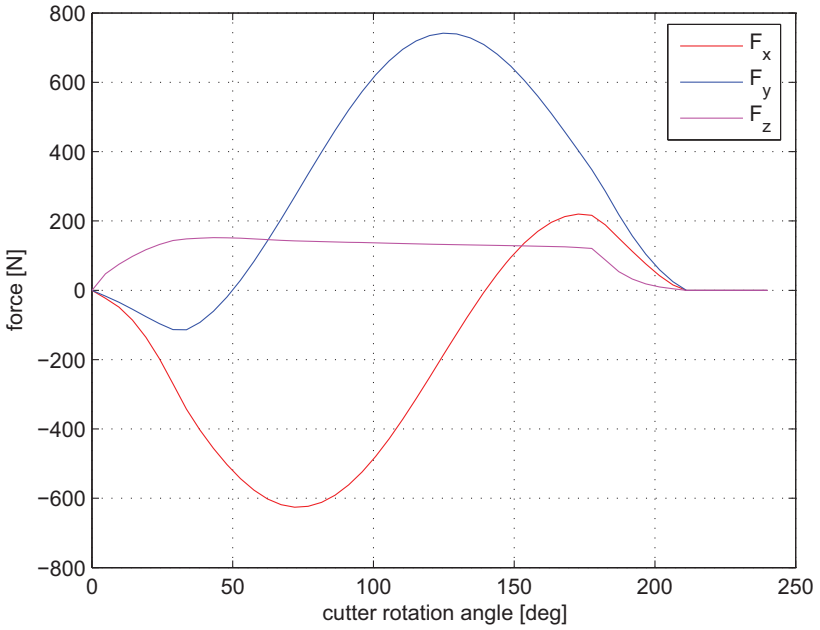

Figure 6.12: Total milling forces direction as a function of cutter rotation. Full radial immersion, axial immersion=6 mm $feed = 0.1$ mm/rev

6.3.2 Comparison with literature test and simulation

The ball nose milling model is implemented as detailed in the preceding sections according to the method formulated by Lee and Altintas [69]. In this section a comparison is made with the published cutting force predictions and test data. The published data is compared with the model prediction in this study using the orthogonal data obtained from the turning tests described in section 3.2.3. Figure 6.13 shows the compared forces for a ball nose mill with $radius = 9.525$ mm, $spindlespeed = 269$ rev/min, helix angle $i_o = 30^\circ$ cut thickness $s_t = 0.0508$ mm and an axial immersion $a = 6.35$ mm. The prediction is for a full immersion slotting operation. Figure 6.14 shows the model prediction versus published test and prediction data. In both cases the forces are well predicted.

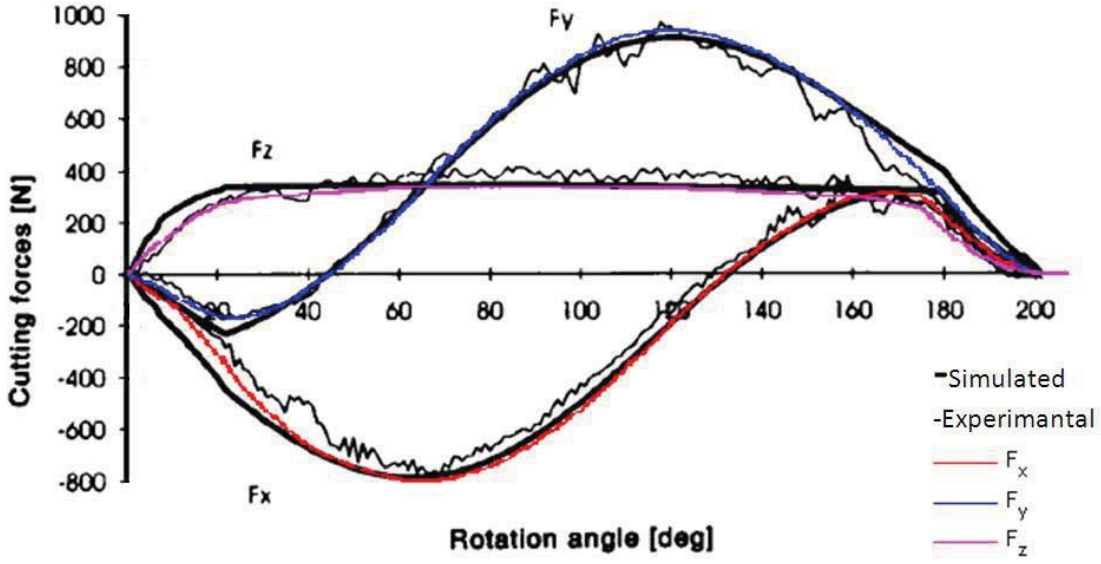

Figure 6.13: Measured and predicted slot milling forces for full immersion milling. Black lines correspond to test and simulation data obtained by [69] while coloured lines are predictions made in this study

Figure 6.13 shows the compared forces for a ball nose mill with $radius = 9.525$ mm, $spindlespeed = 269$ rev/min, helix angle $i_o = 30^\circ$ cut thickness $s_t = 0.102$ mm and an axial immersion $a = 6.35$ mm. The prediction is for a half immersion slotting operation

Cutting forces in both cases are well predicted and the models correlate well. This is an indication that the orthogonal cutting data measured and used in this study are similar to those obtained in the study conducted by Lee and Altintas.

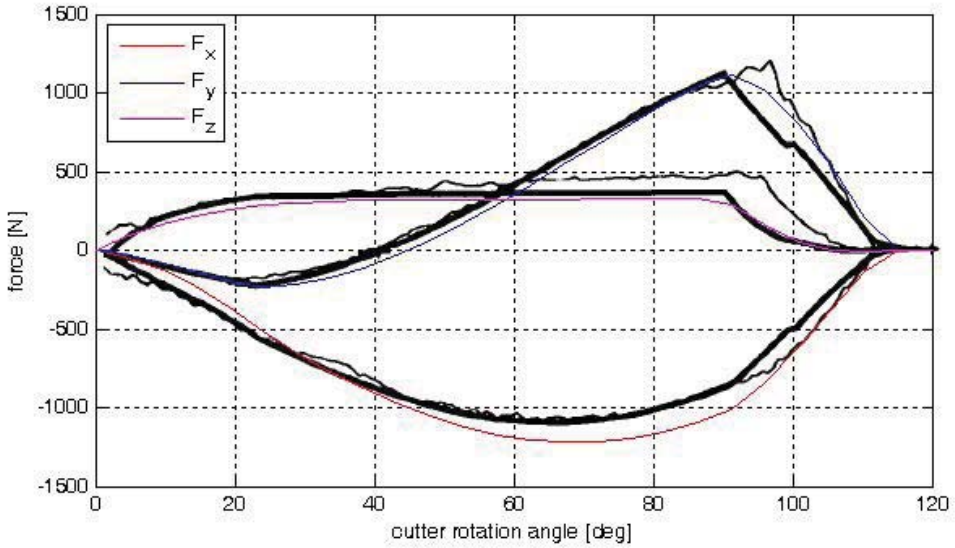

Figure 6.14: Measured and predicted slot milling forces for half immersion milling. Black lines correspond to test and simulation data obtained by [69] while coloured lines are predictions made in this study

6.4 Modelling arbitrary cutter geometry

Modern cutters are often not of the usual constant lead type designs described in section 6.3, but instead have flute geometries designed and optimised to improve cutter performance. To demonstrate the ability of the unified mechanics of cutting approach to model any cutter geometry, a 12 mm diameter ball nose cutter, of unknown flute design, was selected from the Sandvik range of carbide ball-end mills as described in section 3.3.

6.4.1 Defining geometry

The geometry of a flute on the cutter was scanned into a three dimensional CAD file (see figure 6.15) using a touch probe coordinate measuring machine. In the CAD environment, the coordinates of several points along the cutting edge were recorded and integrated into the Matlab code detailed in section 6.3 for the modelling of constant lead ball end mills. The same coordinate system was adopted which allowed for simple integration of the scanned cutter geometry into the program.

To accomplish this, the data was first smoothed and a 3-dimensional spline was fitted to improve the resolution of the curve by describing the flute as a polynomial function. Thereafter the $x-y$ coordinates of the fitted curve were transformed from the cartesian to polar coordinate system while the z-axis data remained unchanged. Figure 6.16 shows the flute plotted in the cartesian space. The edge geometry is then described as a function of ψ, R and z which is analogous with the geometry definition in section 6.3. Figure 6.17 plots this relationship for the Sandvic cutter. To complete the definition of the mill, the differential length, dS, and the helix angle, i, are measured from the

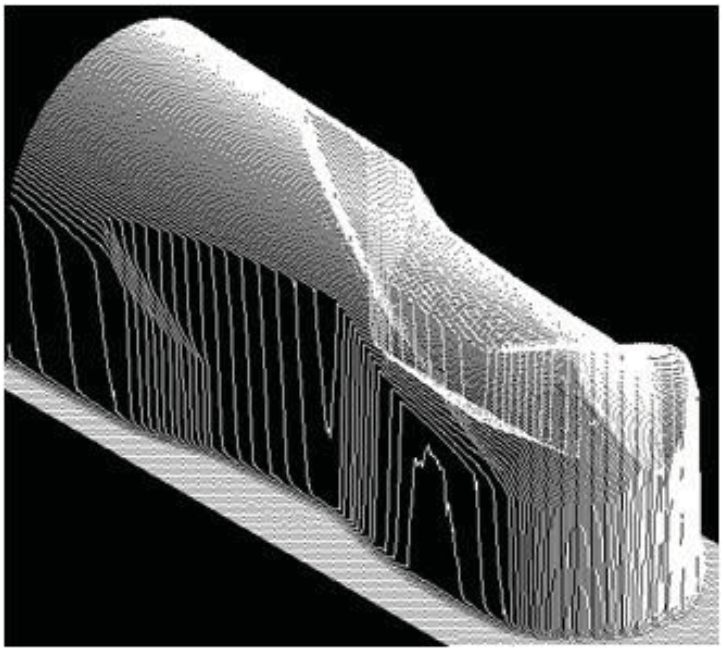

Figure 6.15: CAD model of Sandvik 12 mm ball nose end-mill

CAD model. The cutter has a variable rake angle which ranges from $0^\circ - 2^\circ$ and to simplify the cutter definition, the rake angle is assumed to be zero. This is justified, as the differences in cutting forces for such a small variation in angle are negligible and cutting tests did not indicate a significant difference between rake angles 0° and 5°.

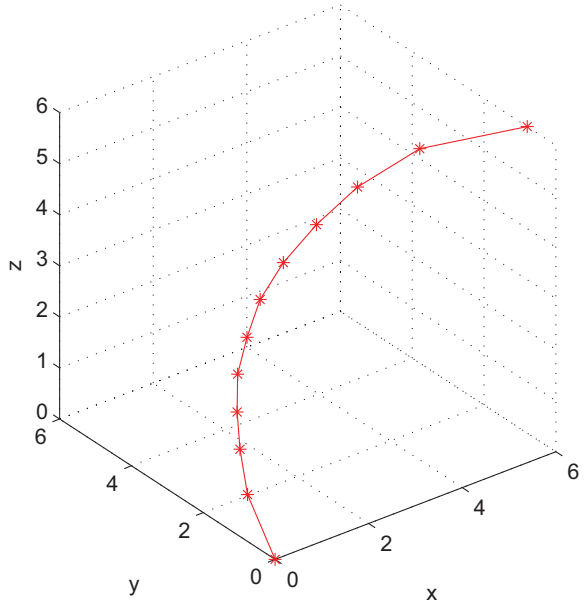

Figure 6.16: Sandvik ball nose flute geometry in the cartesian coordinate system

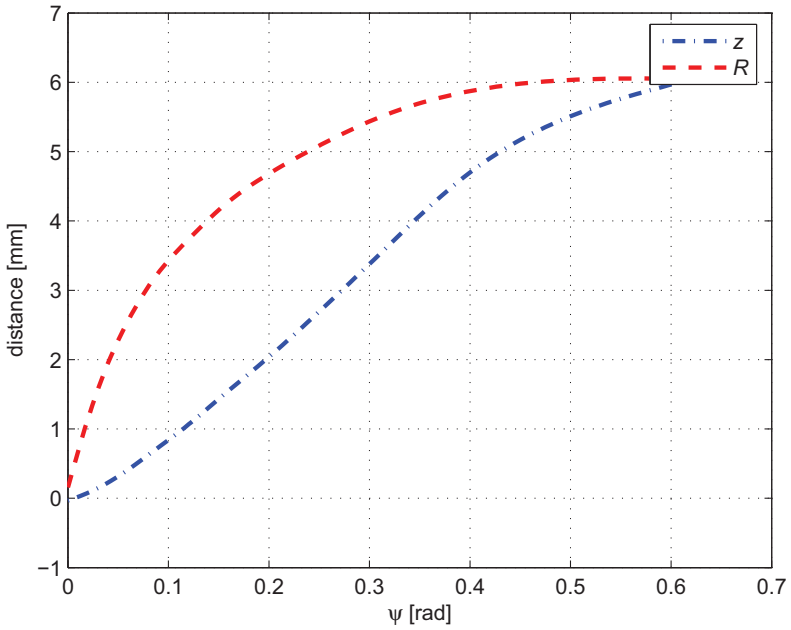

Figure 6.17: Sandvik ball nose flute geometry with ψ and z plotted as a function of axial distance from the cutter tip

6.4.2 Comparison with test data and prediction using FE orthogonal data

In this section force predictions for the Sandvic cutter are compared with the data obtained from slot milling tests described in 3.3. Furthermore milling predictions are made using the orthogonal machining data predicted in the finite element study of titanium machining in Chapter 4.

Figure 6.18 shows the milling forces predictions for full immersion up milling with $feed = 0.15$ mm/rev and axial depth of cut, $a = 4$ mm. Predictions are made using orthogonal data obtained in both in turning tests and from the finite element prediction.The predictions from the milling model correspond closely to those obtained in milling tests and the difference in the prediction made using experimental and FE data do not differ significantly at the cutting conditions modelled.

Figure 6.19 shows the milling forces predictions for half immersion up milling with $feed = 0.05$ mm/rev and axial depth of cut, $a = 3$ mm. In this case the force prediction does not match the milling experimental data well. The forces generated in this case are much smaller than in Figure 6.18 due to the relatively small feed and axial depth of cut. For small feed rates the contribution of the edge forces to the total force prediction is relatively large. Differences in predicted milling forces is thus affected more strongly by the edge condition of the milling cutting edge which is sharper than that of the insert used in obtaining orthogonal turning tests. The model still predicts the general shape of the cutting force plots reasonably well and cutting force magnitudes are assumed to be satisfactory for most applications of the model.

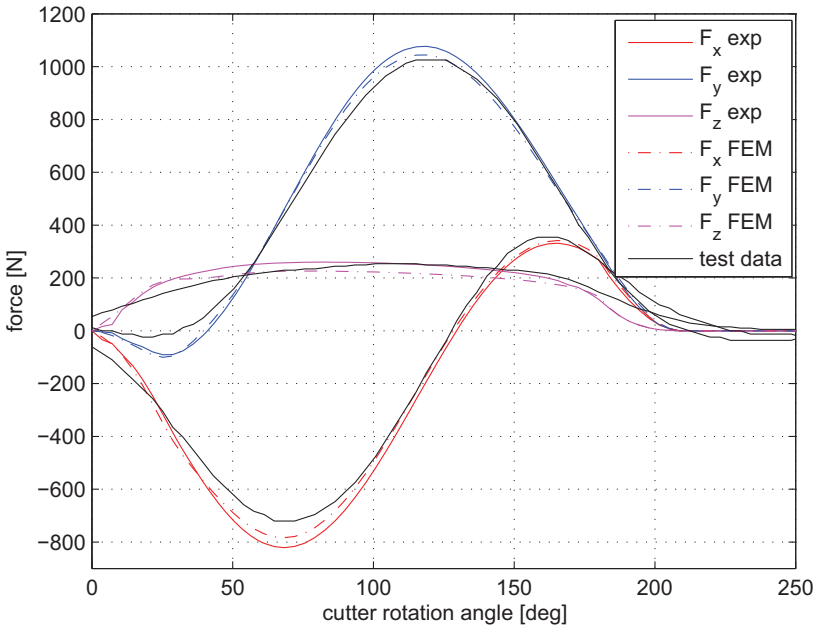

Figure 6.18: Ball nose cutting forces predicted from orthogonal data, FE othogonal data and measured forces for arbitrary cutter geometry

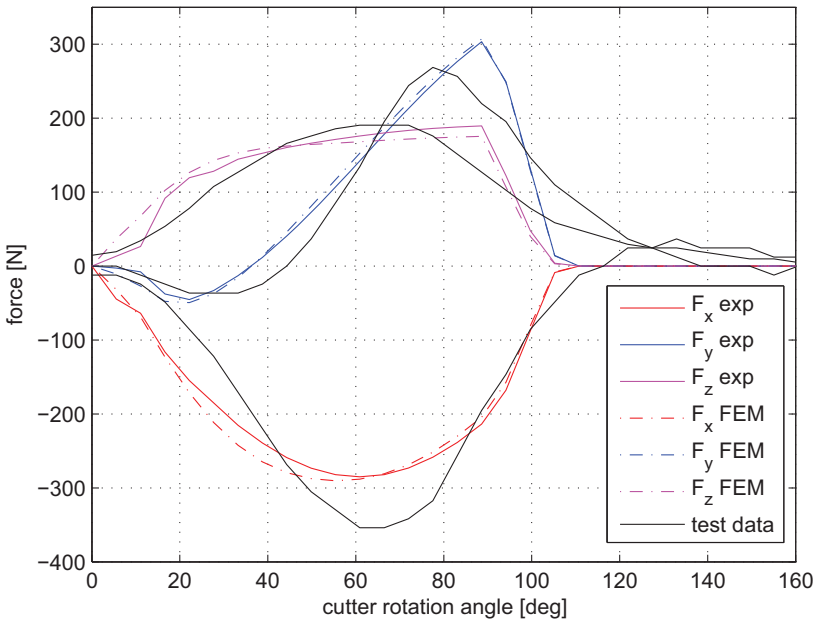

Figure 6.19: Ball nose cutting forces predicted from orthogonal data, FE othogonal data and measured forces for half immersion cutting

6.5 Summary

In this chapter the milling force prediction model based on the "unified mechanics of cutting" theory is implemented. The model uses both the orthogonal cutting data obtained through machining tests and those from the predictions of the finite element model. For the case of ball nose milling with a constant lead flute geometry, the force prediction corresponds well with published data. A ball nose mill of initially unknown edge geometry is also modelled from a touch probe scan of the cutter geometry and compared with the machining forces obtained in milling tests with the cutter. Cutting forces are well predicted when either the orthogonal finite element data or test data are used in the model.

Deviations in predictions from the measured data may be attributed to several factors. The first being that the edge preparations of the end mill differs significantly from that of the turning insert from which the orthogonal database is established. The ball mill has a ground edge and is thus sharper than the turning inserts, which is finely finished only on the top surface. Variations may also be attributed to cutter run-out or eccentricity and deflection of the tool and milling machine. Tool deflection affects the cut geometry, and thus the instantaneous cut thickness, and has a strong influence on the cutting forces.

Chapter 7

Summary

The purpose of this study is to develop numerical models for the prediction of cutting forces and temperatures generated when machining titanium. The approach taken is twofold and makes use of both a finite element model, which models the orthogonal machining case, and the "unified mechanics of cutting" approach which is implemented for the prediction of milling operations.

An extensive range of orthogonal cutting tests was performed and data was collected in terms of cutting forces, chip analysis and temperature measurements. Micro structural analysis was also conducted on the working material, as were hardness tests. The orthogonal data is used to establish an orthogonal cutting database for verification and comparison with the finite element model and is also used in the "unified mechanics of cutting" model. Slot milling tests were conducted using a ball nose mill to measure cutting forces during milling for comparison with the predictions of the "unified mechanics of cutting" model.

A fully coupled temperature-displacement, explicit finite element model is implemented in Chapter 4 to model the orthogonal machining case. The model employs the Johnson-Cook material model to describe the material flow and fracture so that chip separation and segmentation is modelled. The segmental chip shape shows a close resemblance to the actual chips obtained and the cutting forces are well predicted, but there some discrepancies due to limitations of the model and the use of material model parameters obtained from literature. The temperature prediction compares well with the values obtained in orthogonal turning tests and the model is useful in the analysis of the effects of temperature in the material and cutting tool. The model, however, cannot predict the effects of tool edge radius and the associated forces generated.

In Chapter 6 the milling force prediction model, based on the "unified mechanics of cutting", is implemented. The model was implemented using orthogonal force data obtained from machining tests and from the predictions of the orthogonal cutting finite element model. The predicted and measured cutting forces are used independently to populate the orthogonal cutting database used in the milling model. In this study a generic ball nose cutter geometry was modelled and compared with results from literature. The force prediction in this case corresponds well with published data using either FE or test data. An off the shelf ball nose cutter was also modelled by scanning the geometry using a touch probe scanner and incorporating it in the milling model. The model predictions are compared with the machining forces obtained in milling tests. Cutting forces are reasonably well predicted when either the orthogonal finite

element or test data are used in the model.

Chapter 8

Conclusion

The finite element model implemented in this study shows good correlation with experimental data in terms of cutting force and temperature prediction as well as the chip shape. The model is however unable to predict the cutting edge forces that are due to rubbing and plowing of the of the cutting tool due to a finite edge radius. The model is only able to model an infinitely sharp cutting edge and in this study the edge forces were calculated from experimental work. The experimental work however shows that the edge forces are independent of the cutting conditions and are only a function of the edge radius and finish and the material couple.

There are several ways in which a tool with an edge radius may be modelled but they pose their own specific problems. One such metod would be to use an algorithm to continuously remesh the area around the tool edge so that no predefined cutting or parting line has to be employed. Abaqus however has only limited remeshing capabilities. Remeshing is achieved through redistributing the nodes and remapping the stress field onto the new mesh. It does not have the capability of adding new nodes to the system and failed when implemented in the model. A second method would be to use a mixed Lagrangian-Eulerian model where the tool and workpiece are meshed using a lagrangian mesh and a the area of the workpiece around the tool and the chip is meshed using Eulerian elements. This method was also implemented but failed to produce saw tooth chips and was thus deemed unsuitable.

For further studies it is recommended that a custom remeshing algorithm is implemented so that the flow of material around the cutting edge can be realistically modelled. The limitation here would be computational expense as the elements around the edge would need to be smaller than the edge radius modelled to accurately capture the behaviour of the material at the tool edge. Because an explicit formulation is employed, a small time increment would be introduced and the computational time will be greatly increased.

Another shortcoming of the model is that conduction of heat out of the system is not considered and the model is thus incapable of modelling steady state machining temperatures. The model is valid in terms of heat generation in the work piece due to plasticity and friction but the temperature distribution in the tool is not accurately predicted. The thermal modelling is however useful in gaining insight into the influence of machining conditions on the temperatures generated in the system.

The milling model has been proven in literature to provide accurate prediction of machining forces given that the orthogonal cutting database is accurate. It is important

that the tool preparation in the orthogonal or oblique cutting tests closely matches that of the tool being modelled. It is thus important that edge radius, surface finish and tool coatings are well matched. In this study this was not controlled but reasonable predictions of milling forces were still obtained and deemed adequate for the study.

In the milling tests the results when milling at conditions where small machining forces were generated were not not useable. This was because the gain on the charge amplifier was not adjusted for different machining parameters and was only noted on data processing and repeat tests could not be conducted at this stage of the study. Repeat tests are recommended to remedy this. A shorter and tool is also recommended to reduce the effects of tool deflection.

6. List of References

[1] Abele, E. and Frohlich, B.: High speed milling of titanium alloys. *Advances in production engineering management*, vol. 3, no. 3, pp. 131–140, March 2008. (Cited on pages 1 and 4.)

[2] Merchant, M.E.: Mechanics of the metal cutting process i. orthogonal cutting and a type 2 chip. *J. Appl. Phys.*, p. 267, 1945. (Cited on page 5.)

[3] Barnett-Ritcey, D.: *High-speed milling of titanium and titanium aluminide: An experimental investigation*. Master's thesis, McMaster University, 2004. (Cited on pages viii, 5, 6, 7, and 8.)

[4] Komanduri, R. and Von Turkovich, B.: New observations on the mechanism of chip formation when machining titanium and its alloys. *Wear*, vol. 69, pp. 179–188, 1981. (Cited on page 6.)

[5] Rahman, M., Wang, Z. and Wong, Y.: A review on high-speed machining of titanium alloys. *JSME international journal*, vol. 49, p. 11, 2006. (Cited on page 7.)

[6] Ng, E.-G. and Aspinwall, D.K.: Modelling of hard part machining. *Journal of Materials Processing Technology*, vol. 127, p. 222, 2002. (Cited on pages viii, 8, 9, 30, 34, 36, 42, and 43.)

[7] Ng, E.-G., El-Wardany, T.I., Dumitrescu, M. and Elbestawi, M.A.: Physics-based simulation of high speed machining. *Machining Science and Technology*, vol. 6, no. 3, pp. 301–329, 2002. (Cited on pages ix, 8, 42, and 44.)

[8] Carrol III, J. and Strenkowski, J.: Finite element models of orthogonal cutting with application to single point diamond turning. *Int. J. Mech. Sci.*, vol. 30, pp. 699–920, 1988. (Cited on pages 8 and 30.)

[9] Chen, L., El-Wardany, T. and Harris, W.: Modelling the effects of flank wear land and chip formation on residual stresses. *CIRP*, vol. 53, p. 95, 2004. (Cited on pages 8, 42, 43, and 44.)

[10] Johnson, G. and Holmquist, T.: Test data and computational strengthen and fracture model constants for 23 materials subjected to large strain, high-strain rates, and high temperatures. *Los Alamos National laboratory*, p. 425Ű439, 1989. LA-11463-MS. (Cited on pages 9, 31, and 32.)

[11] Leopold, J., Schmidt, G., Hoyer, K. and Freitag, A.: Modelling and simulation of burr formation-state-of-the-art and future trends. *8th CIRP international workshop on modelling of machining operations*, pp. 73–83, 2005. (Cited on page 9.)

[12] Lundblad, M. and Kalhori, V.: Prediction of contact behaviour at chip-insert interface in machining. 8th cirp international workshop on modelling of machining operations. *8th CIRP international workshop on modelling of machining operations*, pp. 485–494, 2005. (Cited on page 9.)

[13] Ozel, T. and Zeren, E.: Finite element simulation of machining of aisi 1045 steel with a round edege cutting tool. *8th CIRP international workshop on modelling of machining operations*, pp. 533–540, 2005. (Cited on page 9.)

[14] Adibi-Sedeh, A., Vaziri, M., Pednekar, V., Madhavan, V. and Ivester, R.: Investigation of the effect of using different material models on finite element simulation of machining. *8th CIRP international workshop on modelling of machining operations*, pp. 215–224, 2005. (Cited on page 10.)

[15] Baker, M.: Some aspects of high speed chip formation. *8th CIRP international workshop on modelling of machining operations*, p. 101, 2005. (Cited on page 10.)

[16] Armarego, E. and Brown, R.H.: *The machining of metals*. Prentice Hall, New York, 1969. (Cited on pages 10 and 67.)

[17] Martelotti, M.: Analysis of the milling process. *Trans. ASME*, vol. 63, p. 667, 1941. (Cited on pages 10 and 72.)

[18] Altintas, Y. and Engin, S.: Generalized modelling of milling mechanics and dynamics: Part ii - inserted cutters. *International journal of machine tools and manufacture*, vol. 41, pp. 2212–2220, 2001. (Cited on page 10.)

[19] Altintas, Y. and Engin, S.: Generalized modelling of milling mechanics and dynamics: Part ii - inserted cutters. *International journal of machine tools and manufacture*, vol. 41, pp. 2212–2220, 2001. (Cited on page 11.)

[20] Lee, P. and Altintas, Y.: Prediction of ball end milling forces from orthogonal cutting data. *Elsevier science*, vol. 41, pp. 1059–1072, 1995. (Cited on page 11.)

[21] Gradisek, J., Kalveram, M., Weinert, K., Govekar, E. and Grabec, I.: Identification of specific cutting force coefficients for general end mill geometry. *8th CIRP international workshop on the modeling of machining operations*, pp. 283–291, 2005. (Cited on page 11.)

[22] Altintas, Y. and Engin, S.: Generalized modelling of milling mechanics and dynamics: Part ii - inserted cutters. *International journal of machine tools and manufacture*, vol. 41, pp. 2212–2220, 2001. (Cited on pages viii and 11.)

[23] Yavuz, B. and Tekka, A.: Correlation between vickers hardness number and yield stress of cold- formed products. *AFP Research Project*, vol. AFP-98-03-02-03, 2002. (Cited on page 14.)

[24] Vaz, M.J.: On the numerical simulation of machining processes. *Journal of the Brazilian Society of Mechanical Sciences*, vol. 22, no. 2, pp. 95–100, 2000. (Cited on pages ix, 26, 27, 30, 34, and 36.)

[25] Okushima, K. and Kakino, Y.: The residual stress produced by metal cutting. *Ann. CIRP*, vol. 20, pp. 13–14, 1971. (Cited on page 26.)

[26] Tay, A., Stevenson, M. and de Vahl Davis, G.: Using the finite element method to determine temperature distributions in orthogonal machining. *Proceedings Institution of Mechanical Engineers*, vol. 188, pp. 627–638, 1974. (Cited on page 26.)

[27] Hashemi, J., Tseng, A. and Chou, P.: Finite-element modelling of segmental chip formation in high-speed machining. *J. Materials Engng. Perf.*, vol. 3, pp. 712–721, 1994. (Cited on page 27.)

[28] Marusich, T. and Ortiz, M.: Modelling and simulation of high speed machining. *International Journal for Numerical Methods in Engineering*, vol. 38, pp. 3675–3694, 1995. (Cited on pages 27 and 28.)

[29] Usui, E., Obikawa, T. and Shirakashi, T.: Study on chip segmentation in machining titanium alloy. *Proceedings of the Fifth International Conference on Production Engineering*, pp. 233–239, 1984. (Cited on page 28.)

[30] Ng, E.-G.: *Modelling of the cutting process when machining hardened steel with PCBN tooling*. Master's thesis, Mechanical Engineering,University of Birmingham, 2001. (Cited on page 28.)

[31] Johnson, G.R. and Cook, W.H.: Fracture characteristics of three metals subjected to various strains, strain rates, temperatures and pressures. *Engineering Fracture Mechanics*, vol. 21, pp. 31–48, 1985. (Cited on pages 29, 30, 31, and 37.)

[32] Sun, J. and Guo, Y.B.: Material flow stress and failure in multiscale machining titanium alloy ti-6al-4v. *International Journal of Advanced Manufacturing Technology*, vol. 41, pp. 651Ű–659, 2009. (Cited on pages xiii and 29.)

[33] Shih, A.: Finite element simulation of orthogonal metal cutting. *Transactions of the ASME*, vol. 117, pp. 84–93, 1995. (Cited on pages 30 and 36.)

[34] Shih, A.: Finite-element analysis of orthogonal metal-cutting mechanics. *Int. J. Mach. Tool and Manuf.*, vol. 36, pp. 255–273, 1996a. (Cited on page 30.)

[35] Shih, A.: Finite element analysis of the rake angle effects in orthogonal metal cutting. *Int. J. Mech. Sci.*, vol. 38, pp. 1–17, 1996b. (Cited on page 30.)

[36] Shih, A., Chandrasekar, S. and Yang, H.: Finite element simulation of metal cutting process with strain-rate and temperature effects. *Fundamental Issues in Machining/ASME PED*, vol. 43, pp. 11–24, 1990. (Cited on pages 30 and 36.)

[37] Iwata, K., Osakada, K. and Terasaka, Y.: Process modelling of orthogonal cutting by the rigid plastic finite element method. *J. Engng. Ind. Trans. ASME*, vol. 106, pp. 132–138, 1984. (Cited on page 30.)

[38] Kim, K. and Sin, H.: Development of a thermoviscoplastic cutting model using finite element method. *Int. J. Mach. Tool and Manuf.*, vol. 36, pp. 379–397, 1996. (Cited on page 30.)

[39] Joshi, V., Dixit, P. and Jain, V.: Viscoplastic analysis of metal-cutting by finite-element method. *Int. J. Mach. Tool and Manuf.*, vol. 34, pp. 553–571, 1994. (Cited on page 30.)

[40] Sekhon, G. and Chenot, J.: Numerical simulation of continuous chip formation during non-steady orthogonal cutting. *Engng. Comp.*, vol. 10, pp. 31–48, 1993. (Cited on page 30.)

[41] Eldridge, K., Dillon, O. and Lu, W.: Thermo-viscoplastic finite element modelling of machining under various cutting conditions. *Trans. of NAMRI/SME*, vol. XIX, pp. 162–169, 1991. (Cited on page 30.)

[42] Altintas, Y. and Engin, S.: Generalized modelling of milling mechanics and dynamics: Part ii - inserted cutters. *International journal of machine tools and manufacture*, vol. 41, pp. 2212–2220, 2001. (Cited on page 30.)

[43] Wu, J., Dillon Jr., O.W. and Lu, W.: Thermo-viscoplastic modeling of machining process using a mixed finite element method. *J. Manuf. Sci. Engng., Trans. ASME*, vol. 118, pp. 470–428, 1996. (Cited on page 30.)

[44] Xie, J., Bayoumi, A. and Zbib, H.: Characterization of chip formation and shear banding in orthogonal machining using finite element analysis. *Material Instabilities, Theory and Applications - ASME 183/MD*, vol. 50, pp. 285–301, 1994. (Cited on page 30.)

[45] Vaz Jr., M. Owen, D. and Peric, D.: Finite-element techniques applied to high-speed machining. *Simulation of Materials Processing: Theory, Methods and Applications*, pp. 973–978, 1998a. (Cited on page 30.)

[46] Vaz Jr., M. Owen, D. and Peric, D.: Numerical simulation of high-speed machining using finite elements. *Computational Mechanics in U.K*, pp. 113–116, 1998b. (Cited on page 30.)

[47] Owen, D. and Jr., V.: Computational techniques applied to high-speed machining under adiabatic strain localization conditions. *Comp. Meth. Appl.*, 2005. (Cited on pages 30 and 36.)

[48] Obikawa, T. and Usui, E.: Computational machining of titanium alloyŮfinite element modeling and a few results. *Journal of Manufacturing Science and Engineering*, vol. 118, pp. 208–215, May 1996. (Cited on pages 30, 34, and 36.)

[49] Johnson, G.R. and Cook, W.H.: A constitutive model and data for metals subjected to large strains, high strain rates and high temperatures. *Proceeding of the 7th International Symposium on Ballistics*, vol. 7, pp. 541–547, 1983. (Cited on page 30.)

[50] Lee, W. and Lin, C.: High-temperature deformation behavior of ti6al4v alloy evaluated by high strain-rate compression tests. *J. Mater. Process. Technol*, vol. 75, pp. 127Ű–136, 1998. (Cited on page 32.)

[51] Dumitrescu, M., Elbestawi, M. and El-Wardany, T.: Mist coolant applications in high speed mmchining of advanced materials metal cutting and high speed machining. *Kluwer Academic/Plenum Publishers*, pp. 329Ű–339, 2002. (Cited on page 32.)

[52] Khan, A., Suh, Y. and Kazmi, R.: Quasi-static and dynamic loading responses and constitutive modeling of titanium alloys. *Int Journal of Plasticity*, vol. 20, pp. 2233Ű–2248, 2004. (Cited on page 32.)

[53] Lesuer, D.: Experimental investigations of material models for ti-6al-4v titanium and 2024-t3 aluminum. *U.S. Department of Transportation/Federal Aviation Administration*, vol. 31, p. 735Ű754, 2000. DTFA03Ű97Z-90007. (Cited on page 32.)

[54] Macdougall, D. and Harding, J.: A constitutive relation and failure criterion for ti-6al-4v alloy at impact rates of strain. *Mech Phys Solids*, vol. 47, pp. 1157Ű–1185, 1999. (Cited on page 32.)

[55] Nemat-Nasser, S., Guo, W., Nesterenko, V., Indrakanti, S. and Gu, Y.: Dynamic response of conventional and hot isostatically pressed ti-6al-4v alloys: experiments and modeling. *Mechanical Matererials*, vol. 33, p. 425Ű439, 2001. (Cited on page 32.)

[56] Seo, S., Min, O. and Yang, H.: Constitutive equation for ti-6al-4vat high temperatures measured using the shpb technique. *Int J Impact Eng*, vol. 31, p. 735Ű754, 2005. (Cited on page 32.)

[57] Hua, J. and Shivpuri, R.: Prediction of chip morphology and segmentation during the machining of titanium alloys. *Journal of Materials Processing Technology*, vol. 150, pp. 124–133, 2004. (Cited on pages 31 and 38.)

[58] Johnson, G. and Holmquist, T.: Test data and computational strengthen and fracture model constants for 23 materials subjected to large strain, high-strain rates, and high temperatures. *Los Alamos National laboratory*, 1989. LA-11463-MS. (Cited on page 31.)

[59] Usui, E., Shirakashi, T. and Kitagawa, T.: Analytical prediction of three dimensional cutting process: Part 3. cutting temperature and crater wear of carbide tool. *Transactions of the ASME*, vol. 100, pp. 237–243, 1978. (Cited on pages 34 and 36.)

[60] Altintas, Y. and Engin, S.: Generalized modelling of milling mechanics and dynamics: Part ii - inserted cutters. *International journal of machine tools and manufacture*, vol. 41, pp. 2212–2220, 2001. (Cited on page 34.)

[61] Yang, H., Heinstein, M. and Shih, J.: Adaptive 2d finite element simulation of metal forming process. *International Journal of Numerical Methods in Engineering*, vol. 28, pp. 1409–1428, 1989. (Cited on page 36.)

[62] Komvopoulos, K. and Erpenbeck, S.: Finite element modelling of orthogonal metal cutting. *Journal of Industrial Engineering Transaction of the ASME*, vol. 113, pp. 253–267, 1991. (Cited on page 36.)

[63] Johnson, G.R.: Strength and fracture characteristics of a titanium alloy (.06al, .04v) subjected to various strains, strain rates, temperatures and pressure. *Naval Surface Weapons Center NSWC*, pp. 86Ű–144, 1985. (Cited on pages xiii and 37.)

[64] Hillerborg, A., Modeer, M. and Petersson, P.E.: Analysis of crack formation and crack growth in concrete by means of fracture mechanics and finite elements. *Cement and Concrete Research*, vol. 6, pp. 773Ű–782, 1976. (Cited on page 40.)

[65] J., S. and C.R., L.: On predicting chip morphology and phase transformation in hard machining. *Int J Adv Manuf Technol*, vol. 27, pp. 645Ű–654, 2005. (Cited on pages 42 and 43.)

[66] Umbrello, D.: Finite element simulation of conventional and high speed machining of ti6al4v alloy. *Journal of Materials Processing Technology*, vol. 196, pp. 3675–3694, 2008. (Cited on pages xiii and 43.)

[67] Köenig, W., Berktold, A. and Koch, K.: Turning versus grinding Ű a comparison of surface integrity aspects and attainable accuracies. *Annals of the CIRP*, vol. 42, pp. 39–43, 1993. (Cited on page 43.)

[68] Budak, E., Altintas, Y. and Armarego, E.: Prediction of milling force coefficients from orthogonal cutting data. *Transactions of the ASME*, vol. 118, pp. 216–224, 1996. (Cited on pages 64 and 67.)

[69] Altintas, Y. and Lee, P.: Prediction of ball-end milling forces from orthogonal cutting data. *Mach tool manufacturing*, vol. 36, no. 9, pp. 1059–1072, April 1995. (Cited on pages x, xi, 2, 64, 65, 70, 71, 78, and 79.)

[70] Montgomery, D. and Altintas, Y.: Mechanism of cutting force and surface generation in dynamic milling. *Trans. ASME J. Engng Ind.*, vol. 113, pp. 160–168, 1991. (Cited on page 72.)

Appendix A

Turning test data

Table A.1: Machining forces for: $v = 15m/min$, $rake = 0°$

Feed $[mm/rev]$	Cutting force	Feed force
0.005	30.09952911	40.13270548
0.025	74.41272474	62.70735231
0.05	118.7259204	80.26541096
0.1	201.1524086	114.3648775
0.2	334.1725498	154.9197986
0.3	437.9429768	180.3788123

Table A.2: Machining forces for: $v = 40m/min$, $rake = 0°$

Feed $[mm/rev]$	Cutting force	Feed force
0.005	26.06483541	37.35959742
0.025	64.29326068	58.21146575
0.05	109.7552083	73.45833333
0.1	184.1915036	98.17754671
0.2	314.7061877	138.6978301
0.3	437.9429768	180.3788123

Table A.3: Machining forces for: $v = 75m/min$, $rake = 0°$

Feed $[mm/rev]$	Cutting force	Feed force
0.005	25.19600756	37.09725311
0.025	61.68677714	54.73615436
0.05	99.64412811	69.39501779
0.1	183.9302682	94.85193201
0.2	308.079838	143.016767
0.3	437.7104	193.6027

Table A.4: Machining forces for: $v = 125m/min$, $rake = 0°$

Feed $[mm/rev]$	Cutting force	Feed force
0.005	24.74398226	38.76557221
0.025	65.9839527	56.91115921
0.05	108.692744	72.74052868
0.1	186.2516108	103.2149377
0.2	338.9830508	152.5423729
0.3	437.7104	193.6027

Table A.5: Machining forces for: $v = 200m/min$, $rake = 0°$

Feed $[mm/rev]$	Cutting force	Feed force
0.005	25.56878167	36.29117399
0.025	61.87125428	59.36296019
0.05	118.294942	91.44786297
0.1	180.0000	112.6169996
0.2	338.9830508	152.5423729
0.3	437.7104	193.6027

Table A.6: Machining forces for: $v = 15m/min$, $rake = 5°$

Feed $[mm/rev]$	Cutting force	Feed force
0.005	36.62109375	58.59375
0.025	76.49739583	69.17317708
0.05	112.3046875	74.05598958
0.1	188.8020833	96.84244792
0.2	330.4036458	146.484375
0.3	409.3424479	173.3398438

Table A.7: Machining forces for: $v = 40m/min$, $rake = 5°$

Feed $[mm/rev]$	Cutting force	Feed force
0.005	33.36588542	57.77994792
0.025	69.17317708	68.359375
0.05	107.421875	78.125
0.1	184.7330729	104.9804688
0.2	297.8515625	137.5325521
0.3	409.3424479	173.3398438

Table A.8: Machining forces for: $v = 75m/min$, $rake = 5°$

Feed $[mm/rev]$	Cutting force	Feed force
0.005	29.7934322	48.828125
0.025	65.10416667	61.03515625
0.05	104.9804688	71.61458333
0.1	178.2226563	88.70442708
0.2	291.3411458	130.2083333
0.3	411.7838542	192.8710938

Table A.9: Machining forces for:$v = 125m/min$, $rake = 5°$

Feed $[mm/rev]$	Cutting force	Feed force
0.005	27.66927083	49.64192708
0.025	65.10416667	58.59375
0.05	106.6080729	72.42838542
0.1	177.4088542	94.40104167
0.2	289.7135417	138.3463542
0.3	411.7838542	192.8710938

Table A.10: Machining forces for: $v = 200m/min$, $rake = 5°$

Feed $[mm/rev]$	Cutting force	Feed force
0.005	25.22786458	43.9453125
0.025	65.91796875	62.66276042
0.05	106.6080729	76.49739583
0.1	166.8294271	96.84244792
0.2	289.7135417	138.3463542
0.3	411.7838542	192.8710938

A.1 Machining temperatures

Table A.11: Measured machining temperatures

Cutting speed m/min	temp [C°] $feed = 0.05mm/rev$	temp [C°] $feed = 0.1mm/rev$
7.5	170	166
15	401	403
40	583	585
75	645	641
125	695	702
200	822	821
300	842	845

A.2 Chip microscopy

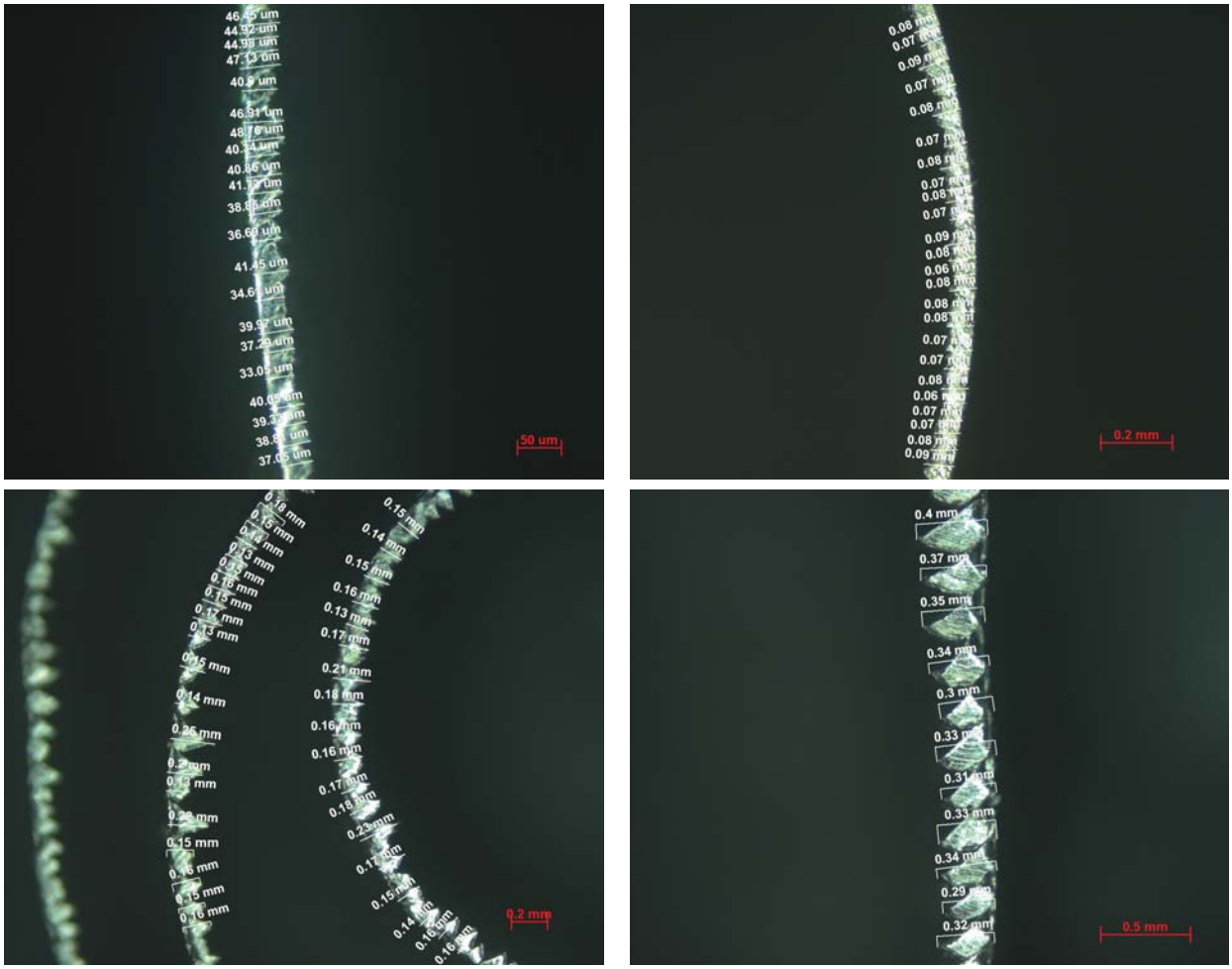

Figure A.1: Chip images from optical microscopy. $V = 40$ m/min, $feed = 0.025; 0.05; 0.1; 0.2$ mm and $rake = 5^\circ$

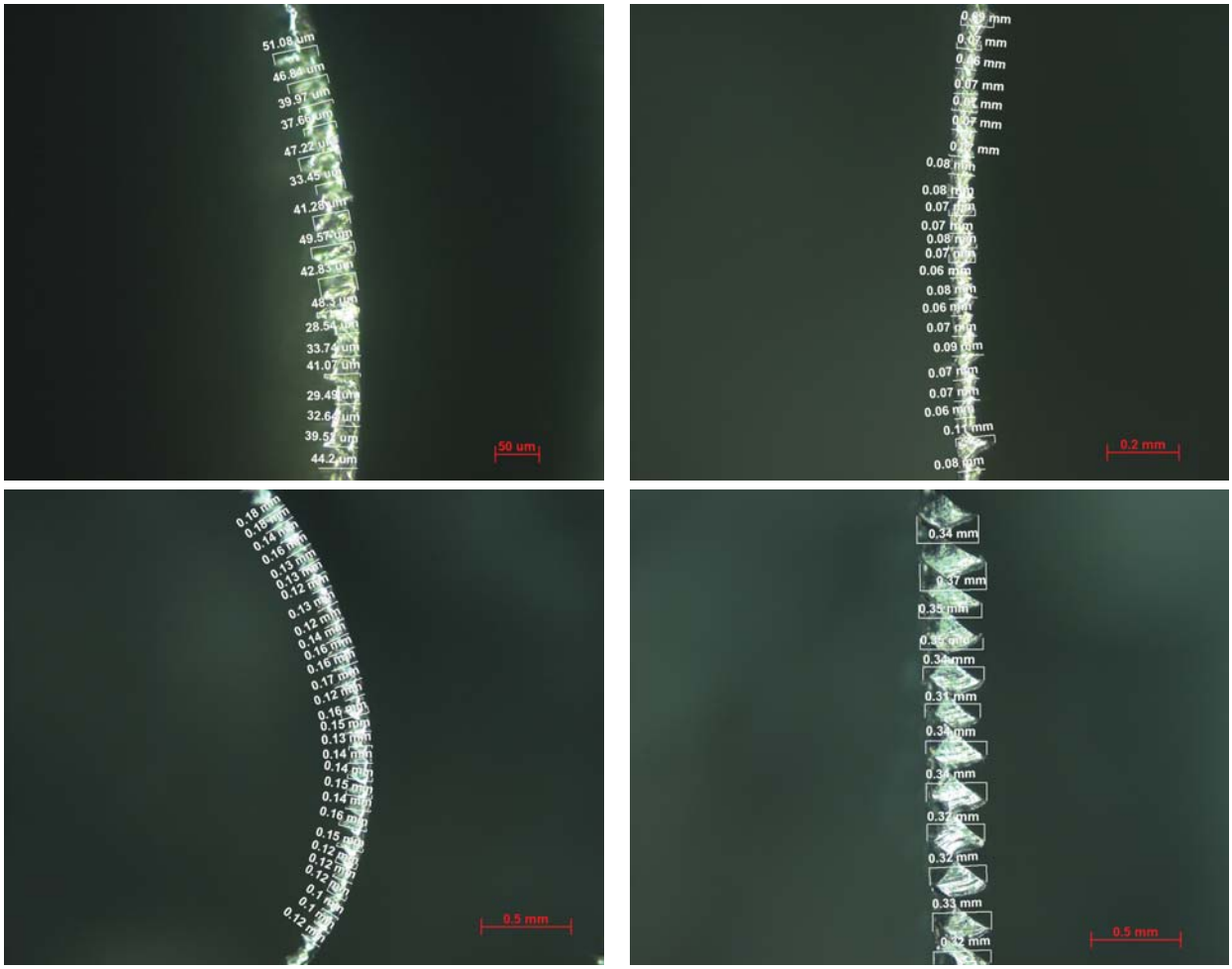

Figure A.2: Chip images from optical microscopy. $V = 75$ m/min, $feed = 0.025; 0.05; 0.1; 0.2$ mm and $rake = 5°$

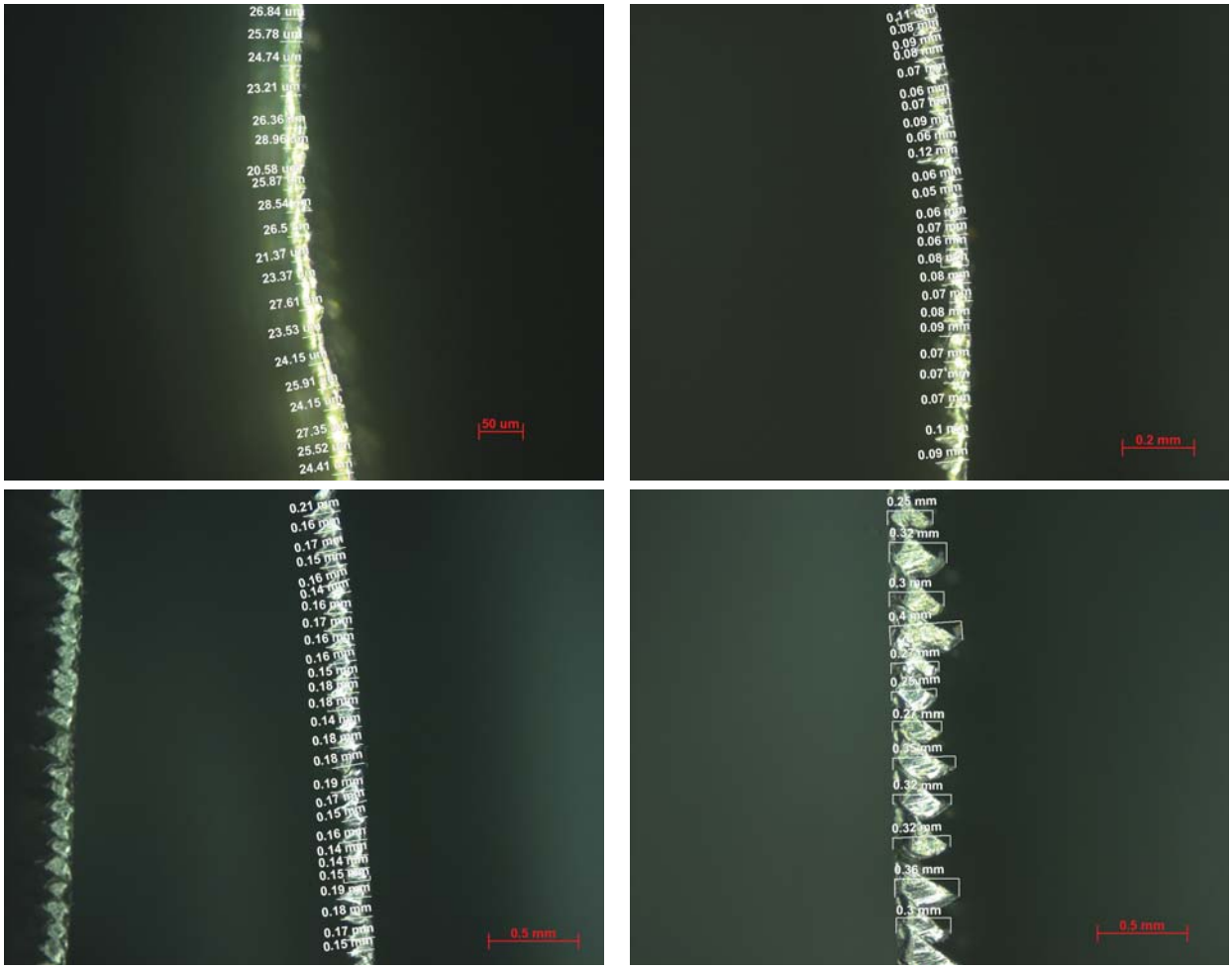

Figure A.3: Chip images from optical microscopy. $V = 125$ m/min, $feed = 0.025; 0.05; 0.1; 0.2$ mm and $rake = 5°$

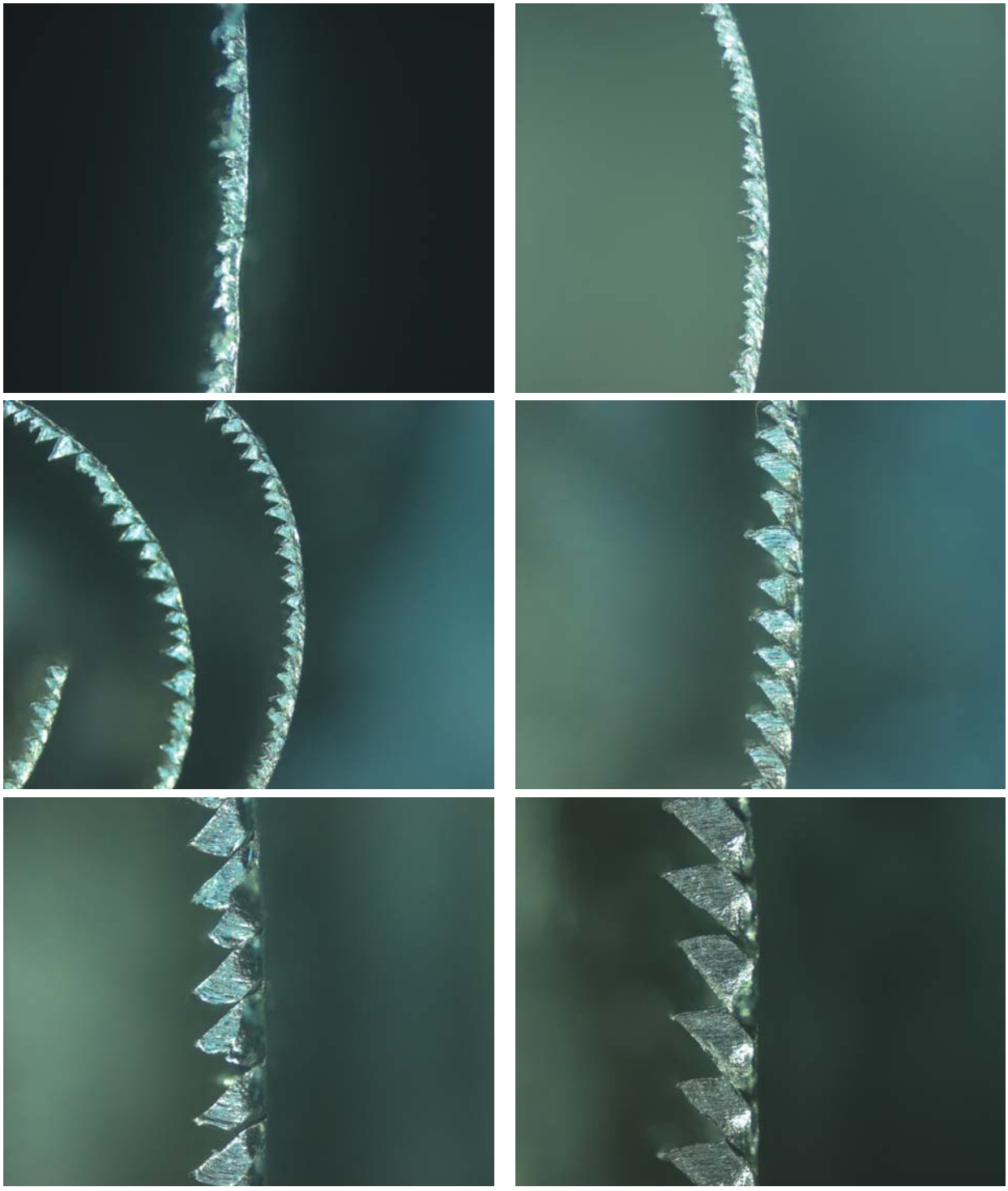

Figure A.4: Chip images from optical microscopy (unannotated). $V = 40$ m/min, $feed = 0.025; 0.05; 0.1; 0.2; 0.3; 0.4$ mm and $rake = 0°$

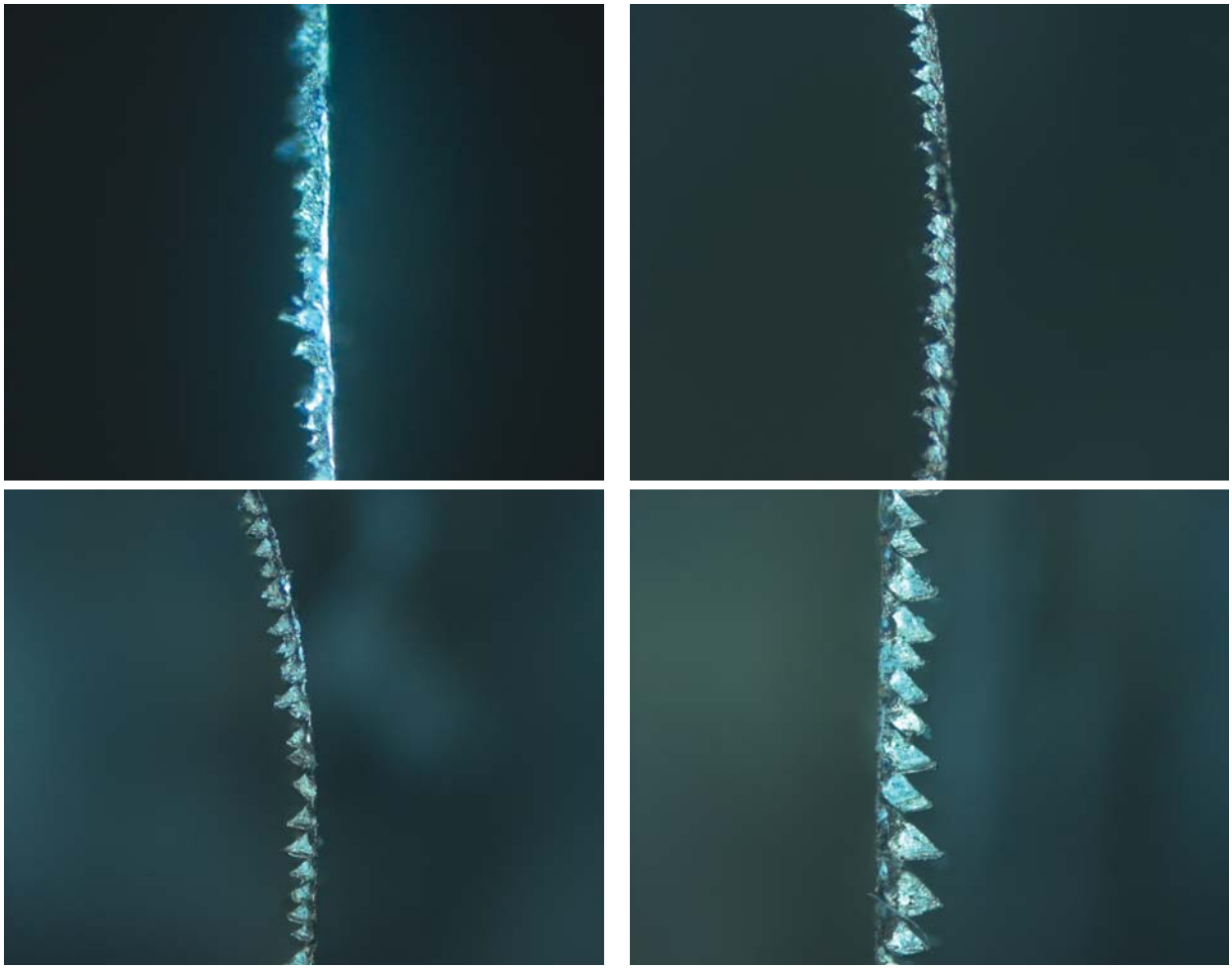

Figure A.5: Chip images from optical microscopy (unannotated). $V = 75$ m/min, $feed = 0.025; 0.05; 0.1; 0.2$ mm and $rake = 5°$

Appendix B

Finite element results

B.1 Finite element predictions for varying feed rates

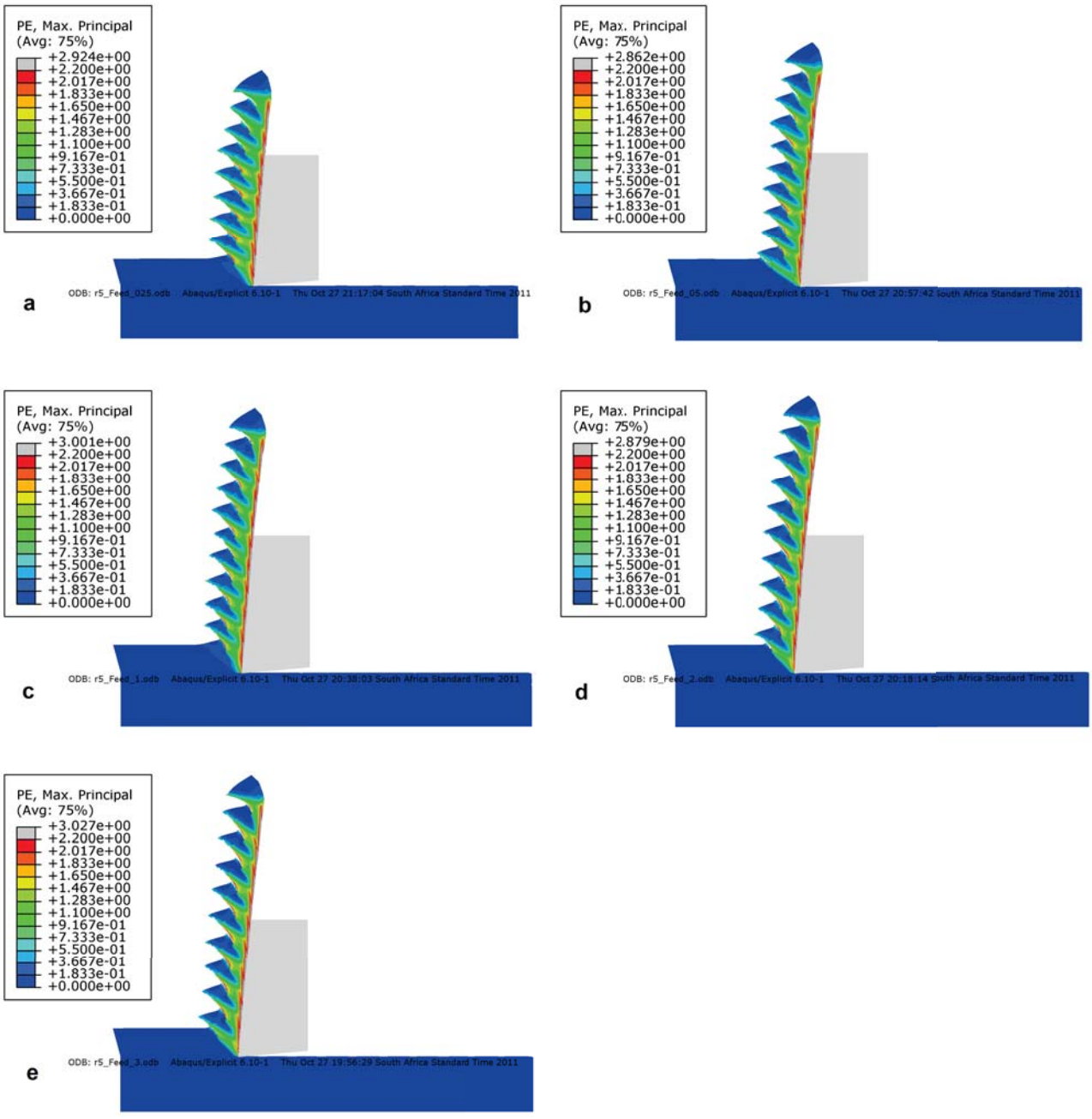

Figure B.1: FE prediction of plastic strain distribution in the chip with $v = 75$ m/min and $feed = 0.025; 0.5; 0.1; 0.2; 0.3$ mm (image a-e)

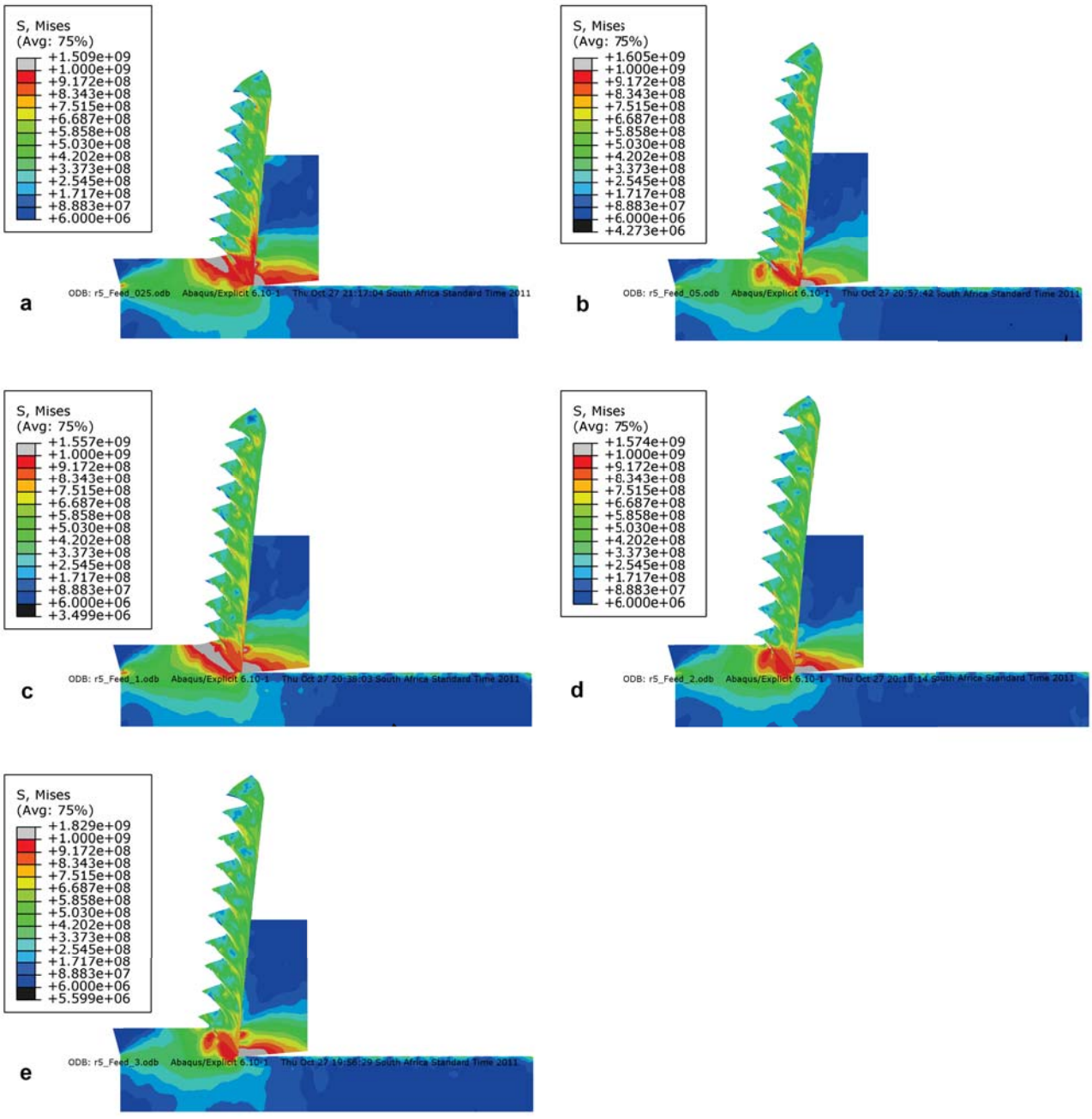

Figure B.2: FE prediction of Mises stress distribution in the chip with $v = 75$ m/min and $feed = 0.025; 0.5; 0.1; 0.2; 0.3$ mm (image a-e)

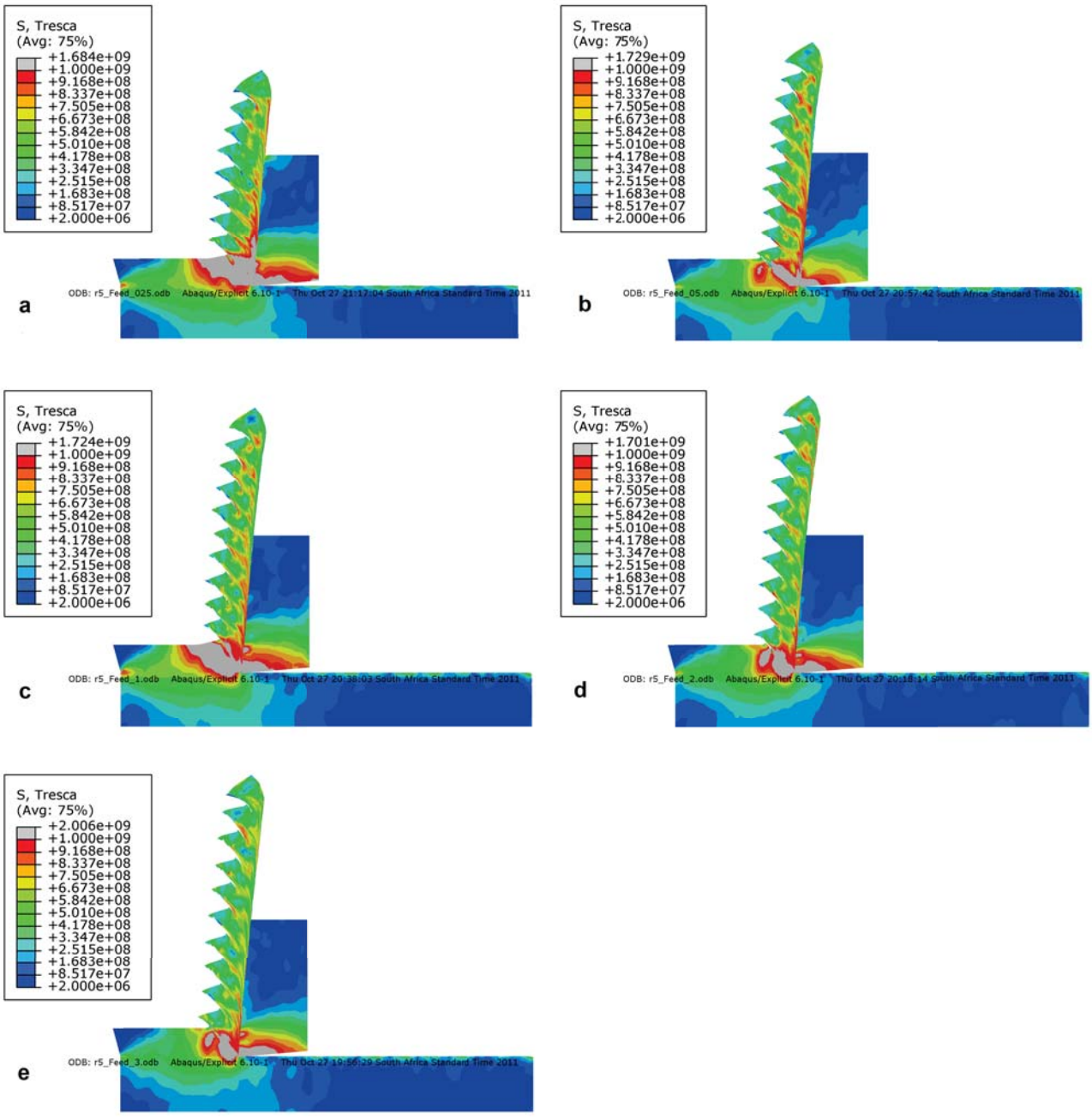

Figure B.3: FE prediction of Tresca stress distribution in the chip with $v = 75$ m/min and $feed = 0.025; 0.5; 0.1; 0.2; 0.3$ mm (image a-e)

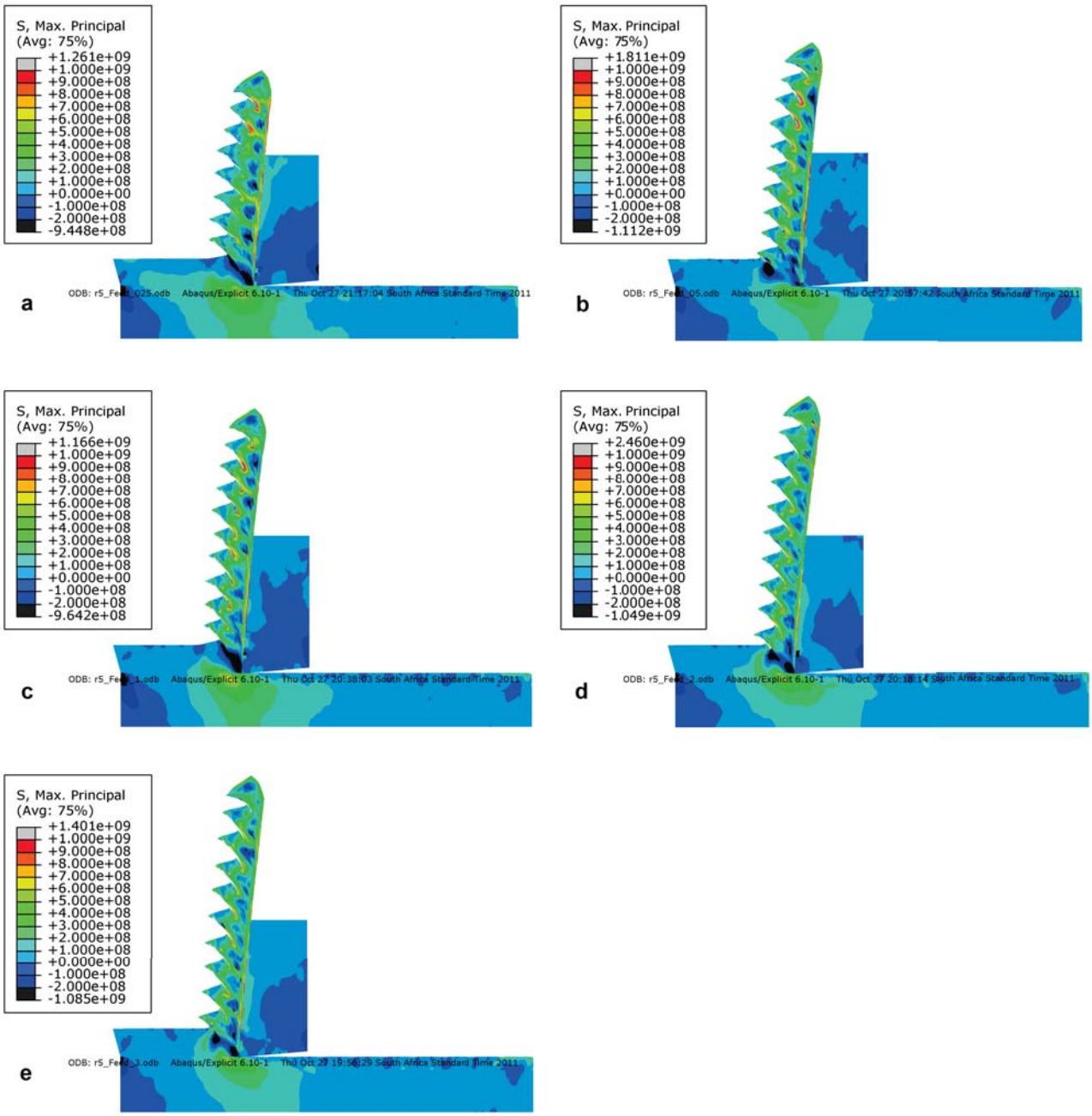

Figure B.4: FE prediction of max principle stress distribution in the chip with $v = 75$ m/min and $feed = 0.025; 0.5; 0.1; 0.2; 0.3$ mm (image a-e)

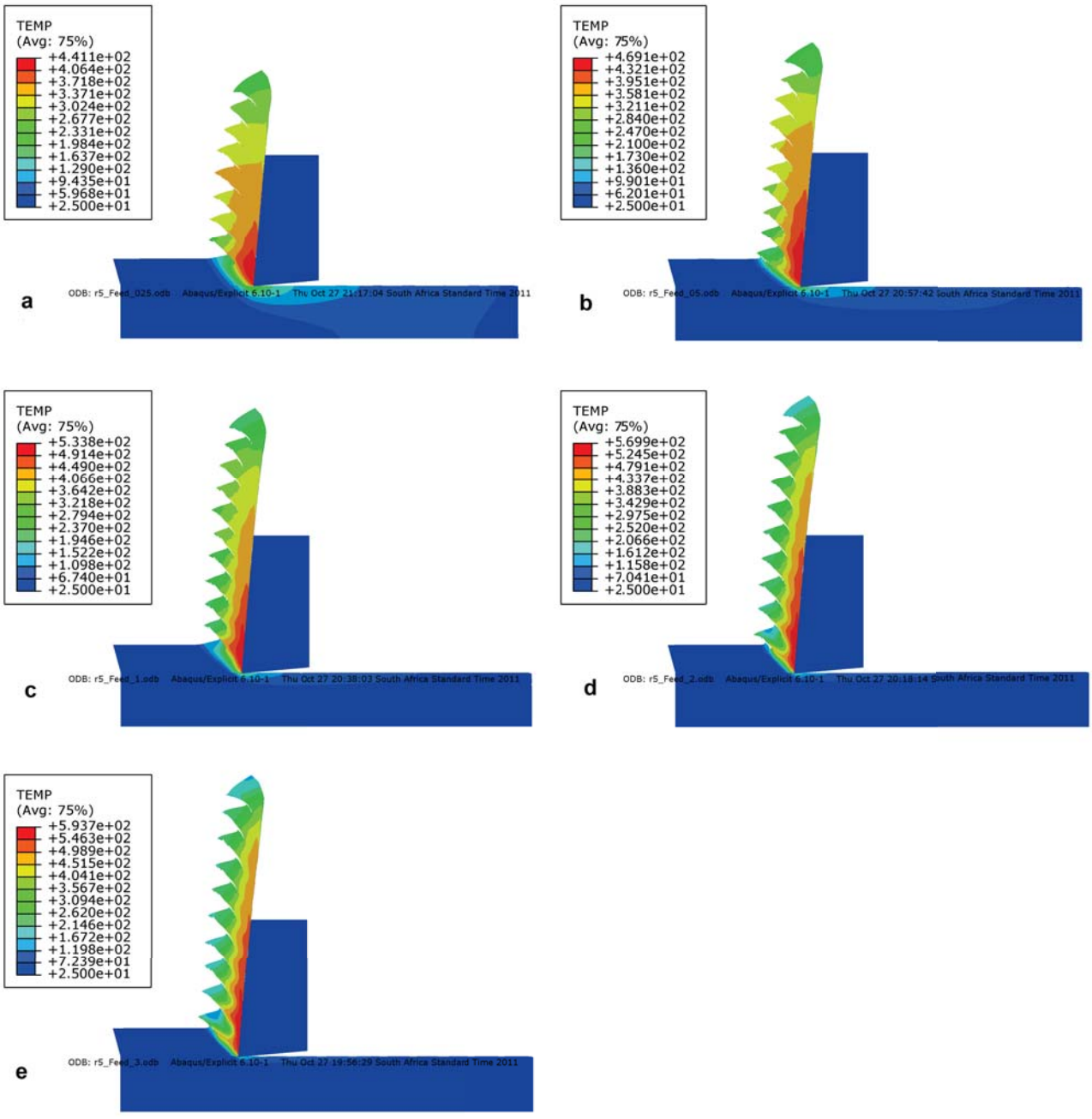

Figure B.5: FE prediction of plastic strain distribution in the chip with $v = 75$ m/min and $feed = 0.025; 0.5; 0.1; 0.2; 0.3$ mm (image a-e)

B.2 Finite element predictions for varying cutting speed

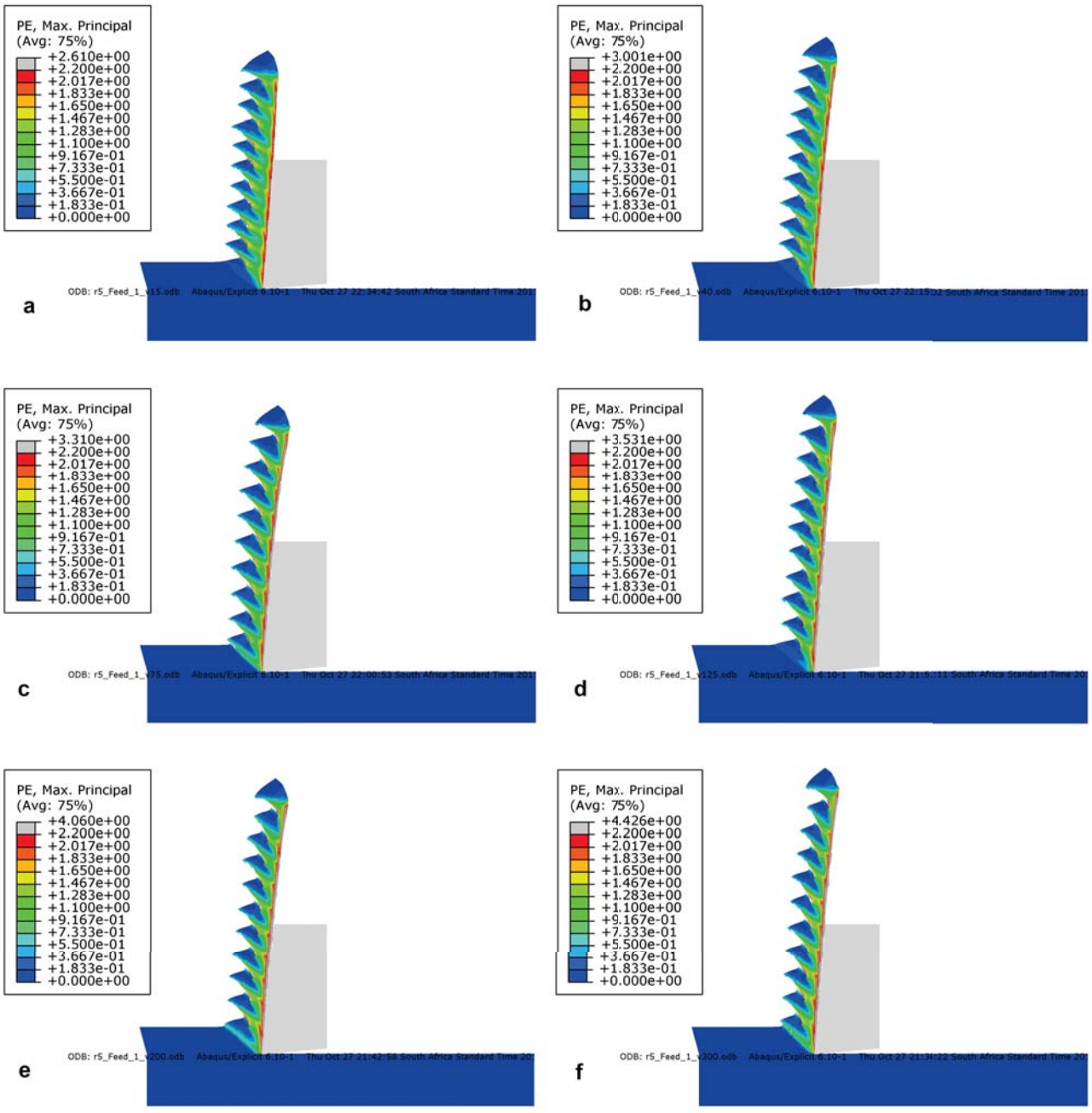

Figure B.6: FE prediction of plastic strain distribution in the chip with $feed = 0.025$ mm/rev and $v = 15; 45; 75; 125; 200; 300$ m/min (image a-f)

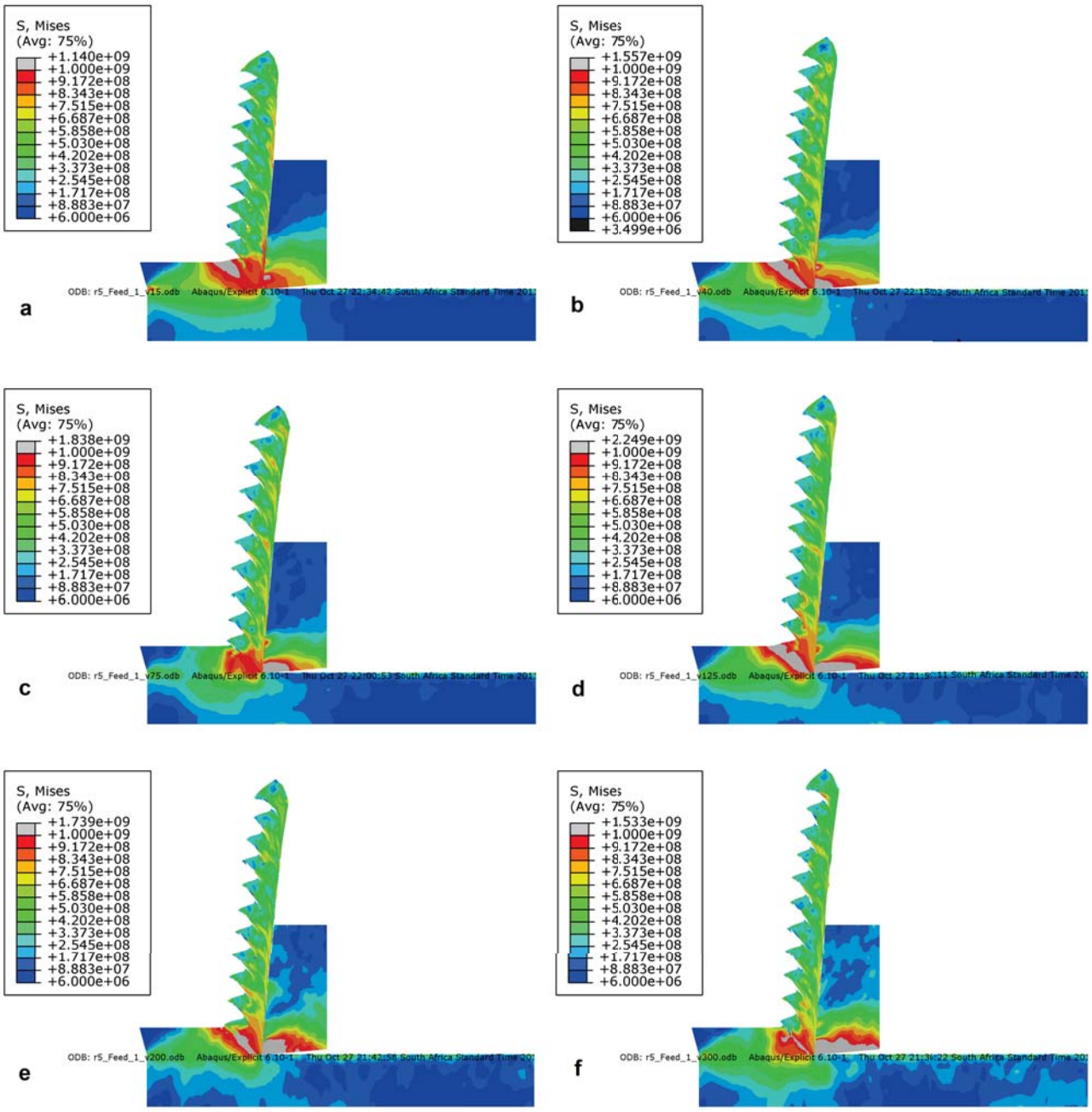

Figure B.7: FE prediction of Mises stress distribution in the chip with $feed = 0.025$ mm/rev and $v = 15; 45; 75; 125; 200; 300$ m/min (image a-f)

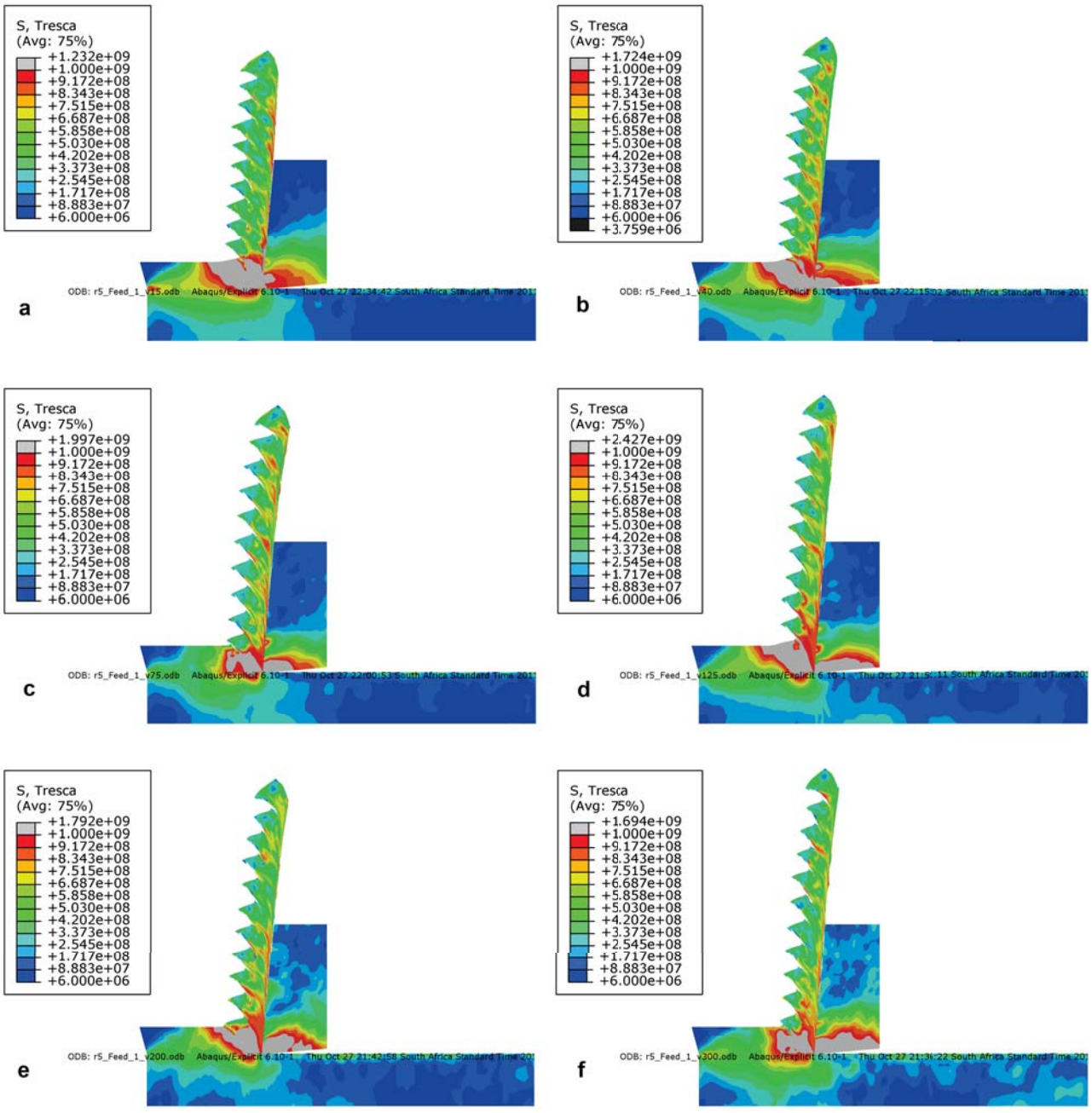

Figure B.8: FE prediction of Tresca stress distribution in the chip with $feed = 0.025$ mm/rev and $v = 15; 45; 75; 125; 200; 300$ m/min (image a-f)

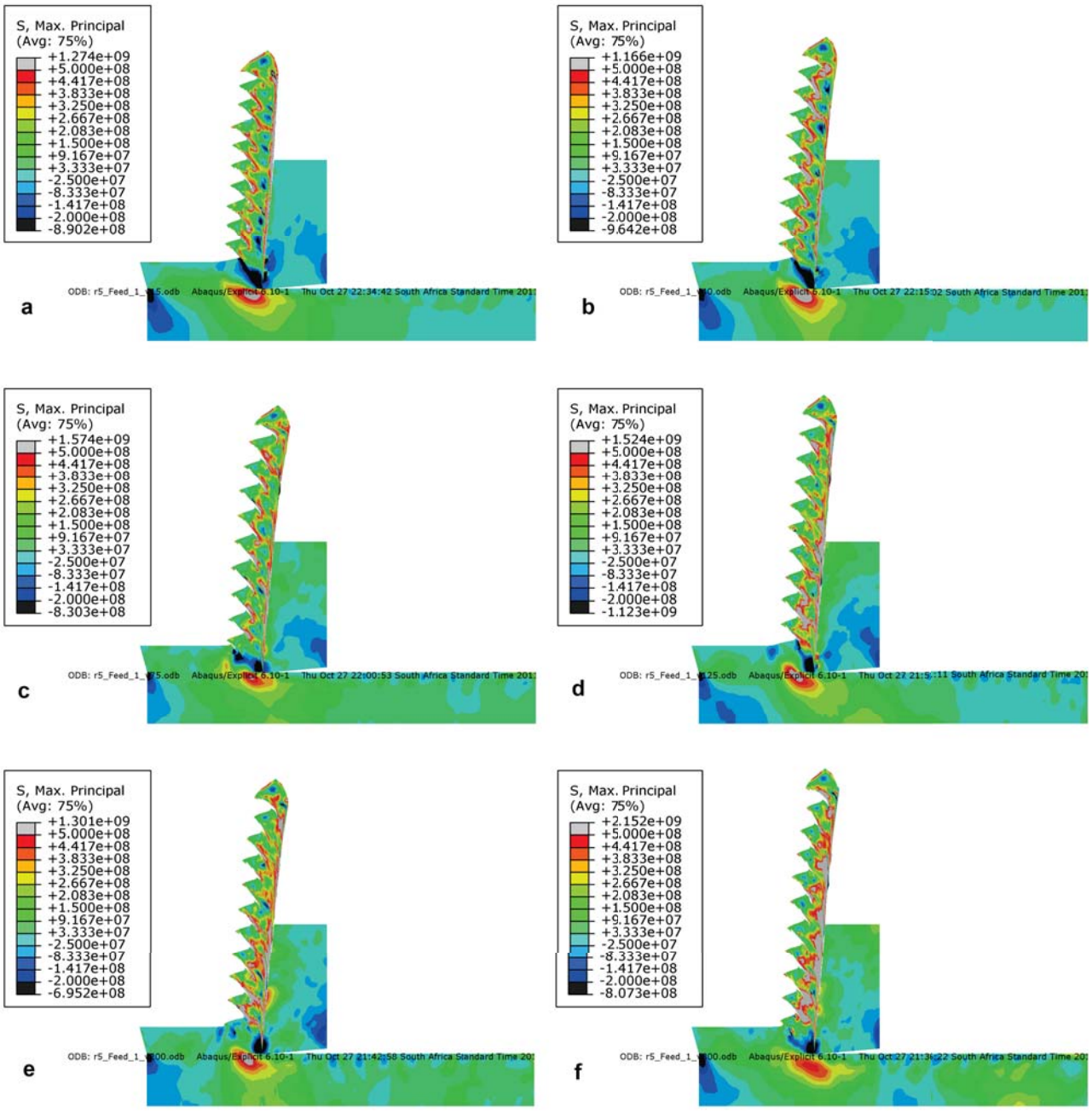

Figure B.9: FE prediction of max principle stress distribution in the chip with $feed = 0.025$ mm/rev and $v = 15; 45; 75; 125; 200; 300$ m/min (image a-f)

Appendix C

Matlab FE cutting model builder for Abaqus Explicit solver

C.1 Input file builder

```
%clear all;close all
%This program generates the Abaqus input file for an orthogonal machining
%model
tic

fid = fopen('feed1_v75_mesh20_cr20_08.inp','w');
%define cutting speed feed and friction coefficient
feed = 0.1e-3; %m
Vc = 75;       %m/min
friction = 0.3


%work piece geometry and number of elements
h_chip=feed;     %chip height      (y)
l_w=h_chip*10;   %workpiece length (x)
h_w=h_chip*2;    %workpiece height (y)

dist_ang=0/180*pi           %mesh predistortion angle
ney_chip = 20;              %number of el in y direction (chip)
ney_work = 0.75*ney_chip;   %number of el in y direction (workpiece)
ney=ney_chip+ney_work
l_y=h_chip/ney_chip
nex  = round(l_w/l_y)
l_x=l_w/nex

disp_length_chip = l_x*1.5/cos(dist_ang)*0.8
disp_length_cl = l_x*2*0.8
thick = l_w/nex             %plane strain thickness

%tool geometry
l_t = h_chip*2.5;      %tool length
h_t = h_chip*5;        %tool height
r_ang = 0;       %rake angle
c_ang = 5;      %clearance angle
nex_tool = 20;  %number of el in x direction
ney_tool = 30; %number of el in y direction


V = Vc/60;
time = l_w/V*2/3*1.2;
V=-V;
```

```
%element height
sh_e = h_chip/50;    %y length of shear failure element
% ************************************************************************
% Material properties for TiAl4V
% ************************************************************************
density = 4430; %kg/m^3
E = 110e+9; %Pa
poisson = 0.3;

% % JC plastic flow constants
% sigma_flow = (A + B*(E_pl)^n) * (1 + C*ln(E_d_pl/E_d_0)) * (1-T)^m
% T = (t-t_tr/t_melt-t_tr)
% No. A (MPa) B (MPa) n     C          m References
% 1 782.7    498.4    0.28    0.028      1 [34]
% 2 870      990      0.25    0.011      1 [35]
% 3 724      683.1    0.47    0.035      1 [36]
% 4 968      380      0.421   0.0197     0.577 [14]
% 5 859      640      0.22    0.000022   1.1 [37]
% 6 862      331      0.34    0.012      0.8 [38]
A = 862e6
B = 331e6
N = 0.34
C = 0.012
m = 0.8
T_m =1650
T = 25
% JC shear failure criteria for crack propagation and chip separation
% E_pl = (d_1 + d_2exp(d_3*p/q))(1 + d_4*ln(E_d_pl/E_d_0))*(1+d_5*T)
D_1 = -0.09
D_2 = 0.25
D_3 = 0.5
D_4 = 0.014
D_5 = 3.87

% ************************************************************************
% Material properties for WC
% ************************************************************************
% density = 4430; %kg/m^3
% E = 110e+9; %Pa
% poisson = 0.3;
%************************************************************************
%mesh CHIP
[nodes_chip,joints_chip]= chip_mesher_distort(nex,ney_chip,l_w,h_w,h_chip,dist_ang);

%************************************************************************

%mesh SHEAR PLANE
[nodes_sh,joints_sh]= shear_mesher_distort(nex,ney_chip,l_w,h_w,h_chip,sh_e,dist_ang↩
    );
s = size(joints_chip);
nnodes = s(1,1);
ss = size(nodes_chip);
nel = ss(1,1);

nodes_upd_sh = [nodes_sh(:,1)+nel,nodes_sh(:,2:5)+(nex+1)*(ney_chip)];
n = [nodes_chip;nodes_upd_sh];
joints_upd_sh = [joints_sh(:,1)+nnodes,joints_sh(:,2:4)];
j = [joints_chip;joints_upd_sh];

% %************************************************************************
%mesh WORKPIECE
[nodes_work,joints_work]= work_mesher_graded(nex,ney_work,l_w,h_w,h_chip,sh_e,↩
    dist_ang);

ss = size(j);
nnodes = ss(1,1);
s = size(n);
nel = s(1,1);

nodes_upd_work = [nodes_work(:,1)+nel,nodes_work(:,2:5)+(nex+1)*(ney_chip+1)];
n = [n;nodes_upd_work];
```

```
joints_upd_work = [joints_work(:,1)+(nex+1)*(ney_chip+2),joints_work(:,2:4)];
j = [j;joints_upd_work];

j((nex+1)*(ney_chip)+1,3) =j((nex+1)*(ney_chip)+1,3);%+sh_e;
j((nex+1)*(ney_chip+1)+1,3) =j((nex+1)*(ney_chip+1)+1,3)-1*sh_e;

joints_work_b(:,1) = j(:,1)+length(j);
joints_work_b(:,2) = j(:,2);
joints_work_b(:,3) = j(:,3);
joints_work_b(:,4) = j(:,4)+thick;
j(length(j)+1:2*length(j),:) = joints_work_b;

n(:,6:9) = n(:,2:5)+length(j)/2;
plotter(n,j);
hold on

%*************************************************************************
%mesh TOOL
[nodes_tool,joints_tool]= tool_mesher_graded(nex_tool,ney_tool,l_t,h_t,l_w,r_ang,↩
    c_ang,h_chip,sh_e,dist_ang);
jt=joints_tool(:,2:4);

wide = 0.1;
joints_tool(:,2:4)=jt;
joints_tool(:,4)=joints_tool(:,4)-(thick*wide);
plotter_red(nodes_tool,joints_tool);
grid on
plotter_black(nodes_chip,joints_chip);
joints_tool_b(:,1) = joints_tool(:,1)+length(joints_tool);
joints_tool_b(:,2) = joints_tool(:,2);
joints_tool_b(:,3) = joints_tool(:,3);
joints_tool_b(:,4) = joints_tool(:,4)+thick+2*(thick*wide);
joints_tool(length(joints_tool)+1:2*length(joints_tool),:) = joints_tool_b;

nodes_tool(:,6:9) = nodes_tool(:,2:5)+length(joints_tool)/2;

% ************************************************
nnodes_w = length(j);
nnodes_t = length(joints_tool);
nnodes = length(joints_tool)+length(j);

%Write ABAQUS input file (.inp)
% ************************************************
%define assembly instances
% ************************************************
fprintf(fid,'%6s\n%6s\n','*Heading','** Job name: UL_my_model Model name: Model-1');
fprintf(fid,'%6s\n','** Generated by: Abaqus/CAE Version 6.8-1');
fprintf(fid,'%6s\n','*Preprint, echo=NO, model=NO, history=NO, contact=NO');
fprintf(fid,'%6s\n','** PARTS');
fprintf(fid,'%6s\n','*Part, name=Tool');
fprintf(fid,'%6s\n','*End Part');
fprintf(fid,'%6s\n','*Part, name=Workpiece');
fprintf(fid,'%6s\n','*End Part');
fprintf(fid,'%6s\n','*Assembly, name=Assembly');
fprintf(fid,'%6s\n','*Instance, name=Tool-1, part=Tool');
fprintf(fid,'%-6s\n','*Node');
fprintf(fid,'%6.0f , %12.11f , %12.11f ,%12.11f\n',joints_tool');
fprintf(fid,'%6s\n','*Element, type=C3D8RT');
fprintf(fid,'%6.0f , %6.0f ,%6.0f,%6.0f,%6.0f,%6.0f,%6.0f ,%6.0f , %6.0f\n',↩
    nodes_tool');
fprintf(fid,'%6s\n','*Elset, elset=_PickedSet2, internal, generate');
fprintf(fid,'%6.0f,%6.0f,%6.f\n',1,length(nodes_tool),1);
fprintf(fid,'%6s\n','** Section: Tool');
fprintf(fid,'%6s\n','*Solid Section, elset=_PickedSet2, material=WC');
fprintf(fid,'%6.0f,\n',1.0);
fprintf(fid,'%6s\n','*End Instance');
fprintf(fid,'%6s\n','*Instance, name=Workpiece-1, part=Workpiece');
fprintf(fid,'%-6s\n','*Node');
fprintf(fid,'%6.0f , %12.11f , %12.11f ,%12.11f\n',j');
fprintf(fid,'%6s\n','*Element, type=C3D8RT');
fprintf(fid,'%6.0f , %6.0f ,%6.0f ,%6.0f ,%6.0f ,%6.0f ,%6.0f ,%6.0f , %6.0f\n',n');
```

```
fprintf(fid,'%6s\n','** Region: (Workpiece_Body:Picked)');
fprintf(fid,'%6s\n','*Elset, elset=Body, internal');
fprintf(fid,'%6.0f,\n',nodes_upd_work(:,1));
fprintf(fid,'%6.0f,\n',nodes_chip(:,1));
fprintf(fid,'%6s\n','*Elset, elset=CL, internal');
fprintf(fid,'%6.0f,\n',nodes_upd_sh(:,1));
fprintf(fid,'%6s\n','*Elset, elset=chip, internal');
fprintf(fid,'%6.0f,\n',nodes_chip(1:(nex)*(crl)));
fprintf(fid,'%6s\n','** Section: Workpiece');
fprintf(fid,'%6s\n','*Solid Section, elset=Body, material=Ti6Al4V');
fprintf(fid,'%6.0f,\n',1);
fprintf(fid,'%6s\n','*Solid Section, elset=CL, material=Ti6Al4V_CL');
fprintf(fid,'%6.0f,\n',1);
fprintf(fid,'%6s\n','*Solid Section, elset=chip,controls=ec, material=Ti6Al4V_chip')↩
    ;
fprintf(fid,'%6.0f,\n',1);
fprintf(fid,'%6s\n','*End Instance');

%definition of element, node and surface sets
%**********************************************************************
fprintf(fid,'%6s\n','*nset, nset=Tool_top_nodes, internal, instance=Tool-1');
fprintf(fid,'%6.0f,\n',(nex_tool+1)*(ney_tool)+1:1:(nex_tool+1)*(ney_tool)+1+↩
    nex_tool,(nex_tool+1)*(ney_tool)+1+nnodes_t/2:1:(nex_tool+1)*(ney_tool)+1+↩
    nex_tool+nnodes_t/2);
fprintf(fid,'%6s\n','*elset, elset=Tool_top, internal, instance=Tool-1');
fprintf(fid,'%6.0f,\n',(nex_tool)*(ney_tool)-nex_tool+1:1:(nex_tool)*(ney_tool));
fprintf(fid,'%6s\n','*****************************************');
fprintf(fid,'%6s\n','*elset, elset=tool_all, internal, instance=Tool-1');
fprintf(fid,'%6.0f,\n',1:length(joints_tool));
fprintf(fid,'%6s\n','*****************************************');
fprintf(fid,'%6s\n','*nset, nset=Tool_back, internal, instance=Tool-1');
fprintf(fid,'%6.0f,\n',1+nex_tool:(nex_tool+1):(nex_tool+1)*(ney_tool+1)+nex_tool,1+↩
    nex_tool+nnodes_t/2:(nex_tool+1):(nex_tool+1)*(ney_tool+1)+nex_tool+nnodes_t/2);
fprintf(fid,'%6s\n','*****************************************');
fprintf(fid,'%6s\n','*SURFACE, NAME=tool_excl, TYPE=ELEMENT ');
fprintf(fid,'%6s\n','tool_all,');
fprintf(fid,'%6s\n','*****************************************');
fprintf(fid,'%6s\n','*SURFACE, NAME=tool_surf, TYPE=ELEMENT ');
fprintf(fid,'%6s\n','tool_all,');
fprintf(fid,'%6s\n','*****************************************');
fprintf(fid,'%6s\n','*nset, nset=all_tool, internal, instance=Tool-1');
fprintf(fid,'%6.0f,\n',1:nnodes_t);
fprintf(fid,'%6s\n','*****************************************');
fprintf(fid,'%6s\n','*Elset, elset=Flankface, internal, instance=Tool-1');
fprintf(fid,'%6.0f,\n',1:1:nex_tool);
fprintf(fid,'%6s\n','*Surface, type=ELEMENT, name=FF, internal');
fprintf(fid,'%6s\n','Flankface, S3');
fprintf(fid,'%6s\n','*****************************************');
fprintf(fid,'%6s\n','*Elset, elset=Rakeface, internal, instance=Tool-1');
fprintf(fid,'%6.0f,\n',1:nex_tool:nex_tool*ney_tool);
fprintf(fid,'%6s\n','*Surface, type=ELEMENT, name=RF, internal');
fprintf(fid,'%6s\n','Rakeface,S6');
fprintf(fid,'%6s\n','*****************************************');
fprintf(fid,'%6s\n','*Surface, type=ELEMENT, name=Top, internal');
fprintf(fid,'%6s\n','Tool_top,S5');
fprintf(fid,'%6s\n','*****************************************');
fprintf(fid,'%6s\n','*Elset, elset=Machsurf, internal, instance=Workpiece-1');
fprintf(fid,'%6.0f,\n',nex*(ney_chip+1)+1:1:nex*(ney_chip+2));
fprintf(fid,'%6s\n','*Surface, type=ELEMENT, name=MS, internal');
fprintf(fid,'%6s\n','Machsurf, S3');
fprintf(fid,'%6s\n','↩
    **********************************************************************');
fprintf(fid,'%6s\n','*Elset, elset=Chipfront, internal, instance=Workpiece-1');
fprintf(fid,'%6.0f,\n',1:nex:(nex)*(ney_chip));
fprintf(fid,'%6s\n','*Surface, type=ELEMENT, name=CF, internal');
fprintf(fid,'%6s\n','Chipfront, S6');
fprintf(fid,'%6s\n','*****************************************');
fprintf(fid,'%6s\n','*Elset, elset=Chipunder, internal, instance=Workpiece-1');
fprintf(fid,'%6.0f,\n',nex*ney_chip-nex+1:1:nex*ney_chip);
fprintf(fid,'%6s\n','*Surface, type=ELEMENT, name=CU, internal');
fprintf(fid,'%6s\n','Chipunder, S5');
```

```
fprintf(fid,'%6s\n','↩
    ******************************************************************************');
fprintf(fid,'%6s\n','*nset, nset=all_work, internal, instance=Workpiece-1');
fprintf(fid,'%6.0f,\n',1:nnodes_w);
fprintf(fid,'%6s\n','*********************************************');
fprintf(fid,'%6s\n','*nset, nset=Work_bottom, internal, instance=Workpiece-1');
fprintf(fid,'%6.0f,\n',[(nex+1)*(ney_chip+ney_work+1)+1:1:(nex+1)*(ney_chip+ney_work↩
    +2),(nex+1)*(ney_chip+ney_work+1)+1+nnodes_w/2:1:(nex+1)*(ney_chip+ney_work+2)+ ↩
    nnodes_w/2,(nex+1)*(ney_chip+2):(nex+1):(nex+1)*(ney+1),(nex+1)*(ney_chip+2)+↩
    nnodes_w/2:(nex+1):(nex+1)*(ney+1)+nnodes_w/2]);
fprintf(fid,'%6s\n','*********************************************');
fprintf(fid,'%6s\n','*elset, elset=work_ent, internal, instance=Workpiece-1');
ex1 = ((nex)*(ney_chip+1)+1):((nex)*(ney_chip+3));
fprintf(fid,'%3.0f\n',ex1);
fprintf(fid,'%6s\n','*********************************************');
fprintf(fid,'%6s\n','*SURFACE, NAME=entry, TYPE=ELEMENT ');
fprintf(fid,'%6s\n','work_ent');
fprintf(fid,'%6s\n','*********************************************');
fprintf(fid,'%6s\n','*elset, elset=work, internal, instance=Workpiece-1');
fprintf(fid,'%6.0f,\n',1:length(n));
fprintf(fid,'%6s\n','*********************************************');
fprintf(fid,'%6s\n','*SURFACE, NAME=work_interior, TYPE=ELEMENT ');
fprintf(fid,'%6s\n','work, INTERIOR');
fprintf(fid,'%6s\n','*********************************************');
fprintf(fid,'%6s\n','*SURFACE, NAME=work_exterior, TYPE=ELEMENT ');
fprintf(fid,'%6s\n','work,');
% ************************************************************
fprintf(fid,'%6s\n','*End Assembly');
fprintf(fid,'%6s\n','*section controls,name=ec,element deletion=yes');
fprintf(fid,'%6s\n','*Amplitude,name=Amp-1,time=total time,definition=smooth step');
fprintf(fid,'%6f, %6f,%6e,%6f\n',0,0,time/5,1);

%define materials
% ***********************************************************
fprintf(fid,'%6s\n','** MATERIALS');
fprintf(fid,'%6s\n','*Material, name=Ti6Al4V');
fprintf(fid,'%6s\n','*Conductivity');
fprintf(fid,'%6.4f, %6.0f\n',6.6, 25);
fprintf(fid,'%6.4f, %6.0f\n',10, 1050);
fprintf(fid,'%6s\n','*Density');
fprintf(fid,'%6.1f\n',density);
fprintf(fid,'%6s\n','*Elastic');
fprintf(fid,'%6e, %6f\n',E,poisson);
fprintf(fid,'%6s\n','*Inelastic Heat Fraction');
fprintf(fid,'%3f\n',0.9);
fprintf(fid,'%6s\n','*Plastic, hardening=JOHNSON COOK');
fprintf(fid,'%6e, %6e, %6f, %6f, %6f, %6f\n',A,B,N,m,T_m,T);
fprintf(fid,'%6s\n','*Rate Dependent, type=JOHNSON COOK');
fprintf(fid,'%6f, %6f\n',C,1);
fprintf(fid,'%6s\n','*Specific Heat');
fprintf(fid,'%6f, %6f\n',500.525, 25.);
fprintf(fid,'%6f, %6f\n',800.0, 1050.);
% ************************************************************************
fprintf(fid,'%6s\n','*Material, name=Ti6Al4V_CL');
fprintf(fid,'%6s\n','*Conductivity');
fprintf(fid,'%6.4f, %6.0f\n',6.6, 25);
fprintf(fid,'%6.4f, %6.0f\n',10, 1050);
fprintf(fid,'%6s\n','*Density');
fprintf(fid,'%6.1f\n',density);
fprintf(fid,'%6s\n','*Elastic');
fprintf(fid,'%6e, %6f\n',E,poisson);
fprintf(fid,'%6s\n','*Inelastic Heat Fraction');
fprintf(fid,'%3f\n',0.9);
fprintf(fid,'%6s\n','*Plastic, hardening=JOHNSON COOK');
fprintf(fid,'%6e, %6e, %6f, %6f, %6f, %6f\n',A,B,N,m,T_m,T);
fprintf(fid,'%6s\n','*Rate Dependent, type=JOHNSON COOK');
fprintf(fid,'%6f, %6f\n',C,1);
fprintf(fid,'%6s\n','*DAMAGE INITIATION, CRITERION=JOHNSON COOK');
fprintf(fid,'%4.2f, %4.2f, %4f, %4f, %6f,%6f,%6f,%6f,\n',D_1,D_2,D_3,D_4,D_5,T_m,T↩
    ,1);
fprintf(fid,'%6s\n','*DAMAGE EVOLUTION, TYPE=DISPLACEMENT,SOFTENING=LINEAR');
```

```
fprintf(fid,'%3f\n',disp_length_cl);
fprintf(fid,'%6s\n','*Specific Heat');
fprintf(fid,'%6f, %6f\n',500.525, 25.);
fprintf(fid,'%6f, %6f\n',800.0, 1050.);
% **********************************************************************
fprintf(fid,'%6s\n','*Material, name=Ti6Al4V_chip');
fprintf(fid,'%6s\n','*Conductivity');
fprintf(fid,'%6.4f, %6.0f\n',6.6, 25);
fprintf(fid,'%6.4f, %6.0f\n',10, 1050);
fprintf(fid,'%6s\n','*Density');
fprintf(fid,'%6.1f\n',density);
fprintf(fid,'%6s\n','*Elastic');
fprintf(fid,'%6e, %6f\n',E,poisson);
fprintf(fid,'%6s\n','*Inelastic Heat Fraction');
fprintf(fid,'%3f\n',0.9);
fprintf(fid,'%6s\n','*Plastic, hardening=JOHNSON COOK');
fprintf(fid,'%6e, %6e, %6f, %6f, %6f, %6f\n',A,B,N,m,T_m,T);
fprintf(fid,'%6s\n','*Rate Dependent, type=JOHNSON COOK');
fprintf(fid,'%6f, %6f\n',C,1);
fprintf(fid,'%6s\n','*DAMAGE INITIATION, CRITERION=JOHNSON COOK');
fprintf(fid,'%4.2f, %4.2f, %4f, %4f, %6f,%6f,%6f,%6f,\n',D_1,D_2,D_3,D_4,D_5,T_m,T↩
    ,1);
fprintf(fid,'%6s\n','*DAMAGE EVOLUTION, TYPE=DISPLACEMENT,SOFTENING=LINEAR');
fprintf(fid,'%3f\n',disp_length_chip);
fprintf(fid,'%6s\n','*Specific Heat');
fprintf(fid,'%6f, %6f\n',500.525, 25.);
fprintf(fid,'%6f, %6f\n',800.0, 1050.);
% **********************************************************************
fprintf(fid,'%6s\n','*Material, name=WC');
fprintf(fid,'%6s\n','*Conductivity');
fprintf(fid,'%6f,\n',50.);
fprintf(fid,'%6s\n','*Density');
fprintf(fid,'%6f,\n',11900);
fprintf(fid,'%6s\n','*Elastic');
fprintf(fid,'%6e, %6f\n',540e+9,0.22);
fprintf(fid,'%6s\n','*Specific Heat');
fprintf(fid,'%6f\n',100);

%define intercation properties
% **********************************************************
fprintf(fid,'%6s\n','** INTERACTION PROPERTIES');
fprintf(fid,'%6s\n','*Surface Interaction, name=Friction');
fprintf(fid,'%6s\n','*Friction,TAUMAX=577e6');
fprintf(fid,'%6f,\n',friction);
fprintf(fid,'%6s\n','*Gap Conductance');
fprintf(fid,'%6f, %6f\n',5000.,     0.);
fprintf(fid,'%6f, %6f\n',      0., 1e-05);
fprintf(fid,'%6s\n','*Gap Heat Generation');
fprintf(fid,'%6f, %6f\n',0.9, 0.603);
fprintf(fid,'%6s\n','*Surface Interaction, name=No_Friction');
fprintf(fid,'%6s\n','*Friction,TAUMAX=577e6');
fprintf(fid,'%6f\n',0.05);
fprintf(fid,'%6s\n','*Gap Conductance');
fprintf(fid,'%6f, %6f\n',5000.,     0.);
fprintf(fid,'%6f, %6f\n',      0., 1e-05);
fprintf(fid,'%6s\n','*Gap Heat Generation');
fprintf(fid,'%6f, %6f\n',0.9, 0.603);

%define initial conditions
% **************************************************************************
fprintf(fid,'%6s\n','*initialconditions, type=VELOCITY');
fprintf(fid,'%6s %f\n','all_tool, 1,', V);
fprintf(fid,'%6s\n','*initialconditions, type=temperature');
fprintf(fid,'%6s %f\n','all_tool,', 25);
fprintf(fid,'%6s\n','*initialconditions, type=temperature');
fprintf(fid,'%6s %f\n','all_work,', 25);

%define step definitions
% **************************************************************************
fprintf(fid,'%6s\n','** STEP: Step-1');
fprintf(fid,'%6s\n','*Step, name=Step-1');
```

```
fprintf(fid,'%6s\n','*Dynamic Temperature-displacement, Explicit');
% fprintf(fid,'%6s\n','*Dynamic,Explicit,Adiabatic');
fprintf(fid,',%6f\n',time);
fprintf(fid,'%6s\n','*Bulk Viscosity');
fprintf(fid,'%6f, %6f\n',0.06, 1.2);
fprintf(fid,'%6s, %6s\n','*FIXED MASS SCALING','FACTOR=1000');

%define boundary conditions
% **************************************************************************
fprintf(fid,'%6s\n','** BOUNDARY CONDITIONS');

fprintf(fid,'%6s\n','** Name: plane_tool Type: Displacement/Rotation');
fprintf(fid,'%6s\n','*Boundary');
fprintf(fid,'%6s\n','all_tool, 3, 3');
fprintf(fid,'%6s\n','** Name: plane_work Type: Displacement/Rotation');
fprintf(fid,'%6s\n','*Boundary');
fprintf(fid,'%6s\n','all_work, 3, 3');
fprintf(fid,'%6s\n','** Name: Tool_Y Type: Displacement/Rotation');
fprintf(fid,'%6s\n','*Boundary');
fprintf(fid,'%6s\n','Tool_top_nodes, 2, 2');
fprintf(fid,'%6s\n','** Name: Tool_Y Type: Displacement/Rotation');
fprintf(fid,'%6s\n','*Boundary');
fprintf(fid,'%6s\n','Tool_back, 2, 2');
fprintf(fid,'%6s\n','** Name: Tool_Y Type: Displacement/Rotation');
fprintf(fid,'%6s\n','** Name: U Type: Velocity/Angular velocity');
fprintf(fid,'%6s\n','*Boundary,amplitude=Amp-1, type=VELOCITY');
fprintf(fid,'%6s %f\n','Tool_back, 1, 1,', V);
fprintf(fid,'%6s\n','** Name: Work_XY Type: Symmetry/Antisymmetry/Encastre');
fprintf(fid,'%6s\n','*Boundary');
fprintf(fid,'%6s\n','Work_bottom, ENCASTRE');

%define contact definitions
% **************************************************************
fprintf(fid,'%6s\n','*CONTACT');

fprintf(fid,'%6s\n','*CONTACT INCLUSIONS');
fprintf(fid,'%6s\n',',work_interior');
fprintf(fid,'%6s\n','work_interior,work_exterior');
fprintf(fid,'%6s\n','work_interior,work_interior');
fprintf(fid,'%6s\n','tool_surf,work_exterior');
fprintf(fid,'%6s\n','tool_surf,work_interior');

fprintf(fid,'%6s\n','*CONTACT EXCLUSIONS');
fprintf(fid,'%6s\n','entry,tool_surf');
fprintf(fid,'%6s\n','RF,MS');
fprintf(fid,'%6s\n','CF,FF');
fprintf(fid,'%6s\n','CU,entry');

fprintf(fid,'%6s\n','*CONTACT PROPERTY ASSIGNMENT');
fprintf(fid,'%6s\n','RF, CU, Friction');
fprintf(fid,'%6s\n','CU, CU, Friction');
fprintf(fid,'%6s\n','RF, CF, No_Friction');
fprintf(fid,'%6s\n','MS, FF, Friction');
fprintf(fid,'%6s\n','MS, RF, Friction');

%define output request
% **************************************************************
fprintf(fid,'%6s\n','** OUTPUT REQUESTS');
fprintf(fid,'%6s\n','*Restart, write, number interval=600, time marks=NO');
fprintf(fid,'%6s\n','*Output, field, number intervals=600, time marks=Yes');
fprintf(fid,'%6s\n','*Node Output');
fprintf(fid,'%6s\n','A, Nt, RF, U, V');
fprintf(fid,'%6s\n','*Element Output');
fprintf(fid,'%6s\n','E, LE, NE, PE, PEEQ, PEMAG, S, STATUS, TEMP,SDEG');
fprintf(fid,'%6s\n','*END STEP');
fprintf(fid,'%6s %6e\n','**thickness',thick);
fclose(fid);

t=toc

time
```

C.2 Node and mesh generator

```
function [nodes_work,joints_work]= work_mesher_graded(nex,ney,l_w,h_w,h_chip,sh_e,↩
    dist_ang)
%tabulate corner coords
tr = [l_w+h_chip*tan(dist_ang) -h_chip];
tl = [h_chip*tan(dist_ang) -h_chip];
bl = [h_chip*tan(dist_ang) -h_chip-sh_e];
br = [l_w+h_chip*tan(dist_ang) -h_chip-sh_e];

node = 0;
y_inc = h_w/ney;
x = tr(1):-l_w/nex:tl(1);
a=1.4
ii=1
for norm=0:1/(ney):1
    z(ii)=norm
    y(ii)= norm^a
    ii=ii+1
end

y=-y*h_w-h_chip-sh_e

% plot(z,y)

ii=0
jj=0
for ii = 2:ney+1;
    jj = 0;

    for X = x
        jj = jj+1;
        node = node+1;

        gcoord_work(node,1) = X;
        gcoord_work(node,2) = y(ii);
         gcoord_work(node,3) = 0;
    end
end


node = 0;
el = 0;
for jj = 1:ney
    node = node+1;
    for ii = 1:nex
        el = el+1;
        nodes_work(el,:) = [el node node+1 nex+3+node-1 nex+2+node-1];
        global_node=node;
        node = node+1;
    end
end
joints_work = [1:length(gcoord_work)]';
joints_work(:,2:4) = gcoord_work;

% joints_work(1,3) =joints_work(1,3)-sh_e
```

C.3 Mesh visualiser function

```
%*********************************************************************
% OUTPUTS
%*********************************************************************
% joints - [no. nodes,4] array containing [node no. :: x coord :: y coord :: z coord↩
    ]
% nodes  - [no. elements,5/9] array containing [element no. :: <connectivity>]
```

```
%
% PLEASE CHECK THAT THE FOLLOWING ARE CORRECT!!!
%
% RHSnodes - vector containing nodes along R.H.S. edge
% LHSnodes - vector containing nodes along L.H.S. edge
% BOTnodes - vector containing nodes along Bottom edge
%
% Use the
%*************************************************************************
function plotter(nodes,joints)

% --- user inputs start --- %
% input file to plot
display_mesh = 'yes';         % OPTIONS <yes/no>
display_nodes = 'no';        % OPTIONS <yes/no>
display_nodenumbers = 'no'; % OPTIONS <yes/no>
tol=1e-5;                     % proximity tolerance for node extraction
                              % DEFAULT <1e-5>
% --- user inputs end --- %

% check for number of nodes per element
nonodes=size(nodes,2)-1;

% display element connectivity (mesh)
figure(1); hold on;

switch lower(display_mesh)
    case{'yes'}
        for j=1:size(nodes,1)
            if nonodes==4
                inodes=nodes(j,2:5); % extract element connectivity <q4>
            elseif nonodes==8
                inodes=nodes(j,[2 6 3 7 4 8 5 9]); % extract element connectivity <↩
                    q8>
            end
            x = joints(inodes,2); % extract element's x coordinates
            y = joints(inodes,3); % extract element's y coordinates
            patch(x,y,'b'); % plot element
         end
end

% display nodes and node numbers
for j=1:size(joints,1)
    switch lower(display_nodes)
        case{'yes'}
            plot(joints(j,2),joints(j,3),'r.'); % plot node
    end
    switch lower(display_nodenumbers)
        case{'yes'}
            node_num=num2str(joints(j,1)); % extract node number
            text(joints(j,2),joints(j,3),node_num,'FontSize',12); % plot node number↩
                 on figure
    end
end

hold off; axis equal;

% extract nodes of interest
ndRHS=0;  % counter
ndLHS=0;  % counter
ndBOT=0;  % counter
for j=1:size(joints,1)
    % extract RHS nodes
    if abs(joints(j,2) - 40) - tol <= 0
        ndRHS=ndRHS+1;
        RHSnodes(ndRHS)=joints(j,1);
    end
    % extract LHS nodes
    if abs(joints(j,2)) - tol <= 0
        ndLHS=ndLHS+1;
        LHSnodes(ndLHS)=joints(j,1);
```

```
    end
    % extract nodes along bottom
    if abs(joints(j,3)) - tol <= 0
        ndBOT=ndBOT+1;
        BOTnodes(ndBOT)=joints(j,1);
    end
end


%% sort nodes in assending order
% [jnk,indxRHS]=sort(joints(RHSnodes,3));
% [jnk,indxLHS]=sort(joints(LHSnodes,3));
% [jnk,indxBOT]=sort(joints(BOTnodes,2));
% RHSnodes=RHSnodes(indxRHS);
% LHSnodes=LHSnodes(indxLHS);
% BOTnodes=BOTnodes(indxBOT);

% display nodes on screen
% disp('Nodes along RHS:')
% disp(RHSnodes')
% disp('Nodes along LHS:')
% disp(LHSnodes')
% disp('Nodes along Bottom edge:')
% disp(BOTnodes')
```

Appendix D

Matlab milling model

D.1 Program for predicting milling forces

```
clear;close all,clc
%warning('off','MATLAB:divideByZero')
tic
%program for predicting ball nose milling forces from orthogonal data
%according to the "unified mechanics of cutting model". This version of the
%code predicts cutting forces for the Sandvik ball nose end mill detailed
%in the relevant section of the dissertation

% Nomenclature
% a                     axial depth of cut [mm]
% b                     width of cut [mm]
% F_P,F_Q               power and thrust force components in orthogonal cutting
% F_xj,F_yj,F_zj        milling forces in Cartesian coordinates on flute j
% dF_t, dF_r, dF_a      differential cutting forces in tangential, radial and axial ↩
    direction in milling
% i_0                   helix angle at flute, shank meeting point
% i(psi)                local helix angle or angle of obliquity
% psi                   lag angle between the tip (z=0) and a point on the helical ↩
    flute at height z
% Psi                   lag angle in global coordinate, measured from+y-axis CW
% psi_0                 maximum lag angle between the tip (z---0) and uppermost ↩
    cutting point (z--a)
% K_tc,K_rc,K_ac        tangential, radial and axial cutting force coefficients in ↩
    milling
% K_tc,K_rc,K_ac        tangential, radial and axial edge force coefficients in ↩
    milling
% N_f                   number of flutes
% R_0                   ball radius
% R(psi)                tool radius in x-y plane at a point defined by psi
% r_t                   cutting chip ratio in orthogonal cutting
% s_t                   feed per tooth
% t,t_c                 uncut and cut chip thickness in orthogonal cutting
% t_n                   uncut chip thickness normal to cutting edge in milling
% alpha_r, alpha_n      radial and normal rake angles
% db                    differential cutting edge length in the direction ↩
    perpendicular to the cutting velocity
% dz                    differential length in axial direction
% kappa                 angle in a vertical plane between a point on the flute and ↩
    the z-axis
% beta                  friction angle on the rake face
% phi                   shear angle in orthogonal cutting
% phi_n,beta_n          normal shear and normal friction angles in oblique cutting
% n_c                   chip flow angle on the rake face
% tau                   shear stress at the shear plane
% theta                 tool rotation angle, measured from+y-axis CW
% psi_1, psi_2          integration limits
```

```
% N                    spindle speed in rpm

%tool geometry
rpm = 240;
rake = 0;
i_0 = 30*pi/180;
R_0 = 6;
a = 5.5;
s_t = 0.1;
alpha_n = 0*pi/180;
J = 1;
N_f = 1;

% cutting conditions
psi_0 = i_0;
psi_1 = 0*pi/180;
psi_2 = psi_0;
psi_inc = 50;
d_psi = (psi_2-psi_1)/psi_inc;

%*************************************************************************
theta_1 = 0;
theta_2 = 2*pi
theta_inc = 100;

%increment for cutter rotation
ii = 0;
for theta = theta_1:(theta_2-theta_1)/theta_inc:theta_2
    ii = ii+1
    theta_(ii) = theta;

    jj = 0;
    psi_old = 0;
    xx_old=0;
    yy_old=0;
    zz_old=0;

    %increment for flute position
    for psi = psi_1:d_psi:psi_2
        jj = jj+1;

        %call function which describes cutter geometry
        [R,kappa,t,z,v,Psi,helix,xx,yy,zz,dSs] = sandvik_geometry(theta,psi,i_0,R_0,↩
            s_t,N_f,J,d_psi,rpm,psi_old,xx_old,yy_old,zz_old);
        R_(ii,jj) = R;
        t_(ii,jj)=t;
        psi_(ii,jj) = psi;
        Psi_(ii,jj) = Psi;
        dSs_(ii,jj) = dSs;
        z_(ii,jj) = z;
        v_(ii,jj) = v;
        kap(ii,jj) = kappa;
        HELIX(ii,jj)=helix;
        psi_old=psi;
        xx_old=xx;
        yy_old=yy;
        zz_old=zz;

        %call function which calculates cutting coefficients and edge forces from ↩
            cutting
        %test data
        if rake ==0
            [Ft,Fr,r_,Kte,Kre,Kae] = data_fem(t_(ii,jj));
        end
        if rake ==5
            [Ft,Fr,r_,Kte,Kre,Kae] = data_r5(t_(ii,jj));
        end

        %call function which calculates friction and shear angles as well
        %as shear stress according to Merchant
        [beta,phi,tau] = merchant(Fr,Ft,alpha_n,r_,t_(ii,jj));
```

```
        if t_(ii,jj)==0
            tau = 0;
            tau_(ii,jj)= tau;
        end
        if isnan(tau)
            tau = 0;
        end
        tau_(ii,jj)= tau;

        %call function which calculates cutting coefficient from cutting test data
        [Ktc,Krc,Kac,n_c] = edge_coefficients(tau,beta,r_,alpha_n,helix);

        n_c_(ii,jj) = n_c;
        K_tc(ii,jj) = Ktc;
        K_rc(ii,jj) = Krc;
        K_ac(ii,jj) = Kac;
        K_te(ii,jj) = Kte;
        K_re(ii,jj) = Kre;
        K_ae(ii,jj) = Kae;

        dz(ii,1) = z_(1,1);
        if jj>1
            dz(ii,jj) = z_(ii,jj) - z_(ii,jj-1);
        end

        dB(ii,jj) = dz(ii,jj)/sin(kappa);
        if jj==2
            dB(ii,1)= dB(ii,jj);
        end

        dF_r(ii,jj) = Kre*dSs + K_rc(ii,jj)*t_(ii,jj)*dB(ii,jj);
        dF_t(ii,jj) = Kte*dSs + K_tc(ii,jj)*t_(ii,jj)*dB(ii,jj);
        dF_a(ii,jj) = Kae*dSs + K_ac(ii,jj)*t_(ii,jj)*dB(ii,jj);
        t__(ii,jj) = t_(ii,jj);

        if t_(ii,jj)==0 | z_(ii,jj)>a
            dF_r(ii,jj) = 0;
            dF_t(ii,jj) = 0;
            dF_a(ii,jj) = 0;
        end

        dF_rta = [dF_r(ii,jj); dF_t(ii,jj); dF_a(ii,jj)];

        %call function defining transformation for force transformation from local
        %to global coordinate system
        [dF_x,dF_y,dF_z] = transformation_matrix(Psi,kappa,dF_rta);
        if isnan(dF_x)
            dF_x = 0;
        end
        if isnan(dF_y)
            dF_y = 0;
        end
        if isnan(dF_z)
            dF_z = 0;
        end
        dF_x_(ii,jj) = dF_x;
        dF_y_(ii,jj) = dF_y;
        dF_z_(ii,jj) = dF_z;

    end
end

figure(1)
mesh(psi_*180/pi,theta_*180/pi,dF_r)
xlabel('Psi [deg]')
ylabel('Theta-rotation angle [deg]')
zlabel('Radial forces [N]')
title('Radial forces as a function of psi and theta')

figure(2)
```

```
mesh(psi_*180/pi,theta_*180/pi,dF_t)
xlabel('Psi [deg]')
ylabel('Theta-rotation angle [deg]')
zlabel('Tangential forces [N]')
title('Tangential forces as a function of psi and theta')

figure(3)
mesh(psi_*180/pi,theta_*180/pi,dF_a)
xlabel('Psi [deg]')
ylabel('Theta-rotation angle [deg]')
zlabel('Axial forces [N]')
title('Axial forces as a function of psi and theta')

figure(4)
mesh(psi_*180/pi,theta_*180/pi,t__)
xlabel('Psi [deg]')
ylabel('Theta-rotation angle [deg]')
zlabel('Thickness of cut [mm]')
title('Thickness of cut as a function of psi and theta')

figure(5)
mesh(psi_*180/pi,theta_*180/pi,dF_x_)
xlabel('Psi [deg]')
ylabel('Theta-rotation angle [deg]')
zlabel('X force [N]')
title('X forces as a function of psi and theta')

figure(6)
mesh(psi_*180/pi,theta_*180/pi,dF_y_)
xlabel('Psi [deg]')
ylabel('Theta-rotation angle [deg]')
zlabel('Y force [N]')
title('Y forces as a function of psi and theta')

figure(7)
mesh(psi_*180/pi,theta_*180/pi,dF_z_)
xlabel('Psi [deg]')
ylabel('Theta-rotation angle [deg]')
zlabel('Z forces [N]')
title('Z force as a function of psi and theta')

figure(8)
plot(theta_*180/pi,Fx,'r')
axis([0 250 -900 1200])
hold on
plot(theta_*180/pi,Fy,'b')
plot(theta_*180/pi,Fz,'m')
plot(theta_*180/pi,Fx_exp,'r-.')
plot(theta_*180/pi,Fy_exp,'b-.')
plot(theta_*180/pi,Fz_exp,'m-.')
[data] = load_data(theta_inc)
plot(theta_*180/pi,data,'k')

legend('F_x exp','F_y exp','F_z exp','F_x FEM','F_y FEM','F_z FEM','test data')
grid on
xlabel('cutter rotation angle [deg]')
ylabel('force [N]')

time = toc
```

D.2 Function defining geometry of a Sandvic ball nose mill

```
%% clear all;close all
function [R,kappa,t,z,v,Psi,helix,xx,yy,zz,dS] = sandvik_geometry(theta,psi,i_0,R_0,↩
    s_t,N_f,J,d_psi,rpm,psi_old,xx_old,yy_old,zz_old);

coord = [-190.922      91.2246      227;
```

```
        -190.9        92.019        227.9;
        -190.7        92.493        228.5;
        -190.5        92.834        229;
        -190.2374     93.1592       229.5;
        -189.8768     93.3665       230;
        -189.4466     93.5628       230.5;
        -188.9        93.63         231;
        -188.2        93.6181       231.5;
        -187.4        93.519        232;
        -186.3        93.221        232.5
        -181.9-3.022  92.021        233];

edge(:,1) = coord(:,1) + 190.922;
edge(:,2) = coord(:,2) - 91.2246;
edge(:,3) = coord(:,3) - 227;
% figure(1)
% plot3(edge(:,1),edge(:,2),edge(:,3),'r*-')
%
% xlabel('x');
% ylabel('y');
% zlabel('z');


[psi_,R_,Z_] = cart2pol(edge(:,3),edge(:,2),edge(:,1));
psi_ = -(psi_-pi/2);
psi_(1) = 0;
psi_(2:end) = (psi_(2:end) - psi_(2)*0.9999 + pi/180);

% figure(2);
% polar(psi_,R_);

[pp,p] = csaps(psi_,Z_);
points=fnplt(pp);

% fnplt(pp)
% hold
% plot(psi_,Z_)

psi_p=points(1,:);
Z_p=points(2,:);

for ii=1:length(Z_p)-1

    if Z_p(ii+1)==Z_p(ii)
        Z_p(ii+1)=Z_p(ii+1)*0.99999;
        psi_p(ii+1)=psi_p(ii+1)*0.999999;
    end
end
Z_p(4)=Z_p(4)*0.999999;
psi_p(4)=psi_p(4)*0.999999;
z = INTERP1(psi_p,Z_p,psi);

Psi = theta-psi;
R = INTERP1(psi_,R_,psi);
kappa = asin(R/R_0);
t = s_t*sin(Psi)*sin(kappa);


[xx,yy,zz]=pol2cart(psi,R,z);
dS=sqrt((xx-xx_old)^2+(yy-yy_old)^2+(zz-zz_old)^2);

% helix = atan((psi-psi_old)/dSs);

helix = asin((R*(d_psi))/dS)*0.6;
% helix = atan((R/R_0)*tan(30/180*pi));
omega = rpm/60*2*pi ;
v = R*omega*60/1000;
v=75;
if t>=0
    t = t;
else
```

```
    t =0;
end
```

D.3 Orthogonal cutting database

```
function [F_t,F_r,r_,K_te,K_re,K_ae] = data(vel,thickness)
% clear all


f_v_15=[13.0784    32.1158;
    22.03389831  36.27118644;
    30.09952911  40.13270548;
    74.41272474  62.70735231;
    118.7259204  80.26541096;
    201.1524086  114.3648775;
    334.1725498  154.9197986;
    437.9429768  180.3788123]*0.95;


f_v_40 =[14.2449    25.9980;
    20.338983   32.20338983;
    26.06483541  37.35959742;
    64.29326068  58.21146575;
    109.7552083  73.45833333;
    184.1915036  98.17754671;
    314.7061877  138.6978301;
    437.9429768  180.3788123]*0.95;


f_v_75=[7.7387    20.2335;
    16.94915254  29.49152542;
    25.19600756  37.09725311;
    61.68677714  54.73615436;
    99.64412811  69.39501779;
    183.9302682  94.85193201;
    308.079838   143.016767;
    437.7104   193.6027]*0.95;


f_v_125=[4.1201    15.8608;
    15.25423729  28.81355932;
    24.74398226  38.76557221;
    65.9839527   56.91115921;
    108.692744   72.74052868;
    186.2516108  103.2149377;
    338.9830508  152.5423729;
    437.7104   193.6027]*0.95;

f_v_200=[3.2577    23.4843;
    15.5932203  30.50847458;
    25.56878167  36.29117399;
    61.87125428  59.36296019;
    118.294942   91.44786297;
    180.0000     112.6169996;
    338.9830508  152.5423729;
    437.7104   193.6027]*0.95;
%
%   Kte = 20;                       %[N/mm]
%
% Kre = 30;

ft(1:8,2:6) = [f_v_15(:,1)-f_v_15(1,1) f_v_40(:,1)-f_v_40(1,1) f_v_75(:,1)-f_v_75↩
    (1,1) f_v_125(:,1)-f_v_125(1,1) f_v_200(:,1)-f_v_200(1,1)];
fr(1:8,2:6) = [f_v_15(:,2)-f_v_15(1,2) f_v_40(:,2)-f_v_40(1,2) f_v_75(:,2)-f_v_75↩
    (1,2) f_v_125(:,2)-f_v_125(1,2) f_v_200(:,2)-f_v_200(1,2)];
ft(1:8,1) = ft(1:8,2);
fr(1:8,1) = fr(1:8,2);
```

```
kte = [f_v_15(1,1) f_v_15(1,1) f_v_40(1,1) f_v_75(1,1) f_v_125(1,1) f_v_200(1,1)];
kre = [f_v_15(1,2) f_v_15(1,2) f_v_40(1,2) f_v_75(1,2) f_v_125(1,2) f_v_200(1,2)];

fd = [0 0.0025 0.005 0.025 0.05 0.1 0.2 0.3];
V = [0 15 40 75 125 200];

r =[0.5 0.5 0.5 0.5     0.5     0.5     0.5     0.5;
    0.5 0.5 0.5 0.49686 0.67344 0.56829 0.55556 0.52692;
    0.5 0.5 0.5 0.55147 0.63218 0.58252 0.50955 0.52941;
    0.5 0.5 0.5 0.52897 0.64767 0.61983 0.49383 0.55556;
    0.5 0.5 0.5 0.56122 0.625   0.55556 0.55814 0.5;
    0.5 0.5 0.5 0.63158 0.5     0.5     0.5     0.5];
%

F_t = interp2(V,fd,ft,vel,thickness,'cubic');
F_r = interp2(V,fd,fr,vel,thickness,'cubic');
r_ = interp2(fd,V,r,thickness,vel,'cubic');

K_te =interp1(V,kte,vel);
K_re =interp1(V,kre,vel);
K_ae = 0;

% figure(1)
% mesh(V,fd,ft)
% title('Cutting force in turning tests')
% xlabel('Cutting speed [m/min]')
% ylabel('Feed [mm/rev]')
% zlabel('Cutting force [N/mm]')
% % view(90,0)
% figure(2)
% % hold on
% mesh(V,fd,fr)
% title('Feed force in turning tests')
% xlabel('Cutting speed [m/min]')
% ylabel('Feed [mm/rev]')
% zlabel('Feed force [N/mm]')
% view(90,0)
```

D.4 Function for calculating edge coefficients

```
function [Ktc,Krc,Kac,n_c] = edge_coefficients(tau,beta,r_t,alpha_n,i_)

ii = 0;
for n_c = 0:15*pi/180/100:15*pi/180
    ii = ii+1;
    nc(ii) = n_c;

    beta_n(ii) = atan(tan(beta)*cos(n_c));

    phi_n(ii) = atan(r_t*(cos(n_c)/cos(i_))*cos(alpha_n)/(1-r_t*(cos(n_c)/cos(i_))*↩
        sin(alpha_n)));

    lhs(ii) = tan(phi_n(ii)+beta_n(ii));
    rhs(ii) = cos(alpha_n)*tan(i_)/(tan(n_c)-sin(alpha_n*tan(i_)));

    ratio(ii) = abs(rhs(ii))-abs(lhs(ii));
    error(ii) = 1-ratio(ii);

end

[y,ind] = min(abs(ratio));

n_c = nc(ind);

beta_n = beta_n(ind);
phi_n = phi_n(ind);
```

```
% beta_n = atan(tan(beta)*cos(i_));
%
% phi_n = atan(r_t*cos(alpha_n)/(1-r_t*sin(alpha_n)));
n_c=i_;

% compute edge coefficients

c = sqrt(cos(phi_n + beta_n - alpha_n)^2 + tan(n_c)^2*sin(beta_n)^2);

Ktc = tau/sin(phi_n)*(cos(beta_n - alpha_n) + tan(n_c)*sin(beta_n)*tan(i_))/c/1e6; ↩
            %[N/mm^2]

Krc  = tau/(sin(phi_n)*cos(i_))* sin(beta_n - alpha_n)/c/1e6; ↩
                                %[N/mm^2]

Kac = tau/sin(phi_n)*(cos(beta_n - alpha_n)*tan(i_) - tan(n_c)*sin(beta_n))/c/1e6; ↩
       %[N/mm^2]
```

D.5 Transformation matrix for local to global coordinate transformation

```
function [dF_x,dF_y,dF_z] = transformation_matrix(Psi,kappa,dF_rta)

dF_xyz =    [-sin(kappa)*sin(Psi)  -cos(Psi)   -cos(kappa)*sin(Psi);
             -sin(kappa)*cos(Psi)   sin(Psi)   -cos(kappa)*cos(Psi);
              cos(kappa)            0                -sin(kappa)]*dF_rta;


              dF_x = dF_xyz(1);
              dF_y = dF_xyz(2);
              dF_z = dF_xyz(3);
```

D.6 Function to calculate chip thickness

```
function [R,kappa,t,PSI,z,jj,i_psi] = thickness(theta,psi_1,psi_2,i_0,R_0,s_t)
R=0;
kappa = 0;
t = 0;
j = 1;
N_f = 1;
jj = 0;
for psi = psi_1:psi_2/20:psi_2
    jj = jj+1;
    PSI(jj) = psi;
    Psi = theta-psi;
    R(jj) = R_0*sqrt(1-(psi*cot(i_0)-1)^2);
    kappa(jj) = asin(R(jj)/R_0);
    t(jj) = s_t*sin(Psi)*sin(kappa(jj));
    z(jj) = -(Psi - theta - (j-1)*2*pi/N_f)*R_0/tan(i_0);
    i_psi(jj) = atan((R(jj)/R_0)*tan(i_0));
end
```